Numerical methods for fluid-structure interaction, and their application to flag flapping

Thesis by
Andres Goza

In Partial Fulfillment of the Requirements for the
degree of
Doctor of Philosophy

CALIFORNIA INSTITUTE OF TECHNOLOGY
Pasadena, California

2018
Defended (October 5, 2017)

ACKNOWLEDGEMENTS

I am indebted to many people who over these past several years have informed my view on research, fluid mechanics, mathematics, advising, teaching, squash, movies and storytelling, comedy, and much more. Perhaps most of all, I am grateful that they have made my growth in these areas a journey that I will look back on so fondly.

I first thank Tim. Beyond your intimidating instincts for and knowledge of fluid mechanics and applied mathematics, your tireless efforts as an advisor had a huge impact on me. I think what I will remember most are moments you spent teaching me about writing and presenting, discussing advising philosophies, or cracking a witty joke (on the rare occasion that occurred!). I will try my hardest to be as wonderful an advisor as you were to me.

I am also grateful to my committee for being such sources of inspiration and guidance during my time here. John, thank you for your heroic efforts in helping me hone in on the narrative for inverted flag flapping, and for acting as a second advisor to me. Guillaume, thank you for your jokes and willingness to give as good as you get, and for taking the time to meet with me about this thesis and life after graduate school. Mory, your pioneering work on inverted flag flapping is singularly responsible for my pursuit of that topic, and I feel honored to have you on my committee.

I must also thank Aaron, Jomela, Ed, Jay, Chen, Jeeson, Oliver, George, Gianmarco, Sebastian, Vedran, Phillipe, Kazuki, Andre 2.0, Marcus, Ke, and Francisco for making my time in Thomas, Steele, and Gates-Thomas so much more rewarding than it would have been without you. I am particularly grateful to Aaron, whose mathematical intuition was always a source of intimidation and inspiration for me; and to Phillipe for being the best colleague in fluid-structure interaction that I could have asked for.

Thanks also to Paul, Massari, Matt, Alex, and Ron for being such wonderful friends outside of research. I will always remember the nights out on the town, bowling events, softball games, squash matches, and general tomfoolery that your friendships afforded me.

There are a number of people from my undergraduate days who were formative during my time at Caltech. I thank BC and Mark, who were the first ones to inspire me to pursue applied mathematics and fluid mechanics, and to show me how impactful an advisor can be. I am also grateful to Travis, for being the best friend in

the whole world throughout both my graduate and undergraduate days. My thanks also go out to Rachel, Matt, Gianmarco, and Marina for being there for me at various times.

Most influential of all have been my family, who believed in me and supported me for longer than I can remember. Mom, Dad, Laurie and Jules, I am only beginning to realize how much effort you have taken to prioritize me and give me every opportunity possible, and I will never forget it.

Last and in a category unto herself is Tess. Thank you for teaching me more than I have ever learned from any one person about research, stories, life and love. I can not begin to convey my gratitude for the growth you have inspired in me, support you have given me despite your hectic schedule, and belief and love you have shown me. All I can say is I look forward to spending the rest of my life trying to repay the favor.

ABSTRACT

This thesis is divided into two parts. Part I is devoted to the development of numerical techniques for simulating fluid-structure interaction (FSI) systems and for educing important physical mechanisms that drive these systems' behavior; part II discusses the application of many of these techniques to investigate a specific FSI system.

Within part I, we first describe a procedure for accurately computing the stresses on an immersed surface using the immersed boundary method. This is a key step to simulating FSI problems, as the surface stresses simultaneously dictate the motion of the structure and enforce the no-slip boundary condition on the fluid. At the same time, accurate stress computations are also important for applications involving rigid bodies that are either stationary or moving with prescribed kinematics (*e.g.*, characterizing the performance of wings and aerodynamic bodies in unsteady flows or understanding and controlling flow separation around bluff bodies). Thus, the method is first formulated for the rigid-body prescribed-kinematics case. The procedure described therein is subsequently incorporated into an immersed boundary method for efficiently simulating FSI problems involving arbitrarily large structural motions and rotations.

While these techniques can be used to perform high-fidelity simulations of FSI systems, the resulting data often involves a range of spatial and temporal scales in both the structure and the fluid and are thus typically difficult to interpret directly. The remainder of part I is therefore devoted to extending tools regularly used for understanding complex flows to FSI systems. We focus in particular on the application of global linear stability analysis and snapshot-based data analysis (such as dynamic mode decomposition and proper orthogonal decomposition) to FSI problems. To our knowledge, these techniques had not been applied to deforming-body problems in a manner that that accounts for both the fluid and structure leading up to this work.

Throughout part I, our methods are derived in the context of fairly general FSI systems and are validated using results from the literature for flapping flags in both the conventional configuration (in which the flag is pinned or clamped at its leading edge with respect to the oncoming flow) and the inverted configuration (in which the flag is clamped at its trailing edge). In part II, we apply many

of the techniques developed in part I to uncover new physical mechanisms about inverted flag flapping. We identify the instability-driving mechanism responsible for the initiation of flapping and further characterize the large-amplitude and chaotic flapping regimes that the system undergoes for a range of physical parameters.

PUBLISHED CONTENT AND CONTRIBUTIONS

Andres Goza et al. "Accurate computation of surface stresses and forces with immersed boundary methods". In: *Journal of Computational Physics* 321 (2016), pp. 860–873. DOI: 10.1016/j.jcp.2016.06.014

AJG established the equation for the surface stresses as a first-kind integral equation, identified the connection between differentiability of the smeared delta functions and the quality of the resulting stresses, ran all simulations, and was the primary author of the article.

Andres Goza and Timothy Colonius. "A strongly-coupled immersed-boundary formulation for thin elastic structures". In: *Journal of Computational Physics* 336 (2017), pp. 401–411. DOI: 10.1016/j.jcp.2017.02.027

AJG devised and implemented the numerical method, ran all simulations, and was the primary author of the article.

Andres Goza and Timothy Colonius. "A global mode analysis of flapping flags". In: *Turbulence and Shear Flow Phenomena 10*. Chicago, Illinois, 2017.

AJG devised and implemented the numerical method, ran all simulations, and was the primary author of the article.

Andres Goza, Timothy Colonius and John E. Sader. "Nonlinear simulations and global modes of inverted flag flapping". Submitted to the *Journal of Fluid Mechanics*.

AJG identified the mechanism responsible for the onset of flapping, distinguished parameters under which vortex-induced vibration occurs in large-amplitude flapping, characterized the chaotic regime, ran all simulations, and was the primary author of the article.

Andres Goza and Timothy Colonius. "Data analysis of fluid-structure interaction". *In preparation*.

AJG extended modal-decomposition methods to fluid-structure interaction systems, identified an appropriate norm for these methods, ran all simulations, and was the primary author of the article.

TABLE OF CONTENTS

Acknowledgements . . . iii
Abstract . . . v
Published Content and contributions . . . vii
Table of Contents . . . viii
List of Illustrations . . . x
List of Tables . . . xiii
Nomenclature . . . xiv

I Numerical methods for fluid-structure interaction 1
Chapter I: Introduction . . . 2
Chapter II: Accurately computing surface stresses and forces with immersed boundary methods . . . 4
2.1 Introduction . . . 4
2.2 Demonstrating and resolving inaccurate computation of source terms for a model problem . . . 6
2.3 Extension to accurately computing surface stresses and forces . . . 15
2.4 An impulsively rotated cylinder . . . 18
2.5 A cylinder in cross-flow . . . 21
2.6 Conclusions . . . 23
Chapter III: An efficient immersed-boundary method for fluid-structure interaction . . . 25
3.1 Introduction . . . 25
3.2 Governing equations . . . 26
3.3 Numerical method . . . 28
3.4 Verification on flapping flag problems . . . 34
3.5 An efficient iteration procedure in primitive variables . . . 41
3.6 Conclusions . . . 42
Chapter IV: Global stability analysis of fluid-structure interaction . . . 44
4.1 Introduction . . . 44
4.2 Numerical method . . . 44
4.3 Validation on conventional flag flapping . . . 46
4.4 Conclusions . . . 50
Chapter V: Data analysis of fluid-structure interaction . . . 51
5.1 Introduction . . . 51
5.2 POD and DMD of fluid-structure interaction . . . 53
5.3 Limit-cycle flapping of conventional and inverted flags . . . 56
5.4 Chaotic flapping of conventional flags . . . 61
5.5 Conclusions . . . 67

Chapter VI: Outlook 69

II Physics of inverted flag flapping **71**

Chapter VII: Introduction 72

Chapter VIII: Nonlinear simulations and global mode analysis of inverted flag flapping 77

8.1 Simulation parameters 77

8.2 Dynamics for $Re = 200$ 77

8.3 Dynamics for $Re = 20$ 93

8.4 Conclusions 99

Chapter IX: Outlook 102

LIST OF ILLUSTRATIONS

Number *Page*

2.1 Incorrect source terms for Poisson problem 9
2.2 Convergence plot for incorrect source terms 10
2.3 Convergence plot for the solution to the Poisson problem 10
2.4 Singular value decay for different smeared δ_h 11
2.5 Decay of exact coefficients for different δ_h 12
2.6 Decay of computed coefficients for different δ_h 14
2.7 Filtered source term for the Poisson problem 14
2.8 Convergence plots for the filtered source term 14
2.9 Stresses for rotating cylinder problem 20
2.10 Errors for rotating cylinder problem 21
2.11 Surface force for rotating cylinder problem 21
2.12 Errors in filtered stresses for rotating cylinder problem 21
2.13 Surface stresses for a cylinder in cross-flow 23
2.14 Convergence plot for the cylinder in cross-flow problem 23
2.15 Surface forces for the cylinder in cross-flow problem 24
3.1 Different flag configurations 34
3.2 Tip displacement and coefficient of lift for a conventional flag 36
3.3 Tip displacement comparison with the literature 37
3.4 Vorticity snapshots for a conventional flag 39
3.5 Illustration of various inverted flag regimes 40
3.6 Vorticity snapshots for an inverted flag 41
4.1 Prediction of the flutter boundary for conventional flag flapping . . . 48
4.2 Global mode of a conventional flag for $M_\rho = 0.05$, $K_B = 0.005$ . . . 49
4.3 Global mode of a conventional flag for $M_\rho = 1$, $K_B = 0.042$ 49
4.4 Global mode of a conventional flag for $M_\rho = 50$, $K_B = 0.06$ 50
5.1 Tip displacement and power-spectral density for small-amplitude limit-cycle flapping of a conventional flag 57
5.2 Snapshots of small-amplitude limit-cycle flapping of a conventional flag 57
5.3 POD singular values and DMD eigenvalues for small-amplitude limit-cycle flapping of a conventional flag 58

5.4 Leading POD and DMD modes for small-amplitude limit-cycle flapping of a conventional flag . . . 58
5.5 POD and DMD reconstructions of small-amplitude limit-cycle flapping of a conventional flag . . . 59
5.6 Tip displacement and power-spectral density of large-amplitude limit-cycle flapping of an inverted flag . . . 59
5.7 Snapshots of large-amplitude limit-cycle flapping of an inverted flag . 60
5.8 POD singular values and DMD eigenvalues for large-amplitude limit-cycle flapping of an inverted flag . . . 61
5.9 Leading POD and DMD modes for large-amplitude limit-cycle flapping of an inverted flag . . . 62
5.10 POD and DMD reconstructions of large-amplitude limit-cycle flapping of an inverted flag . . . 62
5.11 Tip displacement and power spectral density for large-amplitude limit-cycle flapping and chaotic flapping of a conventional flag . . . 63
5.12 DMD eigenvalues for for large-amplitude limit-cycle flapping of a conventional flag . . . 64
5.13 Leading DMD modes for large-amplitude limit-cycle flapping of a conventional flag . . . 65
5.14 DMD eigenvalues γ for chaotic flapping of a conventional flag with $Re = 500, M_\rho = 0.25, K_B = 0.0001$. . . . 65
5.15 Leading DMD modes for chaotic flapping of a conventional flag . . . 66
7.1 Time lapses for different regimes in inverted-flag flapping . . . 72
7.2 A schematic bifurcation diagram for inverted-flag flapping . . . 76
8.1 Bifurcation diagrams for inverted-flag flapping with $Re = 200$. . . . 80
8.2 Deformed equilibria of the inverted-flag system for $Re = 200$ . . . 81
8.3 Frequency response of the inverted-flag system for $Re = 200$ . . . 82
8.4 Leading global modes near the onset of small-deflection deformed flapping for $Re = 200, M_\rho = 0.5$ . . . 84
8.5 Leading global modes near the onset of small-deflection deformed flapping for $Re = 200, M_\rho = 5$ . . . 84
8.6 Snapshots of small-deflection deformed flapping . . . 85
8.7 Snapshots of large-amplitude flapping for light flags . . . 86
8.8 Plots of tip displacement and coefficient of lift for light flags . . . 87
8.9 Snapshots of large-amplitude flapping for heavy flags . . . 88
8.10 Plots of tip displacement and coefficient of lift for heavy flags . . . 88

8.11 Leading global mode for the deflected-mode regime 90
8.12 Plots of tip displacement and spectral density for chaotic flapping of an inverted flag 91
8.13 Phase portraits demonstrating the strange attractor in chaotic flapping 93
8.14 Bifurcation diagrams for inverted-flag flapping with $Re = 20$ 95
8.15 Deformed equilibria of the inverted-flag system for $Re = 20$ 96
8.16 Frequency response of the inverted-flag system for $Re = 20$ 96
8.17 Leading global mode of the deformed equilibrium near the onset of small-deflection deformed flapping for $Re = 20, M_\rho = 5$ 97
8.18 Leading global mode of the undeformed equilibrium near the onset of small-deflection deformed flapping for $Re = 20, M_\rho = 5$ 98

LIST OF TABLES

Number *Page*

2.1 Shedding frequency for the cylinder in cross-flow problem 23
3.1 Flapping amplitude and frequencies for a conventional flag at $Re = 1000$ 36
3.2 Flapping amplitude and frequencies for a conventional flag at $Re = 200$ 37
3.3 Flapping regimes of an inverted flag (comparison with the literature) 38
3.4 Flapping amplitude and frequencies for an inverted flag at $Re = 1000$ 40
8.1 Leading-mode growth rate near the onset of small-deflection deformed flapping for $Re = 200$ 83
8.2 Leading-mode growth rate near the onset of large-amplitude flapping for $Re = 200$ 85
8.3 Leading eigenvalues for the deflected-global mode regime 90
8.4 Lyapunov exponents for different regimes of the inverted-flag system 92
8.5 Leading-mode growth rate near the onset of small-deflection deformed flapping for $Re = 20$ 95
8.6 Leading-mode growth rate near the onset of large-amplitude flapping for $Re = 20$ 99

NOMENCLATURE

χ. Discrete or continuous displacement of the structure immersed in fluid.

δ. Dirac-delta function.

δ_h. Smeared delta function used in immersed-boundary methods.

Γ. Domain defining the structure.

γ_j. j^{th} eigenvalue in a dynamic-mode decomposition.

$\hat{\mathbf{u}}_j$. j^{th} singular vector in a proper-orthogonal decomposition.

$\hat{y}_j$. j^{th} global mode in a global linear stability analysis.

λ_j. j^{th} eigenvalue in a global linear stability analysis.

Ω. Domain defining the fluid.

ω. Discrete or continuous vorticity.

σ_j. j^{th} singular value in a proper-orthogonal decomposition.

$\mathbf{W}$. Weighting matrix used in defining a norm for proper-orthogonal decomposition.

ζ. Discrete or continuous velocity of the structure immersed in fluid.

f. Surface stresses that impose the no-slip boundary condition and drive structural deformation.

K_B. Dimensionless flexural rigidity: ratio of structural flexural rigidity to fluid 'rigidity'.

M_ρ. Mass ratio: ratio of structure-to-fluid inertia.

p. Fluid pressure.

Re. Reynolds number.

s. Discrete or continuous streamfunction.

St. Strouhal number.

u, v. Discrete or continuous fluid velocities.

Part I

Numerical methods for fluid-structure interaction

Chapter 1

INTRODUCTION

In flow-structure interaction (FSI) systems, fluid moves past an immersed structure and the dynamics of both the fluid and the structure are coupled to one another. High-fidelity numerical simulations can aid experiments and theory in providing physical insights into these systems that can lead to improved bio-inspired propulsion vehicles, medical devices such as heart-valve prosthetics, and renewable energy-harvesting technologies. To this end, a variety of numerical methods have been developed and used to study blood-flow through deformable heart valves [10, 26, 62], flow past flapping flags [17, 26, 32, 82], and insect flight involving passively deforming insect wings [82], to name a few examples.

Of the many methods developed for simulating FSI problems, we focus here on immersed-boundary (IB) methods, which are attractive because they treat the fluid and structure with separate grids and therefore do not involve the computationally expensive task of re-meshing. While IB methods have been extensively developed and used (see Mittal and Iaccarino [56] and Peskin [63] for reviews), there remain open challenges to making them more accurate and efficient. First, many IB methods yield inaccurate surface stresses and forces on the immersed body, both in FSI problems and in rigid-body problems where the structure is either stationary or undergoing prescribed kinematics [38, 74, 92]. Second, in FSI problems the nonlinear coupling between the fluid and structure often results in a large nonlinear algebraic system of equations that must be solved iteratively to evolve the FSI system in time (see Hou, Wang, and Layton [34] for a review), and performing these iterations efficiently remains a challenge.

We address these challenges in chapters 2 and 3. In chapter 2 we discuss the source and remedy of the unphysical surface stresses and forces provided by IB methods for rigid-bodies undergoing prescribed kinematics. We then incorporate this remedy into an FSI formulation in chapter 3, where we present an IB method with an efficient iteration procedure for treating the nonlinear fluid-structure coupling (even in the presence of large structural motions). This method is formulated for fairly general thin deforming bodies and validated from results in the literature on flapping flags in both the conventional configuration (in which the flag is pinned or clamped at its

leading edge with respect to the oncoming flow) and the inverted configuration (in which the flag is clamped at its trailing edge).

The method described in chapter 3 is capable of performing high-fidelity simulations that, along with companion simulations and experiments, is a tool for understanding FSI systems. Yet, the dynamics of FSI systems often involve a range of spatial and temporal scales that makes it difficult to identify driving physical mechanisms from simulation or experimental data alone. We therefore devote chapters 4 and 5 to the extension of global stability analysis and snapshot-based data analysis techniques to FSI problems, respectively.

Global stability analysis and snapshot-based data processing techniques have been widely used to identify significant flow features in flows without bodies or involving stationary rigid bodies (see *e.g.*, Bagheri et al. [4], Ehrenstein and Gallaire [22], and Noack and Eckelmann [60] for some applications of global stability analysis and Berkooz, Holmes, and Lumley [8] and Rowley and Dawson [67] for reviews on snapshot-based data processing techniques), and to a lesser extent in rigid-body FSI problems [50, 58]. To our knowledge, however, these techniques have not been applied to deforming-body FSI problems, and in chapters 4 and 5 we present methods that achieve this aim. The global stability solver of chapter 4 uses a linearization of the fully-coupled nonlinear FSI equations described in chapter 3, and therefore identifies instability-driving phenomena in both the fluid and the structure. This method is validated using results from the literature on conventional flag flapping. Chapter 5 develops a framework for performing proper orthogonal decomposition (POD) and dynamic mode decomposition (DMD) of FSI problems, and this framework is demonstrated on flapping flags in both the conventional and inverted configuration. We emphasize that the algorithm presented is agnostic to whether the data was obtained from simulations or experiments. Moreover, while the focus in chapter 5 is on POD and DMD because of their widespread use, straightforward extensions exist for other data processing techniques.

Chapter 2

ACCURATELY COMPUTING SURFACE STRESSES AND FORCES WITH IMMERSED BOUNDARY METHODS[1]

2.1 Introduction

The original IB method of Peskin introduced a singular source term in the momentum equations that imposed the stresses from the immersed body onto the flow grid [62]. In that work, a specific structure was assumed and the surface stresses were derived using the constitutive law for that structure. A different set of IB methods retains the use of a singular source term to impose the surface stresses, but derives these stresses using velocity boundary conditions rather than by directly linking them to deformation of the solid [15, 36–38, 45, 79, 87, 92, 94]. Because they are derived from the boundary conditions on the immersed body, we refer here to these IB methods as surface velocity-based IB methods. These methods produce surface stresses that are poor representations of the physical surface stresses. A subset of these also produce unphysical oscillations in time traces of surface force quantities such as the coefficients of lift and drag, since they enforce the boundary constraint approximately rather than explicitly [36, 87, 94]. Yang *et al.* [92] reduced the unphysical oscillations in these surface force quantities, but to our knowledge the inaccuracies in the surface stresses have not been addressed. This is likely due to the fact that the velocity field converges in spite of these erroneous surface stresses, so surface velocity-based IB methods may be used without modification for problems where accurate knowledge of the surface stresses is not required.

However, correct information about surface stresses and forces is important in many applications, such as characterizing the performance of wings and aerodynamic bodies in unsteady flows, understanding and controlling flow separation around bluff bodies, and simulating fully coupled flow-structure-interaction (FSI) problems with deforming bodies. In this chapter, we characterize and remedy the spurious surface stresses and forces obtained by surface-velocity based IB methods. We do this in the context of flows past rigid bodies undergoing prescribed kinematics in

[1]This chapter is based on the publication Goza et al. [31], for which my contributions were establishing the equation for the surface stresses as a first-kind integral equation, identifying the connection between differentiability of the smeared delta functions and the quality of the resulting stresses, running all simulations, and being the primary author of the article.

this chapter and the procedure is extended to FSI problems in chapter 3.

It should be noted that there is a class of IB methods called "sharp-interface" methods, which includes ghost-cell [57], cut-cell [86], ghost-fluid [24], and immersed interface methods [49]. While spurious surface stress and force oscillations have been observed for a subset of these methods [53, 75], their cause and remedy is different from what is presented in the current work [53]. A key distinction between this subset of sharp-interface methods and the methods considered here is the use of local flow reconstructions that obviate the need for a singular source term in the momentum equations.

We restrict our attention to methods that contain a singular source term in the momentum equations, and that compute surface stresses and forces using that term. We show that, for any choice of smeared delta function, the equation for the surface stresses is an integral equation of the first kind whose ill-posedness leads to an inaccurate representation of the high frequency components of the surface stresses. The error in these high frequency components was also observed by Kallemov *et al.* [38] for a six point delta function. We demonstrate that there is an inverse relation between the smoothness of the smeared delta function and the amplitude of the high frequency components for the physically correct stress. Thus, when sufficiently smooth delta functions are selected, the high-frequency components that are erroneously amplified when solving the integral equation may be effectively filtered out of the solution without damaging the overall surface stress. By contrast, filtering out the incorrect high frequency components for insufficiently smooth smeared delta functions obscures important physical information.

We develop an efficient filtering technique for penalizing the erroneous high frequency stress components. The filtering procedure is performed as a post-processing step, so the convergence of the velocity field is unaffected. We demonstrate that, for all smeared delta functions considered, the filtered stresses are better approximations to the physical stresses than their unfiltered counterparts. However, because of the aforementioned inverse relationship between the smoothness of the smeared delta function and the magnitude of the high frequency components required to represent the physical stresses, this filtering procedure only provides convergent surface stresses when applied to sufficiently smooth smeared delta functions. These results are illustrated for several problems using the immersed boundary projection method (IBPM) of Colonius and Taira [15].

2.2 Demonstrating and resolving inaccurate computation of source terms for a model problem

The difficulty in solving integral equations of the first kind that arise from surface velocity-based IB methods is illustrated and remedied for a model problem in this section. Section 2.3 will demonstrate that the same type of integral equation arises from the Navier-Stokes equations. Thus, the same techniques developed here may be used to compute surface stresses and forces that arise in fluid flows.

The model problem considered is the Poisson equation for an unknown function ψ on a 2D square domain $\Omega = \{\mathbf{x} = [x,\ y]^T : |x|, |y| \leq 1\}$ with an unknown singular source term f that takes nonzero values on an immersed surface denoted by Γ:

$$\begin{aligned} \nabla^2\psi(\mathbf{x}) &= -\int_\Gamma f(\boldsymbol{\chi}(s))\delta(\mathbf{x}-\boldsymbol{\chi}(s))ds \\ \psi(\mathbf{x}) &= \psi^{\partial\Omega}(\mathbf{x}),\ \mathbf{x}\in\partial\Omega \\ \int_\Omega \psi(\mathbf{x})\delta(\mathbf{x}-\boldsymbol{\chi}(s))d\mathbf{x} &= \psi^\Gamma(\boldsymbol{\chi}(s)) \end{aligned} \tag{2.1}$$

where s is a variable that parametrizes the IB (e.g., arc length), $\boldsymbol{\chi}(s)$ is the Lagrangian coordinate of a given point on the IB, $\partial\Omega$ is the boundary of the domain Ω, $\psi^{\partial\Omega}(\mathbf{x})$ is a function of prescribed values for ψ on $\partial\Omega$, and $\psi^\Gamma(\boldsymbol{\chi}(s))$ is a function defined on the immersed body. Note that the delta function $\delta(\mathbf{x}-\boldsymbol{\chi}(s))$ is used to relate quantities between the immersed surface and the solution domain. An error analysis of numerical solutions to (2.1) has been performed in the case where f is prescribed [83, 93]. To mirror surface velocity-based IB methods, we leave f as an unknown that is solved by explicitly incorporating the third equation as a boundary constraint.

We take Γ to be a circle of radius $1/2$ centered at $\mathbf{x} = 0$, $\psi^{\partial\Omega}(\mathbf{x}) = 1 - \frac{1}{2}\log(2|\mathbf{x}|)$, and $\psi^\Gamma(\boldsymbol{\chi}) = 1$. The exact solution to (2.1) is then

$$\psi_{ex}(\mathbf{x}) = \begin{cases} 1, & |\mathbf{x}| \leq \frac{1}{2} \\ 1 - \frac{1}{2}\log(2|\mathbf{x}|) & |\mathbf{x}| > \frac{1}{2} \end{cases} \tag{2.2}$$

$$f_{ex}(\boldsymbol{\chi}) = 1 \tag{2.3}$$

Another quantity of interest is $F_{ex} = \int_\Gamma f_{ex}(\boldsymbol{\chi}(s))ds = \pi$. This term is analogous to the integrated surface force, which is often of interest for IB flow solvers.

To make IB methods suitable for computation, the Dirac delta function in (2.1) is replaced with a smeared delta function, $\delta_h(\mathbf{x}-\boldsymbol{\chi}(s,t))$, that is continuous and has nonzero but compact support defined in terms of the grid spacing, h, of the

discretized domain on which the numerical solution is obtained (see, *e.g.*, reference [63]). Thus, the numerical solution for a given grid spacing h has as its corresponding continuous solution

$$\psi(\mathbf{x}) = -\int_{\Omega}\int_{\Gamma} f(\boldsymbol{\chi}(s'))\delta_h(\mathbf{x}' - \boldsymbol{\chi}(s'))G(\mathbf{x};\mathbf{x}')ds'd\mathbf{x}' \tag{2.4}$$

where $G(\mathbf{x};\mathbf{x}')$ is the Green's function for the Poisson problem evaluated at $\mathbf{x}$ due to a source at $\mathbf{x}'$, and δ_h is the (continuous) smeared delta function. The equation (2.4) is written in terms of the unknown source term f. To arrive at an equation for this source term, we multiply both sides of (2.4) by $\delta_h(\boldsymbol{\chi}(s) - \mathbf{x})$ and integrate over the domain Ω:

$$\int_{\Omega}\int_{\Omega}\int_{\Gamma} f(\boldsymbol{\chi}(s'))\delta_h(\mathbf{x}' - \boldsymbol{\chi}(s'))G(\mathbf{x};\mathbf{x}')\delta_h(\mathbf{x} - \boldsymbol{\chi}(s))ds'd\mathbf{x}'d\mathbf{x} = -\psi^{\Gamma}(\boldsymbol{\chi}(s)) \tag{2.5}$$

The solution $\psi(\mathbf{x})$ is then obtained by substituting the solution f of (2.5) into (2.4).

Since δ_h is continuous for a given grid spacing h, the kernel in the integral equation (2.5) is continuous and has finite support. Thus, the integral operator is compact and formally does not have a bounded inverse [41]. As a consequence, discretizations of this equation lead to inaccurate surface source terms. To highlight that the difficulty in computing the source term occurs for all smeared delta functions, we will use four different functions that are common in the literature. In all cases, the two-dimensional smeared delta function is defined by the tensor product of two one-dimensional smeared delta functions; *i.e.* $\delta_h(\mathbf{x} - \boldsymbol{\chi}) = \delta_h(x - \chi)\delta_h(y - \eta)$, where $\mathbf{x} = [x, y]^T$ and $\boldsymbol{\chi} = [\chi, \eta]^T$. The four one-dimensional smeared delta functions we consider are given below.

- A 2-point hat function:

$$\delta_h^{hat}(r) = \begin{cases} \frac{1}{h} - \frac{|r|}{h^2}, & |r| \le h \\ 0, & |r| > h \end{cases} \tag{2.6}$$

- A 3-point function:

$$\delta_h^3(r) = \begin{cases} \frac{1}{3h}\left(1 + \sqrt{1 - 3\left(\frac{r}{h}\right)^2}\right), & |r| \le \frac{h}{2} \\ \frac{1}{6h}\left(5 - \frac{3|r|}{h} - \sqrt{1 - 3\left(1 - \frac{|r|}{h}\right)^2}\right), & \frac{h}{2} \le |r| \le \frac{3h}{2} \\ 0, & |r| > \frac{3h}{2} \end{cases} \tag{2.7}$$

- A 4 point cosine function:

$$\delta_h^{cos}(r) = \begin{cases} \frac{1}{4h}\left(1 + \cos\left(\frac{\pi r}{2h}\right)\right), & |r| \leq 2h \\ 0, & |r| > 2h \end{cases} \tag{2.8}$$

- A Gaussian function:

$$\delta_h^{G}(r) = \begin{cases} \sqrt{\frac{\pi}{36h^2}} e^{\frac{-\pi^2 r^2}{36h^2}}, & |r| \leq 14h \\ 0, & |r| > 14h \end{cases} \tag{2.9}$$

  A Gaussian function formally has infinite support. The parameters and cut-off used in (2.9) lead to a truncation error on the order of machine precision. Other parameter choices may be selected to satisfy different error tolerances [93].

To solve the problem numerically, we discretize the system (2.1) as (after replacing the Dirac delta functions with the smeared delta functions δ_h)

$$L\psi = -Hf + b_L \tag{2.10}$$

$$E\psi = \psi^{\Gamma} \tag{2.11}$$

where the variables ψ, ψ^{Γ}, and f are understood to be the spatially discrete versions of their continuous counterparts; L is the discrete Laplacian; b_L is a boundary condition term that arises from discretizing the Laplacian operator; and $H(\cdot)$ and $E(\cdot)$ are discretizations of the operations $\int_{\Gamma}(\cdot)\delta_h(\mathbf{x} - \boldsymbol{\chi})ds$ and $\int_{\Omega}(\cdot)\delta_h(\mathbf{x} - \boldsymbol{\chi})d\mathbf{x}$, respectively. Note that the different choices of smeared delta function change E and H. Since E and H have dimensions on the order of the number of solution domain grid points by the number of immersed boundary points, the computational complexity of the algorithm scales linearly with the support of the smeared delta function.

Equations (2.10) and (2.11) may be combined to arrive at an equation for f, given by

$$EL^{-1}Hf = -\psi^{\Gamma} + EL^{-1}b_L \tag{2.12}$$

which is a discretization of the integral equation (2.5). Following Colonius and Taira [15], we construct E and H such that $EL^{-1}H$ is positive definite and symmetric. Note that the square matrix $EL^{-1}H$ has small dimensions (on the order of the number of immersed body points), and can therefore be stored without difficulty.

The matrix is constructed by solving a Poisson problem for each column of H and then applying the action of E.

The simulation for this problem was performed using a finite difference discretization on a uniform grid, with the standard 5 point stencil used for L. The grid spacing of the immersed body was chosen to match that of the solution grid. The numerical solution was obtained on the finite domain $[-1, 1]\times[-1, 1]$; the boundary conditions for ψ were obtained by the exact solution (2.2). In what follows, n_b and n_g are the number of points on the immersed body and the solution domain, respectively.

Figure 2.1 shows that regardless of the choice of smeared delta function, the source term from (2.12) contains spurious oscillations. Moreover, Figure 2.2 demonstrates that these inaccuracies persist as the grid is refined, so that f does not converge to f_{ex} as the grid spacing is decreased. Despite this lack of convergence in f, the integrated source term F and solution ψ converge at first order to F_{ex} and ψ_{ex}, respectively (see Figure 2.2). Convergence of F is a feature of solving (2.12); methods that enforce the boundary constraint approximately contain inaccuracies in F as well as f [36, 87, 94], though these were improved by Yang *et al.* [92]. When used with sufficiently smooth smeared delta functions, the method we propose at the end of this section produces convergent approximations for both.

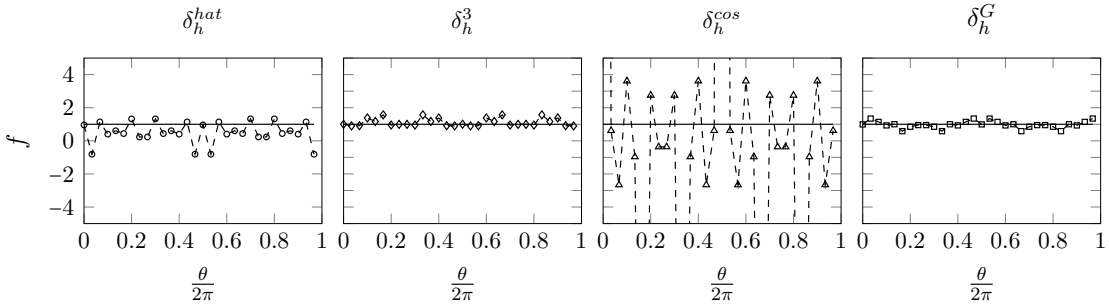

Figure 2.1: Computed source term (f) versus arc length along the cylinder for the Poisson model problem; —: f_{ex}. All plots used $h = 1/640$.

As shown in Figure 2.3, f has the property that Hf does not converge to Hf_{ex} but $EL^{-1}Hf$ converges to $EL^{-1}Hf_{ex}$. By virtue of (2.12), the convergence of $EL^{-1}Hf$ is a statement that using the exact force, f_{ex}, to enforce the boundary condition would lead to a boundary value that is not equal to ψ^Γ but that converges at first order. This intuitive result was also shown by Tornberg and Engquist [83], and will be exploited in what follows to compute accurate approximations to f_{ex}.

To better explain the results of Figure 2.3, we compute the singular value decompo-

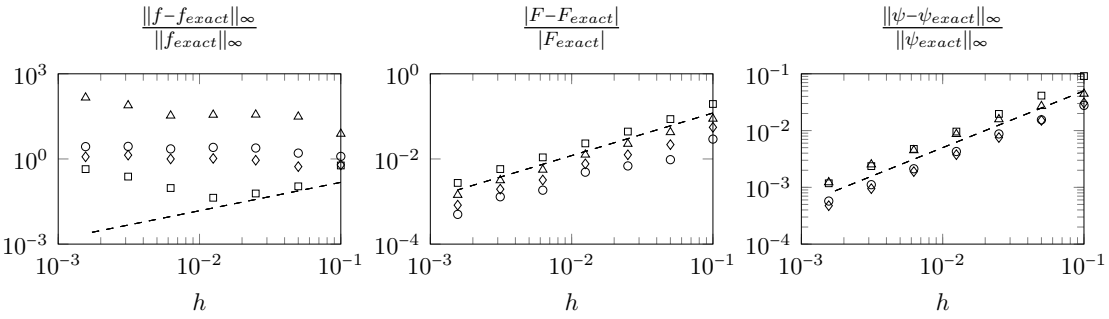

Figure 2.2: Errors in f, F, and ψ versus grid spacing (h) for the Poisson model problem. $\circ$: δ_h^{hat}, $\diamond$: δ_h^3, $\triangle$: δ_h^{cos}, $\square$: δ_h^G, --: first order convergence.

sition (SVD) of EL^{-1}. Let $EL^{-1} = U\Sigma V^T$, where $U \in \mathbb{R}^{n_b \times n_b}$ and $V \in \mathbb{R}^{n_g \times n_b}$ are matrices of left and right orthonormal singular vectors of EL^{-1}, respectively; and $\Sigma \in \mathbb{R}^{n_b \times n_b}$ is a diagonal matrix containing the positive singular values of EL^{-1}. The singular values $\sigma_1, \ldots, \sigma_{n_b}$ are arranged such that $\sigma_1 \geq \sigma_2 \geq \cdots \geq \sigma_{n_b} > 0$, and the singular vectors are notated such that u_j (v_j) is the left (right) singular vector corresponding to σ_j.

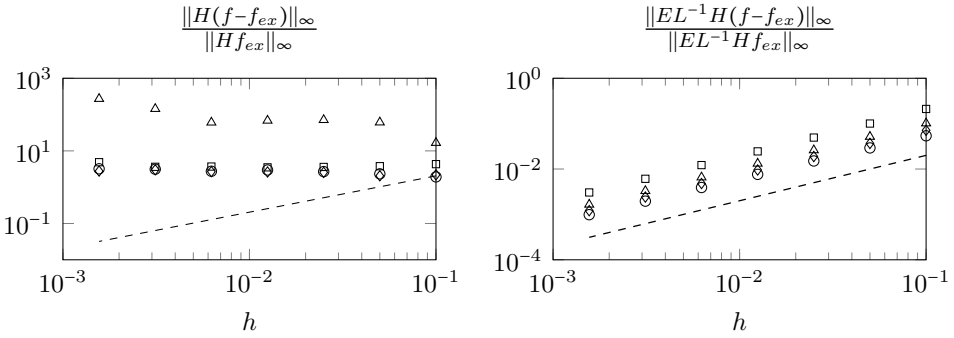

Figure 2.3: Errors in Hf and $EL^{-1}Hf$ versus grid spacing (h) for the Poisson model problem. $\circ$: δ_h^{hat}, $\diamond$: δ_h^3, $\triangle$: δ_h^{cos}, $\square$: δ_h^G, --: first order convergence.

Using this decomposition, Hf_{ex} may be written as a projection onto the basis of vectors formed by V:

$$Hf_{ex} = \sum_{j=1}^{n_b} \alpha_j^{ex} v_j \tag{2.13}$$

and $EL^{-1}Hf_{ex}$ may be expressed as

$$EL^{-1}Hf_{ex} = \sum_{j=1}^{n_b} \alpha_j^{ex} \sigma_j u_j \tag{2.14}$$

where $\alpha_j^{ex} := (v_j^T Hf_{ex})$. Analogous expressions exist for Hf by replacing f_{ex} with f in (2.13) and (2.14). We denote the corresponding coefficients as $\alpha_j := (v_j^T Hf)$.

Using (2.13) and (2.14), Figures 2.3 (a) and (b) show that the sum $\sum_{j=1}^{n_b} \alpha_j$ does not converge to $\sum_{j=1}^{n_b} \alpha_j^{ex}$ under grid refinement, but does converge when scaled by the σ_j. Since EL^{-1} is a discrete integral operator, the σ_j decay to very small values [33] (see Figure 2.4). Thus, the error in the sum $\sum_{j=1}^{n_b} \alpha_j$ stems from the high index coefficients α_j corresponding to the small σ_j. The key to computing accurate source terms is to use a smeared delta function for which the coefficients α_j^{ex} decay as rapidly as possible. The spurious high index coefficients α_j may then be filtered out to obtain physical source terms. By contrast, it is difficult to accurately compute source terms using smeared delta functions for which the α_j^{ex} decay slowly, because the incorrect high index α_j obscure important physical information.

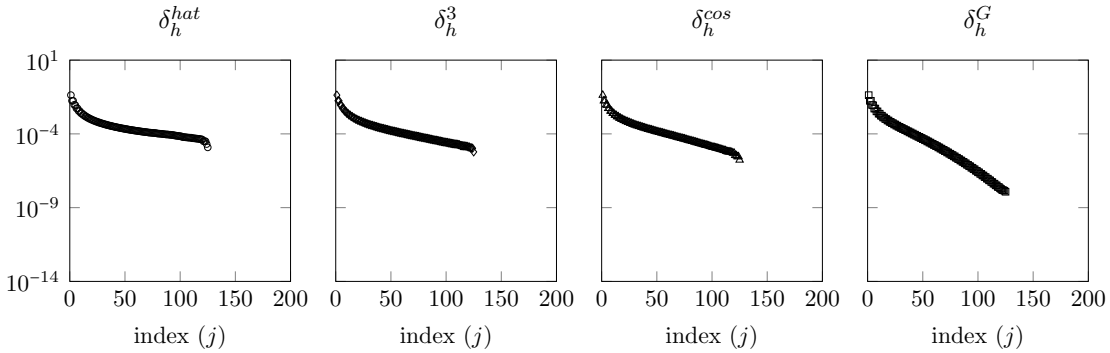

Figure 2.4: Singular values σ_j of EL^{-1} versus index (j) for the Poisson model problem. A grid spacing of $h = 1/80$ was used.

Since EL^{-1} is a discrete integral operator, the basis vectors v_j are closely related to the standard Fourier basis [33], and (2.13) behaves like an expansion of Hf_{ex} in this basis. The decay rate of the coefficients α_j^{ex} is therefore governed by the smoothness of Hf_{ex}, which is determined by the smoothness of the smeared delta function. This is true because Hf_{ex} is a discretization of $\int_\Omega f_{ex}(\boldsymbol{\chi})\delta_h(\mathbf{x}-\boldsymbol{\chi})d\mathbf{x}$, and

$$\frac{d}{d\mathbf{x}}\int_\Omega f_{ex}(\boldsymbol{\chi})\delta_h(\mathbf{x}-\boldsymbol{\chi})d\mathbf{x} = \int_\Omega f_{ex}(\boldsymbol{\chi})\frac{d}{d\mathbf{x}}\delta_h(\mathbf{x}-\boldsymbol{\chi})d\mathbf{x} \tag{2.15}$$

To demonstrate the effect of the smoothness of the smeared delta function on the decay rate of the coefficients α_j^{ex}, we consider a sequence of successively smoother delta functions using the recursive formula developed by Yang *et al.* [92]. Define the operator $\mathcal{S}$ acting on a function $g(r)$ by

$$\mathcal{S}[g(r)] = \int_{r-1/2}^{r+1/2} g(\tilde{r})d\tilde{r} \tag{2.16}$$

Then the functions we consider are $\delta_h^{3,*}(r) = \mathcal{S}[\delta_h^3(r)]$, $\delta_h^{3,**} = \mathcal{S}[\delta_h^{3,*}(r)]$, and δ_h^G, which as a Gaussian may roughly be thought of as the limit of applying $\mathcal{S}$ to δ_h^3

infinitely many times. Note that $\delta_h^3 \in C^1$, $\delta_h^{3,*} \in C^2$, $\delta_h^{3,**} \in C^3$, and $\delta_h^G \in C^\infty$. Figure 2.5 shows that the decay rate of the coefficients α_j^{ex} increases as smoothness of the smeared delta function increases (note the log scale of the y-axis). Note that the compactness of a function in Fourier space is roughly inversely related to its compactness in physical space (see, e.g. [93]), so it is important to pick smeared delta functions whose support is not too narrow.

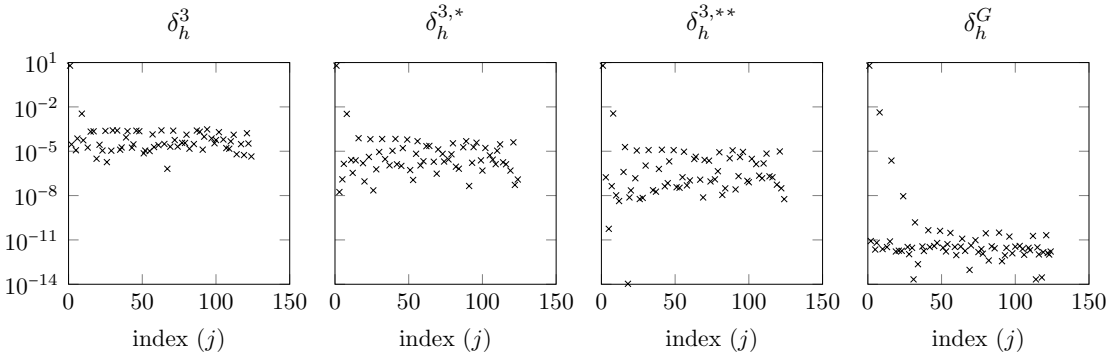

Figure 2.5: Coefficients α_j^{ex} for successively smooth smeared delta functions. Obtained using $h = 1/80$. Note the log scale on the y-axis.

We now discuss the efficient filtering of the spurious high index coefficients α_j. One may in principle filter out the high index coefficients using the SVD of EL^{-1}, but this is a costly procedure. Instead, we penalize the spurious components of f by pre-multiplying it with the matrix $\tilde{E}H$, where $\tilde{E} = E\tilde{W}$ is a weighted interpolant that takes the smeared source term Hf back onto the immersed body while preserving its integral value. The filtered source term is then $\tilde{f} = \tilde{E}Hf$. To give the specific form for $\tilde{W}$, define $\mathbf{1} = [1, 1, \cdots, 1]^T \in \mathbb{R}^{n_g \times 1}$ and let $(H\mathbf{1})_i$ be the i^{th} entry in the vector $H\mathbf{1}$. Then $\tilde{W}$ is a diagonal matrix with entries given by

$$\tilde{W}_{ii} = \begin{cases} 1/(H\mathbf{1})_i, & (H\mathbf{1})_i \neq 0 \\ 0, & \text{else} \end{cases} \tag{2.17}$$

Note that $\tilde{W}$ only applies a nonzero weight if the grid point is within the support of the smeared delta function.

The filter $\tilde{E}H$ redistributes the source term f by convolving it with a kernel of smeared delta functions. The weighting matrix leads to a kernel of the same form as is used in nonparametric kernel smoothing techniques [23], and was inspired from work in this field. As shown below, $\tilde{E}H$ filters the high index coefficients at a rate proportional to the smoothness of the smeared delta function being used. This is

due to the fact that $\tilde{E}H$ is itself an integral operator, and therefore the decay rate of its singular values is governed by the smoothness of its kernel [33].

Figure 2.6 demonstrates the effect of filtering by showing the coefficients α_j^{ex}, α_j and $\tilde{\alpha}_j := (v_j^T H\tilde{f})$. Consistent with the observations made above, the high index coefficients α_j are substantially different from those of α_j^{ex}. For all smeared delta functions, the filtered coefficients are better approximations to the exact coefficients. Noting that $\delta_h^{hat} \in C^0$, $\delta_h^3 \in C^1$, $\delta_h^{cos} \in C^0$, and $\delta_h^G \in C^\infty$, it is clear from Figure 2.6 that the absolute error in the high frequency $\tilde{\alpha}_j$ decreases as the smoothness of the smeared delta function increases. This is because the magnitude of the high index coefficients α_j^{ex} is smaller for smoother smeared delta functions, so the spurious high index α_j may be filtered more aggressively.

Figure 2.7 shows the filtered source terms as a function of arc length along the cylinder. By comparison with Figure 2.1, it is clear that the filtered surface stresses are better representations of f_{ex} than their unfiltered counterparts. Moreover, note from Figure 2.7 that the approximation to f_{ex} improves as the smoothness of the smeared delta function increases. This argument is shown quantitatively by the error plot from Figure 2.8. Indeed, the infinitely differentiable δ_h^G yields an $\tilde{f}$ that converges to f_{ex}. The inability to compute convergent source terms using δ_h^{hat}, δ_h^3, and δ_h^{cos} stems from the slow decay rate of the coefficients α_j^{ex}. By contrast, accurate approximations to f_{ex} can be obtained for δ_h^G by simply removing the high index coefficients of α_j.

Note also that it is only the smoothness of the smeared delta functions that matters; δ_h^{hat}, δ_h^3, and δ_h^G all satisfy the same number of discrete moment conditions, and the derivative of δ_h^3 satisfies two more discrete moment conditions than δ_h^G. Last, see from Figure 2.8 that filtering does not affect F by virtue of the way $\tilde{E}H$ was constructed, and that the error in the solution ψ is unchanged because computing $\tilde{f}$ is a post-processing step. For these reasons, we may write F and ψ without the tilde.

It would be desirable to determine *a priori* the appropriate differentiability of a smeared delta function for a given tolerance in the accuracy of the surface stress. Yet, this is perhaps not possible, as each smeared delta function is associated with a distinct decay rate in singular values and a unique set of singular vectors. For example, $\delta_h^{cos}, \delta_h^{hat} \in C^0$, but each is associated with different error bounds in the computed surface stress (see figure 2.3). Thus, this chapter provides the general result that smeared delta functions of increasing differentiability have associated sin-

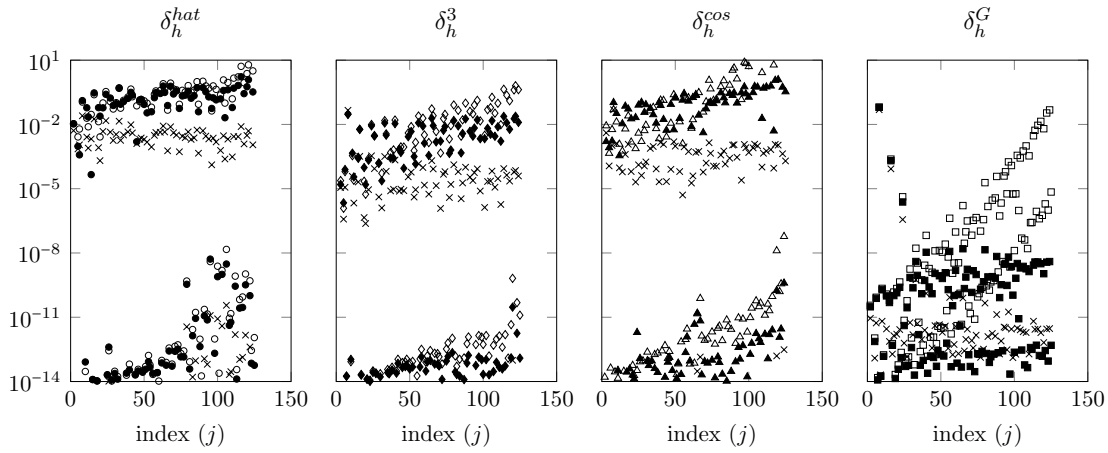

Figure 2.6: Coefficients α_j^{ex} ($\times$), α_j (open markers) and $\tilde{\alpha}_j$ (filled markers) for the Poisson model problem. Note the log scale on the y-axis. The grid spacing $h = 1/80$ was used.

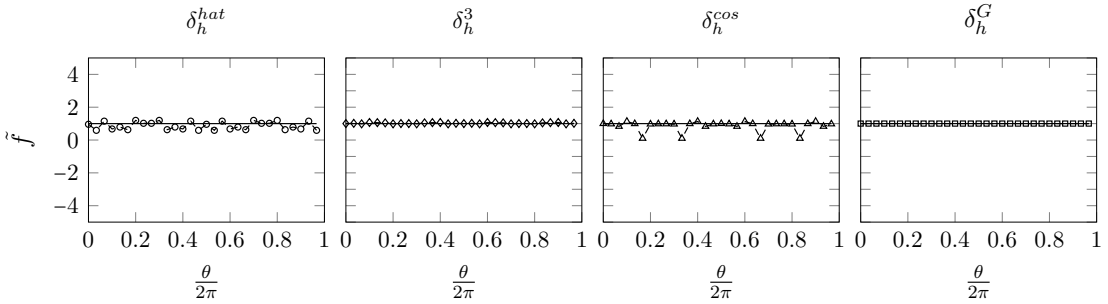

Figure 2.7: $\tilde{f}$ vs arc length along the cylinder for the Poisson problem. The exact solution f_{ex} is given by the solid line (—) for reference.

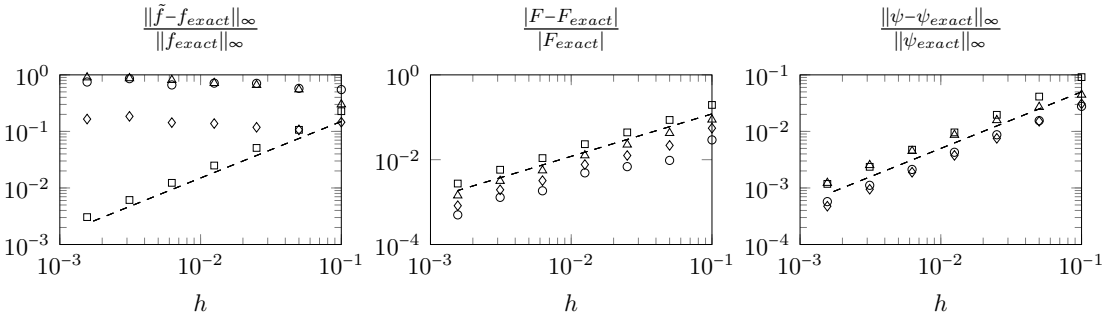

Figure 2.8: Errors in $\tilde{f}$, F, and ψ versus grid spacing (h) for the Poisson problem. $\circ$: δ_h^{hat}, $\diamond$: δ_h^3, $\triangle$: δ_h^{cos}, $\square$: δ_h^G, --: first order convergence.

gular values and exact stress coefficients α_j^{ex} that decay more quickly, and describes a procedure to compute accurate surface stresses from this result. Establishing error bounds for specific smeared delta functions or classes of smeared delta functions remains an open question.

Finally, it is worth mentioning other possibilities for accurately computing source terms. First, there might be adequately differentiable functions of narrower support than δ_h^G that are sufficiently compact in Fourier space to provide convergent source terms. Second, one may use standard regularization techniques that have been developed for first-kind integral equations, such as Tikhonov reguarization, to compute convergent source terms irrespective of delta function. The difficulty in using these techniques is that they involve a free parameter, and our experience has been that a costly SVD is required to determine this parameter so that the source term converges.

2.3 Extension to accurately computing surface stresses and forces

In this section, we consider surface-velocity based IB methods that use a singular source term in the momentum equations. We show that these methods require the solution of a discrete integral equation of the first kind to compute the surface stresses on an immersed body. Therefore, the conclusion that smoother smeared delta functions lead to faster decay of coefficients for the exact surface stresses still holds. Moreover, sufficiently smooth smeared delta functions may be used in combination with the filter $\tilde{E}H$ to obtain surface stresses and forces that converge to the actual stresses and forces on the immersed body.

The nondimensionalized Navier-Stokes equations are considered here on a domain Ω containing a body whose boundary is denoted by Γ. The governing equations for surface velocity-based IB methods are written as

$$\frac{\partial \mathbf{u}}{\partial t} + \mathbf{u}\cdot\nabla\mathbf{u} = -\nabla p + \frac{1}{Re}\nabla^2\mathbf{u} + \int_\Gamma \mathbf{f}(\boldsymbol{\chi}(s',t))\delta(\mathbf{x}-\boldsymbol{\chi}(s',t))ds' \tag{2.18}$$

$$\nabla\cdot\mathbf{u} = 0 \tag{2.19}$$

$$\int_\Omega \mathbf{u}(\mathbf{x})\delta(\mathbf{x}-\boldsymbol{\chi}(s,t))d\mathbf{x} = \mathbf{u}^\Gamma(\boldsymbol{\chi}(s,t),t) \tag{2.20}$$

where $\mathbf{f}(\boldsymbol{\chi}(s',t))$ represents the surface stresses that arise to enforce the boundary condition (2.20). As with the previous section, all IB methods replace the Dirac delta functions in (2.18) and (2.20) with smeared delta functions δ_h.

It is well known that many discretizations of (2.18)–(2.20) involve solving a discrete Poisson or Poisson-like equation for either the pressure (primitive variable formulations) or for the streamfunction (vorticity-streamfunction formulations). An analogous situation occurs for the surface stresses, except that the equation is an integral equation. This can be seen by multiplying (2.18) by $\delta_h(\mathbf{x}-\boldsymbol{\chi}(s,t))$ and

integrating over the domain. Doing this gives

$$\begin{aligned}&\int_\Omega \int_\Gamma \mathbf{f}(\boldsymbol{\chi}(s',t))\delta_h(\mathbf{x}-\boldsymbol{\chi}(s,t))\delta_h(\mathbf{x}-\boldsymbol{\chi}(s',t))ds'd\mathbf{x} = \\ &\int_\Omega \left[\left(\frac{\partial}{\partial t}-\frac{1}{Re}\nabla^2\right)\mathbf{u}(\mathbf{x})+\mathbf{u}\cdot\nabla\mathbf{u}+\nabla p\right]\delta_h(\mathbf{x}-\boldsymbol{\chi}(s,t))d\mathbf{x}\end{aligned} \tag{2.21}$$

The key point is that all IB methods replace the delta function with a smeared delta function in the governing equations. Had the Dirac delta function been kept, the integral equation (2.21) would trivially reduce to an expression for the surface stresses $\mathbf{f}(\boldsymbol{\chi}(s,t))$. As in (2.5), the integral operator of (2.21) has an unbounded inverse because it contains a continuous kernel for any finite h.

Many discretizations of (2.18)–(2.20) involve solving a discretized integral equation of the first kind for the surface stresses. Spatially discretizing (2.18)–(2.20) leads to a system of differential algebraic equations given by

$$\dot{u} + \mathcal{N}(u) = -Gp + Lu + Hf \tag{2.22}$$

$$Du = 0 \tag{2.23}$$

$$Eu = u^\Gamma \tag{2.24}$$

where the overdot denotes differentiation with respect to time; u, p, and f denote the spatially discrete velocity, pressure, and surface stresses; $\mathcal{N}(u)$ is a discretization of the nonlinear term; G, L, and D are discretizations of the gradient, Laplacian, and divergence operators, respectively; and $H(\cdot)$ and $E(\cdot)$ are discretizations of the operations $\int_\Gamma(\cdot)\delta_h(\mathbf{x}-\boldsymbol{\chi})ds$ and $\int_\Omega(\cdot)\delta_h(\mathbf{x}-\boldsymbol{\chi})d\mathbf{x}$, respectively.

Consider a time discretization that treats the nonlinear term explicitly and the viscous term implicitly. Then (2.22)–(2.24) become a linear system of equations of the form

$$\begin{bmatrix} A & G & H \\ D & 0 & 0 \\ E & 0 & 0 \end{bmatrix}\begin{bmatrix} u_{n+1} \\ p_{n+k_1} \\ f_{n+k_2} \end{bmatrix} = \begin{bmatrix} r_1 \\ r_2 \\ u^\Gamma_{n+1} \end{bmatrix} \tag{2.25}$$

where $0 < k_1, k_2 \leq 1$, $A = \frac{1}{\Delta t}I - \alpha L$ ($\alpha \in \mathbb{R}$) comes from the implicit treatment of the viscous term, and r_1 and r_2 are known right hand side terms arising from the explicit time discretization and boundary conditions of the spatial derivative operators.

The system (2.25) is valid for a variety of discretizations. Multistep methods lead to a system of the form of (2.25), and many Runge-Kutta methods involve solving a

system such as (2.25) at each stage. If the viscous term were treated explicitly then A would be replaced with $\frac{1}{\Delta t}I$, though none of the ensuing conclusions would be affected by this change.

Solving (2.25), as is done in the current work, leads to a velocity field that satisfies the boundary conditions on the immersed body at time t_{n+1} [15, 38, 45, 79]. Other surface-velocity based IB methods compute f_{n+k_2} using u_n, rather than u_{n+1} [36, 87, 92, 94], which produces a velocity field that does not exactly satisfy the boundary conditions at each time step. We argue in this section that in either case the equation for the surface stresses is an integral equation, and therefore that the results of section 2.2 are valid for either approach.

For the methods that solve (2.25), the equation for the surface stresses may be derived by a block-LU factorization of (2.25) (see reference [79]). Doing this gives

$$EBHf_{n+k_2} = r_3 \tag{2.26}$$

where r_3 is known and $B = (A^{-1}G(DA^{-1}G)^{-1}D - I)A^{-1}$. The form of B arises because of the time discretization of the system (2.22)–(2.24) and the factorization of (2.25). Equation (2.26) is an approximation of the continuous equation (2.21), and therefore is a discrete integral equation of the first kind. Thus, the logic of section 2.2 applies: smoother delta functions may be used to expand the exact surface stresses on the body using very few terms, and may therefore be combined with the filter $\tilde{E}H$ to compute accurate surface stresses and forces. It should be mentioned that an analog of the system (2.25) can be formulated in a streamfunction-vorticity formulation [15]. It can be shown that this formulation still leads to a discrete integral equation of the first kind whose kernel is modified from (2.21) by the presence of discrete curl operators. The conclusions of section 2.2 are thus still applicable.

We now show that the methods that use u_n to compute f_{n+k_2} also contain an integral equation of the first kind for the surface stresses. In the notation of the current work, the expression for the surface stresses used in references [36, 87, 92, 94] is given by

$$EHf_{n+k_2} = \frac{u^{\Gamma}_{n+1} - Eu_n}{\Delta t} + E(\mathcal{N}(u_{n+k_3}) + Gp_{n+k_4} + Lu_{n+k_5}) \tag{2.27}$$

where $0 \leq k_3, k_4, k_5 < 1$, and all terms on the right hand side are known. This is a discrete integral equation of the first kind whose kernel corresponds to that of (2.21).

As an approximation, references [36, 87, 92, 94] replace the matrix EH in (2.27) with the identity matrix, which corresponds to replacing the kernel in (2.21) with an

invertible kernel given by the Dirac delta functions. This approximation produces non-convergent surface stresses and forces, though Yang *et al.* [92] reduced the error in the surface forces. We argue that the root cause of the spurious surface stresses computed by these methods is the nature of the underlying discrete integral equation (2.27), and that the methods of section 2.2 may be used to obtain convergent surface stresses and forces.

Both (2.26) and (2.27) have a time-dependence that was not present in the Poisson problem of section 2.2. For time-dependent problems, the filtering procedure is performed at the end of a given time step. Note also that since the spurious stresses do not affect the accuracy of the velocity field, the filtered stresses do not need to be incorporated into the time-stepping algorithm, even if it requires information of the surface stress at previous time steps (multistep methods) or stages (Runge-Kutta methods). Thus, the time-dependence of the Navier-Stokes equations does not affect the view of the filtering technique as a post-processing procedure.

In the remainder of this paper, we use the IBPM [15] to illustrate that computing surface stresses and forces using the filter $\tilde{E}H$ leads to increasingly accurate surface stresses as the smoothness of the smeared delta function is increased. We further show that a sufficiently smooth smeared delta function may be used to obtain convergent stresses and forces. These results are demonstrated for multiple test problems.

2.4 An impulsively rotated cylinder

Consider an infinitely long (2-D), infinitely thin cylinder of radius R in a quiescent fluid that is impulsively brought from rest to constant angular velocity ω. Fluid exists inside and outside of the cylinder. All quantities in this section are dimensionless: length scales are nondimensionalized by R, velocities are nondimensionalized by ωR, and time is nondimensionalized by ω.

The exact velocity field is in the azimuthal direction, and is given in polar coordinates by $\mathbf{u}_{ex} = u_{ex}(r,t)\mathbf{e}_\theta$. It may be written as

$$u_{ex}(r,t) = \begin{cases} r + 2\sum_{n=1}^{\infty} \frac{J_1(\sqrt{\lambda_n} r)}{\sqrt{\lambda_n} J_0(\sqrt{\lambda_n})} e^{\frac{-\lambda_n t}{Re}}, & r \leq 1 \\ \mathcal{L}^{-1}\left[\frac{K_1\left(r\sqrt{sRe}\right)}{sK_1(\sqrt{sRe})}\right], & r > 1 \end{cases} \tag{2.28}$$

In the above, Re is the Reynolds number; J_p is the p^{th} Bessel function of the first kind; $\sqrt{\lambda_n}$ is the n^{th} root of J_1; K_1 is the 1^{st} modified Bessel function of the first kind;

and $\mathcal{L}^{-1}[\cdot]$ represents the inverse Laplace transform with respect to the variable s.

The exact surface stress is also in the azimuthal direction ($\mathbf{f}_{ex} = f_{ex}\mathbf{e}_\theta$), and is given by summing the contributions on the inside and outside of the cylinder surface:

$$f_{ex}(t) = \frac{2}{Re}\left[\frac{\partial}{\partial r}\left(\frac{u_{ex}}{r}\right)\right]_{r=1^-} + \frac{2}{Re}\left[\frac{\partial}{\partial r}\left(\frac{u_{ex}}{r}\right)\right]_{r=1^+} \tag{2.29}$$

$$= \frac{4}{Re}\sum_{n=1}^{\infty} e^{\frac{-\lambda_n t}{Re}} + \frac{2}{Re}\left[\frac{\partial}{\partial r}\left(\frac{u_{ex}}{r}\right)\right]_{r=1^+} \tag{2.30}$$

The second term on the right hand side of (2.30) is difficult to express analytically by virtue of the inverse Laplace transform in (2.28), but it can be evaluated using numerical routines. Note that the exact stresses are not spatially constant in the Cartesian coordinate system in which the IBPM is formulated, which makes this model problem a more stringent test than if the numerical solution was obtained using a cylindrical polar coordinate system.

The exact surface force in the azimuthal direction (F_{ex}) is obtained by integrating (2.30) along the surface of the cylinder:

$$F_{ex}(t) = 2\pi f_{ex}(t) \tag{2.31}$$

The inverse Laplace transform was computed using the built-in MATLAB implementation of the Talbot inversion procedure. The inversion is poorly conditioned near the surface of the cylinder, and computations within a radial distance of 0.05 of the cylinder surface were performed in variable precision arithmetic. All quantities in the exact solution (2.28), (2.30), and (2.31) were converged to within 10^{-10}. We compare this exact solution to the IBPM using the smeared delta functions introduced in section 2.2. We ran tests for Reynolds numbers ranging from $Re = 10$ to $Re = 200$. In the interest of brevity, we primarily show results for $Re = 10$, with supplementary results given for $Re = 200$.

All simulations used a multidomain approach: fine grids were placed near the immersed body and coarser grids were employed as distance from the immersed body increased. In all results shown below, the cylinder of dimensionless radius 1 was centered at $[0, 0]$; the finest mesh was placed on a subdomain of size $[-2.5, 2.5]\times[-2.5, 2.5]$, and the total flow domain size was $[-20, 20]\times[-20, 20]$. The grid spacing on the immersed surface was selected to match that of the $[-2.5, 2.5] \times [-2.5, 2.5]$ sub-domain, and the time step was selected so that the CFL number with respect to

the angular velocity of the cylinder was kept at 0.1. In what follows, h is defined as the grid spacing on the $[-2.5, 2.5] \times [-2.5, 2.5]$ subdomain.

Figure 2.9 demonstrates that for $Re = 10$, the filtered stresses are better approximations to f_{ex} than the unfiltered stresses. Morever, the quality of the approximation of the filtered stress is better for smoother smeared delta functions (see also the error in the filtered stresses from Figure 2.10). Indeed, the use of δ_h^G leads to filtered surface stresses that converge to the analytical solution f_{ex}.

In analogy with section 2.2, the surface forces converge irrespective of smeared delta function (see Figures 2.10 2.11). This is a consequence of solving the discrete integral equation (2.26) to explicitly enforce the boundary condition. The surface velocity-based IB methods that use (2.27) to approximately enforce this condition are known to obtain non-convergent surface forces [92]. Note also that the velocity field converges at first order for all smeared delta functions. In keeping with the notation of section 2.2, tildes are not placed on the variables F and u to emphasize that these quantities are not affected by the filtering procedure. Figure 2.12 shows the errors in $\tilde{f}$, F, and u at $Re = 200$ to highlight the applicability of these results over a range of Reynolds numbers.

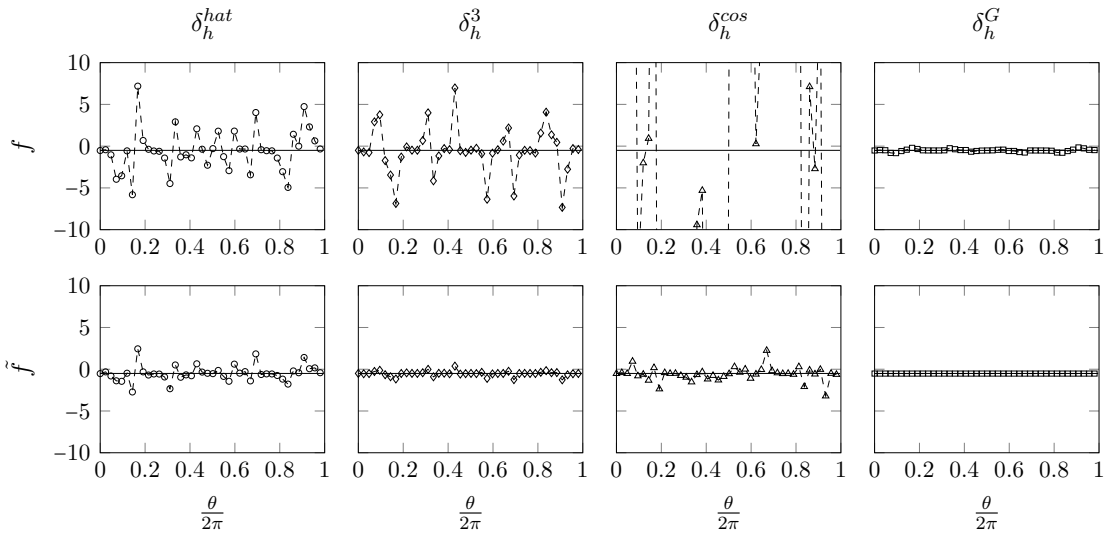

Figure 2.9: Top row: tangential surface stress without filtering (f) versus arc length along the cylinder for the rotating cylinder problem at $Re = 10$. Bottom row: filtered surface stresses ($\tilde{f}$) versus arc length along the cylinder at $Re = 10$; —: f_{ex}. All plots used $h = 5/200$.

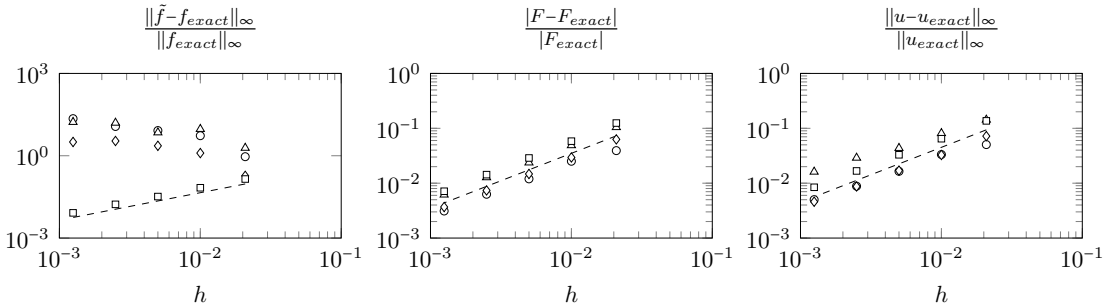

Figure 2.10: Errors in $\tilde{f}$, F, and u versus grid spacing (h) for the rotating cylinder problem at $Re = 10$. ○: δ_h^{hat}, ◇: δ_h^3, △: δ_h^{cos}, □: δ_h^G, --: first order convergence.

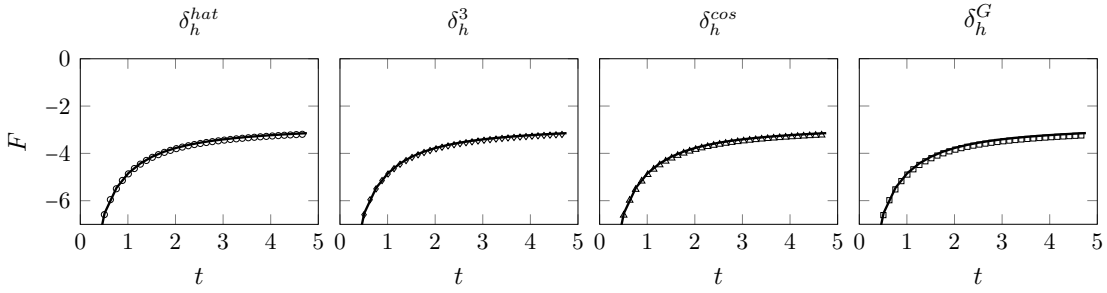

Figure 2.11: Tangential surface force, F, versus time for the rotating cylinder problem at $Re = 10$; —: F_{ex}. The same grid spacing as in Figure 2.9 was used.

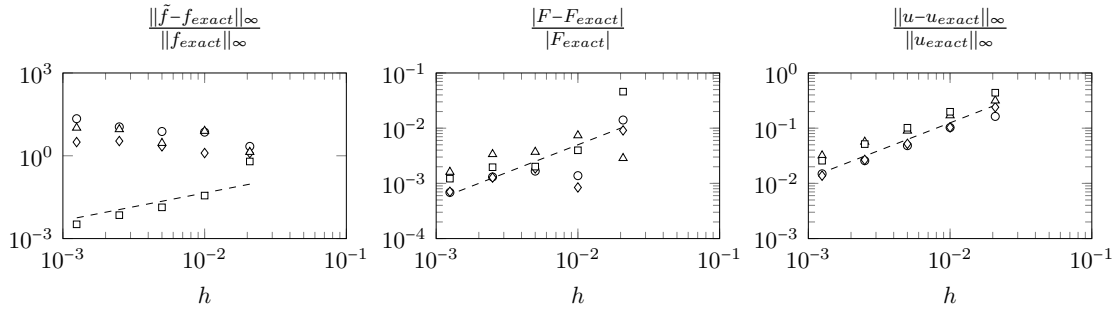

Figure 2.12: Errors in $\tilde{f}$, F, and u versus grid spacing (h) for the rotating cylinder problem at $Re = 200$. ○: δ_h^{hat}, ◇: δ_h^3, △: δ_h^{cos}, □: δ_h^G, --: first order convergence.

2.5 A cylinder in cross-flow

We now consider the canonical problem of flow over an infinitely long (2D) cylinder of diameter D that is impulsively brought to translation at speed U. All quantities are dimensionless; length scales, velocity scales, and time scales are nondimensionalized by U, D, and U/D, respectively. Since there is no known analytical solution to this flow, we will present results at $Re = 200$ to compare with other numerical and experimental results. This flow is well known to exhibit a vortex shedding instability, which we trigger in our simulations using an asymmetric body force at

early time. In the interest of brevity, we only present the filtered stresses $\tilde{f}$ for this problem, though the result from sections 2.2 and 2.3 that filtering provides better approximations to the physically correct surface stresses remains true here as well. The surface stresses associated with this flow exhibit substantial spatial variation, which attests to the ability of this method to compute convergent surface stresses for a variety of complicated flows.

In all results shown below, the cylinder of dimensionless diameter 1 was centered at $[0, 0]$; the finest mesh was placed on a subdomain of size $[-1.5, 2.5]\times[-2, 2]$, and the total flow domain size was $[-12, 20] \times [-16, 16]$. The grid spacing on the immersed surface was selected to match that of the $[-1.5, 2.5] \times [-2, 2]$ sub-domain, and the time step was selected so that the CFL number with respect to the translational speed of the cylinder was 0.1. In what follows, h is defined as the grid spacing on the $[-1.5, 2.5] \times [-2, 2]$ subdomain. We define the quantities of interest for this 2-D flow as $\tilde{f} = [\tilde{f}_x,\ \tilde{f}_y]^T$, $F = [C_D,\ C_L]^T$, and $u = [u_x,\ u_y]$, where C_D and C_L denote the dimensionless x and y surface forces, respectively.

Figure 2.13 demonstrates that the unphysical oscillations of the surface stresses $\tilde{f} = [\tilde{f}_x,\ \tilde{f}_y]^T$ are reduced for the smoother smeared delta functions. To demonstrate this quantitatively, we perform a convergence analysis by computing the infinity norm of the difference between $\tilde{f}_x$, C_D, and u_x and the corresponding quantities obtained on a fine grid solution using δ_h^G with grid spacing $h = 4/3072 \approx 0.001$. Similar results would be obtained using the y-components of $\tilde{f}$, F, and u. As with sections 2.2 and 2.3, δ_h^G yields surface stresses $\tilde{f}$ that converge to the fine-grid surface stress, but all smeared delta functions lead to convergent surface forces and velocities (see Figure 2.14). As before, the tildes are removed from force and velocity variables to emphasize that they are not affected by filtering.

As seen in Figure 2.15, the present work faithfully replicates the well known periodic oscillations exhibited by C_D and C_L once the flow enters its limit cycle vortex shedding behavior. Table 2.1 shows that the amplitude and dimensionless frequency (St) associated with these oscillations agree well with several previous experiments and simulations. This further demonstrates that accurate integral force values may be obtained irrespective of smeared delta function. Note by Figure 2.14 that the integrated force is the same to within 10^{-3} for all smeared delta functions considered. For simplicity we therefore only provide one value in Table 2.1 with the understanding that it is representative of all smeared delta functions.

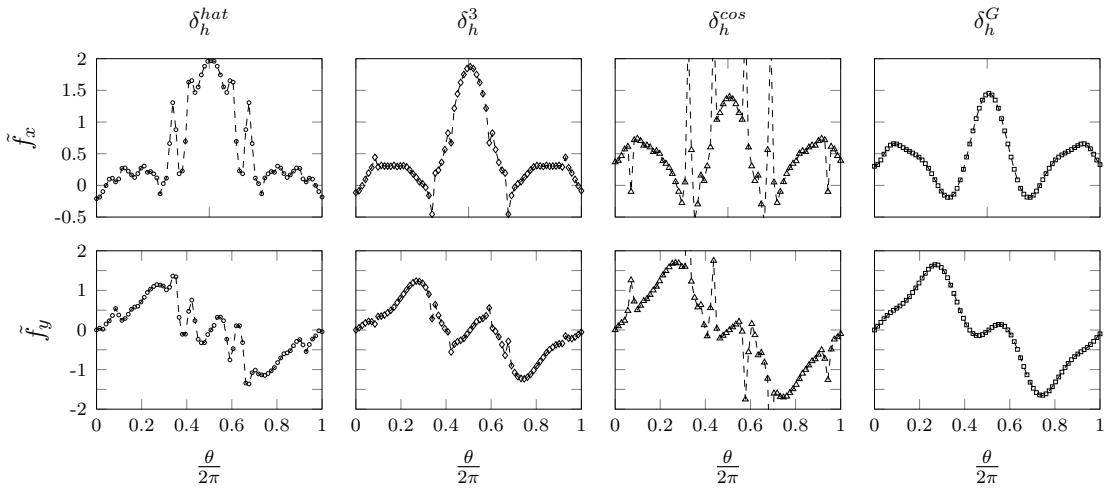

Figure 2.13: Filtered x and y component of the surface stress versus arc length along the cylinder for the cylinder in cross-flow problem. All plots used $h = 4/768$.

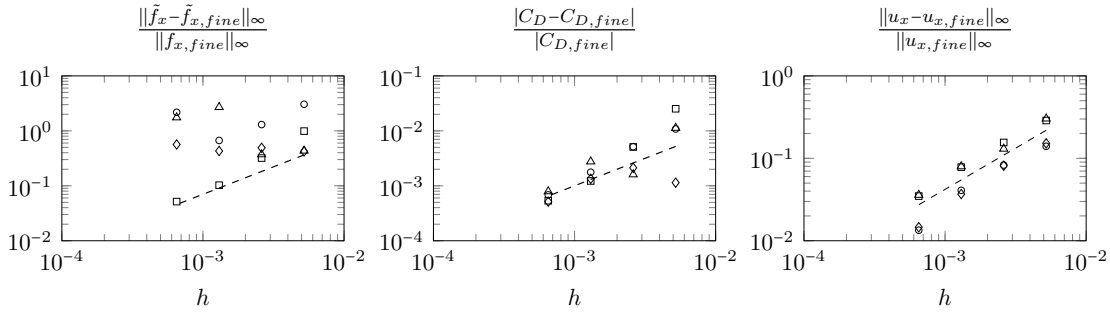

Figure 2.14: Errors in $\tilde{f}_x$, C_D, and u_x versus grid spacing (h) for the cylinder in cross-flow problem. ○: δ_h^{hat}, ◇: δ_h^3, △: δ_h^{cos}, □: δ_h^G, --: first order convergence.

	St	C_D	C_L
[7]	0.193	1.19 ± 0.042	±0.64
[52]	0.192	1.31 ± 0.049	±0.69
[44]	0.190		
[65]	0.19		
[79]	0.196	1.35 ± 0.048	±0.68
Present	0.198	1.35 ± 0.046	±0.70

Table 2.1: A comparison of of the dimensionless frequency (St) and amplitude of surface force oscillations

2.6 Conclusions

The source of the inaccurate surface stresses and forces obtained by a class IB methods was identified: for any smeared delta function used, the equation for the surface stresses is an ill-posed integral equation of the first kind. As a result, the surface stresses computed from this equation have high frequency components

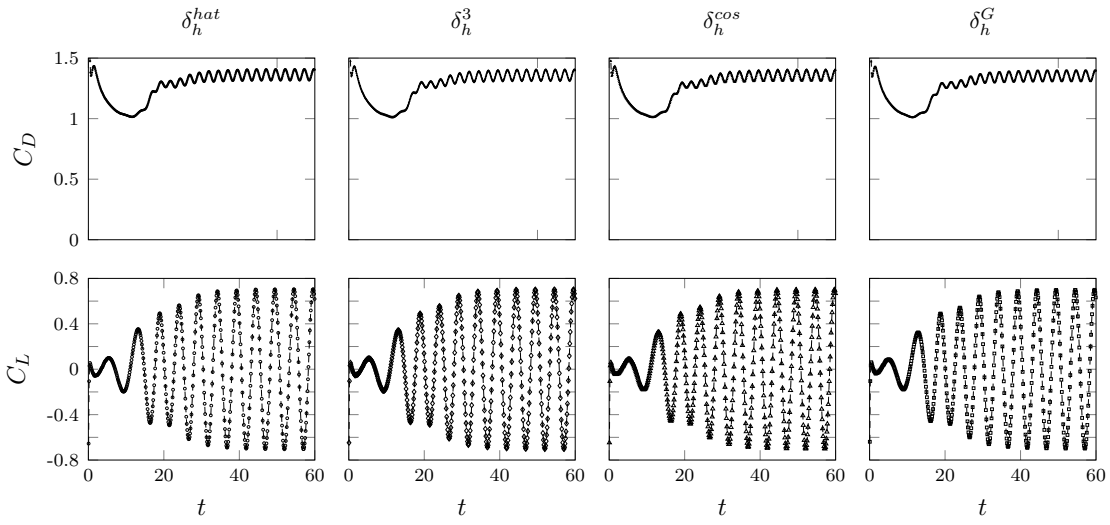

Figure 2.15: Coefficients of lift and drag on the cylinder versus time for the cylinder in cross-flow problem. The same grid spacing as in Figure 2.13 was used.

that are erroneously amplified. We also demonstrated that the amplitude of the high frequency components of the physically correct surface stresses decreases as smoother smeared delta functions are used. Thus, for sufficiently smooth smeared delta functions, the incorrectly computed high frequency components may simply be filtered out to obtain accurate approximations to the actual stresses. We developed an efficient filtering technique that leads to better representations of the physical stresses than those obtained without filtering, and established that combining this filtering technique with an adequately smooth smeared delta function leads to surface stresses and forces that converge to the physical stresses and forces on the body. The filtering procedure is applied as a post-processing step, so it does not alter the convergent velocity field. We demonstrated the efficacy of the technique on two flow problems, flow in and around a rotating cylidner and flow over a circular cylinder, and demonstrate converged surface stresses in both cases.

Chapter 3

AN EFFICIENT IMMERSED-BOUNDARY METHOD FOR FLUID-STRUCTURE INTERACTION[1]

3.1 Introduction

We present in this chapter an IB method for fully-coupled FSI problems. Our method is strongly-coupled; *i.e.*, it strictly enforces the nonlinear constraint between the fluid and the structure at each time instance. Enforcing this constraint is necessary for simulations involving large structural motions (weakly coupled IB methods do not impose the constraint and are unstable for small structure-to-fluid mass ratios and large body motions [10, 12, 25]).

Due to the nonlinear nature of the constraint, most strongly-coupled methods must solve a large nonlinear system of equations at each time step. The block Gauss-Seidel procedure is one approach to solving this nonlinear system. It is attractive for its ease of implementation, but requires relaxation to converge for a wide range of mass ratios. Employing relaxation requires a heuristically chosen parameter, and can involve dozens of iterations to converge for small mass ratios [82], though Wang and Eldredge [88] improved this convergence behavior using information about the system's added mass. Alternatively, the nonlinear system can be solved with a Newton-Raphson method. This removes the need of free parameters, and typically requires a small number of iterations irrespective of the mass ratio. However, this approach often involves computing several matrix-vector products per time step, each involving large Jacobian matrices [19, 34, 59].

In the context of rigid body FSI problems, some strongly-coupled methods evaluate the constraint equation at the previous time step, which allows for the resulting equations of motion to be linear [43, 91]. Thus, these methods do not require iterations, though the temporal accuracy is reduced to first order due to the time lag introduced in the constraint. It is difficult to avoid iteration in deforming body problems, since the structure equations have a nonlinear stiffness term that is frequently treated implicitly when discretized in time.

[1] This chapter is based on the publication Goza and Colonius [28], for which my contributions were devising and implementing the numerical method, running all simulations, and being the primary author of the article.

Our strongly-coupled IB method iteratively solves the nonlinear algebraic equations using a linearization of the system, as is done in the Newton-Raphson approach. Therefore, our method does not require free relaxation parameters, and has exhibited fast convergence behavior for all problems we have considered so far. A distinction between our method and a standard Newton-Raphson implementation is that we avoid large Jacobian matrices by performing a block-LU factorization of the linearized system. This reduces all iterations to subsystems whose dimensions scale with the number of discretization points on the immersed surface, rather than on the entire flow domain.

Our method treats the fluid with the two-dimensional (2D) discrete streamfunction formulation of Colonius and Taira [15], and the structure with a finite element formulation that applies to various structural materials undergoing large deformations and rotations. Our method is valid for problems involving fairly general thin elastic structures, and we verify it on 2D test problems of flow past deforming flags. The test problems involve large body motions and a wide range of mass ratios, and for all cases our proposed iteration process required a small number of iterations to converge. To supplement the 2D method, we derive an analogous method that treats the fluid with primitive variables at the end of this chapter. This primitive-variable formulation has a similar iteration procedure to the proposed 2D formulation, and can be applied in both 2D and 3D.

3.2 Governing equations

The governing equations take the same form as in (2.18)–(2.20), though there is now an additional equation associated with the deformation of the structure. The fully-coupled equations are written as

$$\frac{\partial \mathbf{u}}{\partial t} + \mathbf{u} \cdot \nabla \mathbf{u} = -\nabla p + \frac{1}{\mathrm{Re}} \nabla^2 \mathbf{u} + \int_\Gamma \mathbf{f}(\boldsymbol{\chi}(s,t)) \delta(\boldsymbol{\chi}(s,t) - \mathbf{x}) ds \tag{3.1}$$

$$\nabla \cdot \mathbf{u} = 0 \tag{3.2}$$

$$\frac{\rho_s}{\rho_f} \frac{\partial^2 \boldsymbol{\chi}}{\partial t^2} = \frac{1}{\rho_f U_\infty^2} \nabla \cdot \boldsymbol{\sigma} + \mathbf{g}(\boldsymbol{\chi}) - \mathbf{f}(\boldsymbol{\chi}) \tag{3.3}$$

$$\int_\Omega \mathbf{u}(\mathbf{x}) \delta(\mathbf{x} - \boldsymbol{\chi}(s,t)) d\mathbf{x} = \frac{\partial \boldsymbol{\chi}(s,t)}{\partial t} \tag{3.4}$$

where ρ_s is the structure density, the term $\mathbf{g}$ represents a body force per unit volume (e.g. gravity) applied to the immersed body, the other variables retain their same definition as in chapter 2, and the structural equations (3.3) were divided by $\rho_f U_\infty^2 / L$ to arrive at the form seen above.

Note that making the structural displacement $\boldsymbol{\chi}$ an unknown leads not only to the new equation (3.3), but also results in a modification to the no-slip condition (3.4): this boundary condition still reflects the interface constraint between the fluid and structure, but now the right-hand-side term is the unknown structural velocity rather than a prescribed body velocity. As in chapter 2, the term $\mathbf{f}(\boldsymbol{\chi})$ arises to enforce this no-slip constraint. The presence of $\mathbf{f}$ in (3.1) represents the surface stress imposed on the fluid by the immersed body. This can be seen by multiplying the momentum equations (3.1) by $\delta(\mathbf{x} - \boldsymbol{\chi}(s,t))$ and integrating over the domain Ω to get

$$\mathbf{f}(\boldsymbol{\chi}(s,t)) = \left[\left(\frac{\partial}{\partial t} - \frac{1}{Re}\nabla^2\right)\mathbf{u} + \mathbf{u}\cdot\nabla\mathbf{u} + \nabla p\right]\Big|_{\mathbf{x}=\boldsymbol{\chi}(s,t)} \qquad \forall\ \boldsymbol{\chi} \in \partial\Gamma \tag{3.5}$$

Note that $-\mathbf{f}$ is present in the structural equations (3.3) since by Newton's third law this term represents the stress imposed on the immersed body by the fluid (including added mass effects). The presence of $\mathbf{f}$ in the structural equations (3.3) requires that the surface stresses be computed accurately, and we therefore incorporate the procedure of chapter 2 into the numerical method described in the subsequent section.

In (3.3), the time derivative is understood to be a Lagrangian derivative, and the stress tensor used is the Cauchy stress, which is related to the second Piola-Kirchoff stress in the undeformed configuration, $\boldsymbol{\sigma}^K$, by

$$\sigma_{mn} = \frac{1}{J}\frac{\partial x_m}{\partial \chi_i^0}\frac{\partial x_n}{\partial \chi_j^0}\sigma_{ij}^K \tag{3.6}$$

where $\boldsymbol{\chi}^0$ is the position of the body in its undeformed configuration, and $J = \det(\partial x_i/\partial \chi_j^0)$. The second Piola-Kirchoff stress is related to the strains within the structure via

$$\sigma_{ij}^K = D_{ijkl}E_{kl} \tag{3.7}$$

where $\mathbf{D}$ depends on Young's Modulus, E, the bulk shear modulus, G, and Poisson's ratio, ν_s; and $\mathbf{E}$ is the strain tensor given by

$$E_{ij} = \frac{1}{2}\left(\frac{\partial \chi_i}{\partial \chi_j^0} + \frac{\partial \chi_j}{\partial \chi_i^0} + \frac{\partial \chi_m}{\partial \chi_i^0}\frac{\partial \chi_m}{\partial \chi_j^0}\right) \tag{3.8}$$

(summation implied on repeated indices). Again, all variables that comprise $\mathbf{E}$ were nondimensionalized using the characteristic length L.

Finally, we note that we restrict our attention to thin structures. This restriction is not required by the structural equations; indeed, the formulation described in

(3.3); (3.6)–(3.8) is valid for a variety of structures. The reason for the thin-structure restriction is due to the fact that the immersed-boundary method places fictitious fluid inside of bodies that produces unphysical contributions to the surface stress in (3.5). For rigid body FSI problems (*e.g.*, freely falling cylinders), the stress contribution from the fictitious fluid can be explicitly removed to obtain the correct stress [43], but this procedure is difficult to extend to deforming bodies. We therefore consider thin bodies, such as shells or membranes, where these unphysical contributions are negligible.

3.3 Numerical method

In this section, we discretize the equations of motion in space to arrive at the coupled semi-discrete equations of motion: the fluid equations are discretized using the 2D discrete streamfunction formulation of Colonius and Taira [15], and the structure equations are discretized using a finite element formulation. We then discretize in time and introduce an efficient iteration procedure for solving the resulting nonlinear algebraic equations.

Semi-discrete equations

As noted in chapter 2, the spatially discrete equations of motion for the fluid on a staggered uniform Cartesian grid are

$$\dot{u} + \mathcal{N}(u) = -Gp + Lu + H(\chi)f \tag{3.9}$$

$$Du = 0 \tag{3.10}$$

where the various operators are defined in chapter 2 (see also reference [79] for more details). One distinction from chapter 2, however, is that we write the explicit dependence of H on the unknown structural displacement χ.

Following Colonius and Taira [15], we avoid the incompressibility constraint by using a discrete curl operator that lies in the null space of the discrete divergence operator D. That is, $DC \equiv 0$, which implies that $C^T G = -(DC)^T \equiv 0$. The discrete curl operator engenders the use of a discrete streamfunction, s, that is related to the discrete velocity field by $u = Cs$. Using this and premultiplying (3.9) and (3.10) by C^T then gives the final form of the semi-discrete fluid equations that we consider:

$$C^T C\dot{s} + \mathcal{N}(Cs) = C^T LCs - C^T E^T(\chi)f \tag{3.11}$$

The equations for the structure are discretized in space using a finite element procedure: the body is broken up into isoparametric finite elements with an associated

set of compatible shape functions [6]. A variable $(\cdot)$ belonging to the surface may be expressed with these basis functions as

$$(\cdot)(\boldsymbol{\chi}) = \sum_{j=1}^{N_{node}} (\cdot)_j b_j(\boldsymbol{\chi}) \tag{3.12}$$

where $(\cdot)_j$ is the nodal value of $(\cdot)$ and b_j is the shape function corresponding to node j. Using this expansion of each variable in (3.3), we arrive at a system of ordinary differential equations in time by multiplying (3.3) by the various shape functions and integrating over the volume of the immersed body. Letting B be a matrix containing the various shape functions b_j, we write the spatially discretized form of (3.3) as

$$M\ddot{\chi} + R(\chi) = Q(g + W(\chi)f) \tag{3.13}$$

where

$$M = \frac{\rho_s}{\rho_f} \sum_{j=1}^{N_{el}} \int_{\Gamma_j^0} B^T B d\boldsymbol{\chi}^0 \tag{3.14}$$

$$R(\chi) = \frac{1}{\rho_f U_\infty^2} \sum_{j=1}^{N_{el}} \int_{\Gamma_j^0} B_E^T \sigma^K d\boldsymbol{\chi}^0 \tag{3.15}$$

$$Q = \sum_{j=1}^{N_{el}} \int_{\Gamma_j^0} B^T B d\boldsymbol{\chi}^0 = \frac{\rho_f}{\rho_s} M \tag{3.16}$$

In the above, Γ_j^0 denotes element j of Γ in its undeformed configuration, B_E is a matrix containing the derivatives of the shape functions with respect to the nodal positions, and σ^K contains nodal values of its continuous analog. Note that σ^K is arranged as a vector so that $R(\chi)$ is also a vector. The nonlinearity of $R(\chi)$ is due to the dependence of B_E and σ_K on χ.

Note the presence of $W(\chi) = \tilde{E}(\chi)H(\chi)$ in (3.13), which is the filtering operator described in chapter 2. The effectiveness of this operator in producing convergent surface stresses depends on the smeared delta function used, with more differentiable functions providing increasingly accurate approximations. Our experience is that the infinitely differentiable Gaussian function, δ_h^G, was not necessary for performing accurate FSI computations, as the time-stepping procedure and spatial operators associated with the structure equations of motion provide some regularization to the high-frequency surface-stress oscillations. At the same time, the use of δ_h^{cos} was found to introduce high frequency dynamics into the structure that spuriously alter the system behavior. In the present work, we use the delta function of Roma, Peskin,

and Berger [64], which we found to provide a good combination of computational efficiency and accuracy. Note also that Wf is a discretization of

$$\frac{\int_\Omega \int_\Gamma \mathbf{f}(\boldsymbol{\chi}(s',t))\delta_h(\mathbf{x}-\boldsymbol{\chi}(s',t))\delta_h(\mathbf{x}-\boldsymbol{\chi}(s,t))ds'd\mathbf{x}}{\int_\Gamma \delta_h(\mathbf{x}-\boldsymbol{\chi}(s',t))ds'} \tag{3.17}$$

so introducing W into (3.13) represents a first-order modification in the grid spacing h of the structural equations of motion.

Equation (3.13) and the corresponding definitions of M, R, and Q are valid for a variety of structural materials undergoing large deformations, displacements, and rotations. In this work we restrict our attention to flags, for which we employ a corotational formulation [18]. In this formulation, arbitrarily large displacements and rotations are accommodated by attaching a local coordinate frame to each flag element. The strains are assumed to be small in this frame, and the corresponding internal stresses $R(\chi)$ are well known (see, *e.g.*, reference [18]). Materials other than flags would require changes in the choice of elements, shape functions, and model for σ^K. However, these changes would not affect the structure of (3.13) or the ensuing time discretization procedure.

Using these discretizations of the fluid and structure equations, the discrete form of the constraint (3.4) is written in terms of the streamfunction as

$$E(\chi)Cs - \zeta = 0 \tag{3.18}$$

Defining $\zeta := \dot{\chi}$, the fully coupled FSI equations may be written as a first order system of differential-algebraic equations given by

$$C^TC\dot{s} = -\mathcal{N}(Cs) + C^TLCs - C^TE^T(\chi)f \tag{3.19}$$

$$M\dot{\zeta} = -R(\chi) + Q(g + W(\chi)f) \tag{3.20}$$

$$\dot{\chi} = \zeta \tag{3.21}$$

$$E(\chi)Cs - \zeta = 0 \tag{3.22}$$

Note that (3.9)–(3.10) and (3.13) are valid in both 2D and 3D; the restriction to 2D is due only to the discrete streamfunction formulation (3.11). We derive in section 3.5 an alternative method that treats the fluid using (3.9)–(3.10). This method has an analogous iteration procedure to the one proposed in the next section and is readily extendible to 3D.

Time discretization and efficient factorization procedure

We discretize (4.1) using an Adams-Bashforth scheme for the nonlinear term and a Crank-Nicholson method for the diffusive term. Equations (4.2)–(4.3) are discretized using an implicit Newmark scheme. The constraint equation (4.4) is evaluated at the current time step. That is, the method is strongly-coupled, which is necessary for the method to be stable for a wide range of mass ratios and in the presence of large body displacements [10, 12, 25]. We discretize the equations of motion in the aforementioned way to illustrate the iteration procedure on a commonly used scheme. However, the proposed iteration approach can readily be extended for a variety of time stepping schemes.

Discretizing (4.1)–(4.4) as described in the previous paragraph leads to a system of nonlinear algebraic equations given by

$$C^T A C s_{n+1} + C^T E_{n+1}^T f_{n+1} = r_n^f \tag{3.23}$$

$$\frac{4}{\Delta t^2} M \chi_{n+1} + (R(\chi_{n+1}) - Q W_{n+1} f_{n+1}) = r_n^\zeta \tag{3.24}$$

$$\frac{2}{\Delta t} \chi_{n+1} - \zeta_{n+1} = r_n^\chi \tag{3.25}$$

$$E_{n+1} C s_{n+1} - \zeta_{n+1} = 0 \tag{3.26}$$

where $A = \frac{1}{\Delta t} I - \frac{1}{2} L$, $r_n^f = (\frac{1}{\Delta t} C^T C + \frac{1}{2} C^T L C) s_n + \frac{3}{2} C^T \mathcal{N}(C s_n) - \frac{1}{2} C^T \mathcal{N}(C s_{n-1})$, $r_n^\zeta = M(\frac{4}{\Delta t^2} \chi_n + \frac{4}{\Delta t} \zeta_n + \dot{\zeta}_n) + Qg$, and $r_n^\chi = \zeta_n + \frac{2}{\Delta t} \chi_n$. Note that the operators E, E^T, and W are given subscripts to indicate their dependence on χ.

We now describe an iteration procedure for using a guess for the solution at iteration (k) to compute a new guess at iteration $(k+1)$ (We use the solution at time step n as the guess for $(k) = 0$). To do this, we write $\chi_{n+1}^{(k+1)} = \chi_{n+1}^{(k)} + \Delta\chi$, $\zeta_{n+1}^{(k+1)} = \zeta_{n+1}^{(k)} + \Delta\zeta$, where the increments $\Delta\chi$, $\Delta\zeta$ are assumed to be small. Substituting this decomposition into (3.23)–(3.26) and retaining first order terms in the increments

and Δt gives the linear system[2]

$$\begin{bmatrix} C^T AC & 0 & 0 & C^T E_{n+1}^{(k)T} \\ 0 & 0 & \frac{4}{\Delta t^2} M + K^{(k)} & -QW_{n+1}^{(k)} \\ 0 & -I & \frac{2}{\Delta t} I & 0 \\ E_{n+1}^{(k)} C & -I & 0 & 0 \end{bmatrix} \begin{bmatrix} s_{n+1} \\ \Delta\zeta \\ \Delta\chi \\ f_{n+1}^{(k+1)} \end{bmatrix} = \begin{bmatrix} r_n^f + O(\Delta t) \\ r_n^\zeta - \frac{4}{\Delta t^2} M\chi_{n+1}^{(k)} - R(\chi_{n+1}^{(k)}) + O(\Delta t) \\ r_n^\chi - \frac{2}{\Delta t}\chi_{n+1}^{(k)} + \zeta_{n+1}^{(k)} \\ \zeta_{n+1}^{(k)} + O(\Delta t) \end{bmatrix} := \begin{bmatrix} r_n^f \\ r^{\zeta\,(k)} \\ r^{\chi\,(k)} \\ r^{c\,(k)} \end{bmatrix} \tag{3.27}$$

where $K^{(k)} = dR/d\chi|_{\chi=\chi_{n+1}^{(k)}}$. For flags this stiffness matrix has well known analytical expressions [6, 18].

The linear system (3.27) may be factored using a block-LU decomposition. Defining $\hat{K}^{(k)} := \frac{4}{\Delta t^2} M + K^{(k)}$ and $B_{n+1}^{(k)} := E_{n+1}^{(k)} C(C^T AC)^{-1} C^T E_{n+1}^{(k)T}$, the factored equations are

$$s^* = (C^T AC)^{-1} r_n^f \tag{3.28}$$

$$\begin{bmatrix} B_{n+1}^{(k)} & I \\ -\frac{2}{\Delta t} QW_{n+1}^{(k)} & \hat{K}^{(k)} \end{bmatrix} \begin{bmatrix} f_{n+1}^{(k+1)} \\ \Delta\zeta \end{bmatrix} = \begin{bmatrix} E_{n+1}^{(k)} Cs^* - r^{c\,(k)} \\ \frac{2}{\Delta t} r^{\zeta\,(k)} - r^{\chi\,(k)} \end{bmatrix} \tag{3.29}$$

$$\Delta\chi = \frac{\Delta t}{2}(\Delta\zeta + r^{\chi\,(k)}) \tag{3.30}$$

$$s_{n+1} = s^* - (C^T AC)^{-1} C^T E_{n+1}^T f_{n+1} \tag{3.31}$$

The LU-factorized equations (3.28)–(3.31) are analogous to the classical fractional-step procedure used for the Navier-Stokes equations. In fact, Perot [61] showed that the fractional-step procedure for the Navier-Stokes equations can be derived by a block-LU factorization of the associated semi-discrete system. Taira and Colonius [79] used a block-LU factorization to derive an analogous fractional step procedure for an immersed boundary method applied to rigid bodies undergoing prescribed kinematics, and Lācis, Taira, and Bagheri [43] extended this analysis to allow for rigid-body flow-structure interaction. Our method applies this block-LU fractional-step philosophy to FSI problems involving deforming bodies.

[2]Derivative terms that arise in the expansion of $E_{n+1}^{(k+1)}$, $E_{n+1}^{(k+1)T}$, and $W_{n+1}^{(k+1)}$ may be neglected to within $O(\Delta t)$. For example, the fourth block equation of (3.27) including this extra term is $E_{n+1}^{(k)} Cs_{n+1} + (DE_{n+1}^{(k)}\Delta\chi)Cs_{n+1} - \Delta\zeta = \zeta_{n+1}^{(k)}$. The DE term is of order $O(\Delta t)$ compared with the $\Delta\zeta$ term, since by the third block equation $\Delta\chi = O(\Delta\zeta\Delta t)$.

The fractional-step procedure (3.28)–(3.31) has a physical interpretation: first, a trial streamfunction that does not account for the updated body position and velocity boundary conditions is computed through (3.28). Then the surface stress and the associated body position and velocity are computed through iteration in (3.29)–(3.30). Finally, in (3.31) the updated surface stress is used to remove the part of the streamfunction that does not satisfy the updated boundary conditions.

Note that (3.28) does not depend on information at time step $n+1$, and (3.29)–(3.30) do not require knowledge of s_{n+1}. Thus, (3.28) can be solved once and for all at the beginning of each time step, and s_{n+1} only needs to be computed once, after (3.29)–(3.30) have been iterated to convergence. This has the benefit that all iterations are restricted to (3.29)–(3.30), which have dimensions on the order of the number of body points, rather than the total number of points in the flow domain. We do not write a superscript on s_{n+1} since it does not need to be iterated on. Wang and Eldredge [88] also restricted iterations to small dimensional subsystems like (3.29)–(3.30). In their case, the structure equations were replaced by the rigid body equations of motion, and a block Gauss-Seidel procedure with added mass relaxation was used to solve their analogous nonlinear system.

A Poisson-like problem $(C^T AC)^{-1}$ must be solved in (3.28), (3.31), and in each matrix-vector multiply with $B_{n+1}^{(k)}$. Solving the Poisson-like problem may be done efficiently using fast Fourier transforms, but this requires a number of operations that scales with the number of points on the flow domain. Thus, the computation and storage of $(\hat{K}^{(k)})^{-1}$ may be small compared with solving the Poisson-like problem. In this case one may analytically perform a block-Gaussian elimination of (3.29) to get

$$\begin{aligned}\left(B_{n+1}^{(k)} + \frac{2}{\Delta t}(\hat{K}^{(k)})^{-1} Q W_{n+1}^{(k)}\right) f_{n+1}^{(k+1)} = E_{n+1}^{(k)} C s^* - \\ r^{c\,(k)} - \frac{2}{\Delta t}(\hat{K}^{(k)})^{-1} r^{\zeta\,(k)} + r^{\chi\,(k)}\end{aligned} \tag{3.32}$$

$$\Delta\zeta = \frac{2}{\Delta t}(\hat{K}^{(k)})^{-1}(r^{\zeta\,(k)} + Q W_{n+1}^{(k)} f_{n+1}^{(k)}) - r^{\chi\,(k)} \tag{3.33}$$

One may therefore equivalently solve (3.28)–(3.31) with (3.29) replaced by (3.32)–(3.33), which has the benefit of avoiding the inhomogeneous block structure of (3.29). We use this formulation for the results shown below, as we found it to be more efficient for the test problems considered. We solve (3.32) using the BiCGSTAB method, which typically requires 2–8 iterations to converge using $f_{n+1}^{(k)}$ as the initial guess. Moreover, the number of iterations required by BiCGSTAB

often decreases as k increases, since $f_{n+1}^{(k)}$ becomes an increasingly good guess for $f_{n+1}^{(k+1)}$.

It is also worth noting that the updates for $\chi_{n+1}^{(k)}$, $\zeta_{n+1}^{(k)}$, and $f_{n+1}^{(k)}$ do not depend on a heuristic relaxation parameter, as is often required when applying the block Gauss-Seidel iterative procedure to FSI solvers. Moreover, the proposed iteration procedure has required a small number of iterations to converge for all problems we have considered so far.

3.4 Verification on flapping flag problems

We verify our method for several test problems of 2D flow past thin deforming flags. The dynamics of this system are governed by the Reynolds number, dimensionless mass ratio, dimensionless bending stiffness, and Froude number. These are given, respectively, as

$$Re = \frac{U_\infty L}{\nu},\ M_\rho = \frac{\rho_s h}{\rho_f L},\ K_B = \frac{EI}{\rho_f U_\infty^2 L^3},\ Fr = \frac{U_\infty}{\sqrt{gL}} \tag{3.34}$$

where h is the thickness of the flag, EI is the bending stiffness of the flag, ν is the kinematic viscosity of the fluid, and g is the gravitational constant.

We consider problems with the flag pinned at the leading edge (conventional configuration) and with the flag clamped at the trailing edge (inverted configuration). Schematics of the different problem setups are shown in figure 3.1.

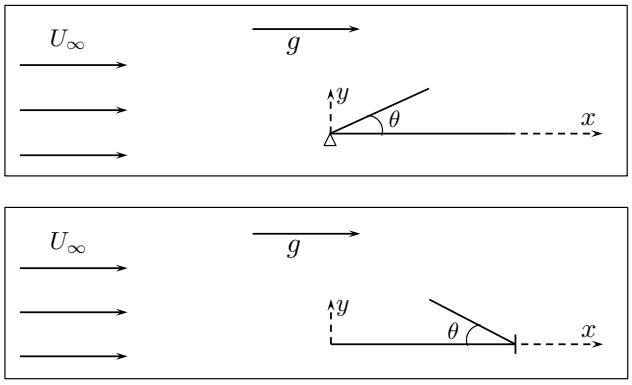

Figure 3.1: Flow moves from left to right past a flag in the conventional configuration (top) or the inverted configuration (bottom).

Each configuration presents different challenges: flags in the conventional configuration are typically associated with smaller mass ratios, whereas those in the inverted configuration often undergo larger motions and have greater dimensionless bending stiffnesses.

The flow equations are solved using a multidomain approach: the finest grid surrounds the body and grids of increasing coarseness are used as distance from the body increases (see reference [15] for details). The immersed-boundary spacing must be large enough with respect to the flow grid to avoid ill-conditioning of the matrix $B_{n+1}^{(k)}$ [3], but sufficiently small to keep the body from being porous. We found that setting the immersed-boundary spacing to be twice that of the flow grid on the finest sub-domain gave the appropriate balance (Kallemov et al. [38] also found this ratio to be preferable). We used a convergence criteria of $||\Delta\chi||_\infty / ||\chi_{n+1}^{(k+1)}||_\infty \leq 1 \times 10^{-7}$ when iterating between (3.30), (3.32), and (3.33).

Flow past a flag in the conventional configuration

We first consider flow past a deforming flag in the conventional configuration with $Re = 1000$, $M_\rho = 0.075$, $K_B = 0.0001$, and $Fr = 0$ (*i.e.*, no gravitational body force). This choice of parameters leads to limit cycle flapping, which we triggered in our simulations by initializing the flag at $\theta = 1^\circ$ (see figure 3.1 for the definition of θ). We show the transverse tip displacement and lift coefficient in figure 3.2. After an initial transient, the trailing edge of the flag has oscillatory transverse displacement of fixed amplitude and frequency. The lift and tip displacement share the same frequency but are out of phase. As the flag nears its peak amplitude, the lift force opposes it enough to overcome the flag's inertia, which initiates flag motion in the other direction. This interplay of fluid and flag forces modulates and sustains the limit cycle flapping behavior seen for this set of parameters. Our computed amplitude and frequency of the flag tip displacement in the limit cycle regime agree well with published values for these quantities (see table 3.1).

The finest domain for this simulation was of size $[-0.2, 1.8] \times [-0.3, 0.3]$, and the entire flow domain size was $[-15.20, 16.80] \times [-4.78, 4.78]$. The grid spacing on the finest subdomain was $h = 0.0025$, and the time step was $\Delta t = 0.0006$. Using a grid spacing of $h = 0.003$ changed our results in table 3.1 by less than one percent. There were a total of 960,000 points in the flow domain, and it took 30.83 hours to run this simulation on a single CPU core. Five iterations of (3.30), (3.32), and (3.33) were required for the first time step, and a maximum of three iterations were required for all remaining time steps.

[3] The ill-conditioning associated with small immersed-boundary spacing arises from the fact that as the number of immersed-boundary points increases relative to the grid spacing, more surface quantities are being distributed to a given point on the flow grid, and redistributing that information back onto the surface becomes increasingly difficult.

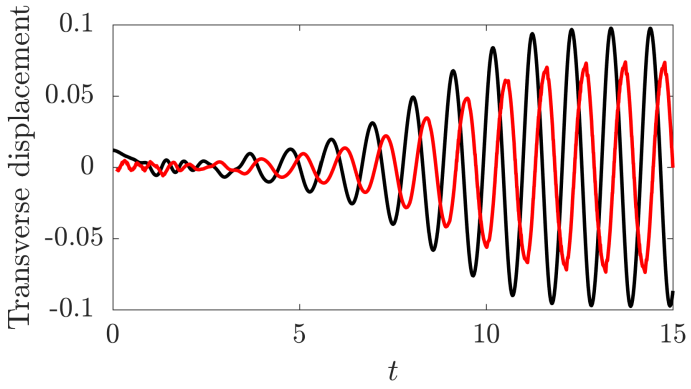

Figure 3.2: Transverse displacement of the flag's trailing edge (black) and coefficient of lift (gray) for $Re = 1000$, $K_B = 0.0001$, and $Fr = 0$.

	Amplitude	Frequency (St)
Connell and Yue [17]	±0.096	0.93
Gurugubelli and Jaiman [32]	±0.098	0.95
Present	±0.097	0.94

Table 3.1: Amplitude and frequency associated with the transverse displacement of the flag's trailing edge; obtained for $Re = 1000$, $M_\rho = 0.075$, $K_B = 0.0001$, and $Fr = 0$.

Limit cycle flapping also occurs for $Re = 200$, $M_\rho = 1.5$, $K_B = 0.0015$, and $Fr = 1.4$. We show in table 2 the associated amplitude and frequency of the transverse trailing edge displacement. For comparison with the literature, we initialized the flag at $\theta = 18°$. Our finest sub-domain for this problem was of size $[-0.2, 1.8] \times [-0.9, 0.9]$, and the total domain size was $[-15.20, 16.80] \times [-7.95, 7.95]$. The grid spacing on the finest domain was $h = 0.00625$, and the time step was $\Delta t = 0.0001$. Using $h = 0.005$ changed our reported results from table 3.2 by less than one percent. There were a total of 460,800 points in the flow domain, and it took 10.42 hours to run this simulation on a single CPU core. Three iterations of (3.30), (3.32), and (3.33) were required for the first time step, and a maximum of two iterations were required for all remaining time steps.

Figure 3.3 gives a time history of the trailing edge transverse displacement for the parameters corresponding to table 3.2 (results from references [35, 47] are included for comparison). To emphasize the robustness of the method for a range of mass ratios, figure 3.3 also shows the trailing edge displacement for $M_\rho = 0.0001$ and $M_\rho = 100$. To our knowledge, the $M_\rho = 0.0001$ and $M_\rho = 100$ cases have not been simulated before. Moreover, we were not able to simulate the $M_\rho = 0.0001$

	Amplitude	Frequency (St)
Huang, Shin, and Sung [35]	±0.35	0.30
Wang and Eldredge [88]	±0.35	0.31
Lee and Choi [47]	±0.38	0.31
Present	±0.38	0.32

Table 3.2: Amplitude and frequency associated with the transverse displacement of the flag's trailing edge; obtained for $Re = 200$, $M_\rho = 1.5$, $K_B = 0.0015$, and $Fr = 1.4$.

case when solving (3.23)–(3.26) with the Gauss-Seidel method, even when using extensive relaxation. Using (3.30), (3.32), and (3.33), a maximum of three iterations per time step were required after the first twenty time steps. During the first twenty time steps, up to fifteen iterations were required due to the impact of the impulsive start on a flag with such small inertia.

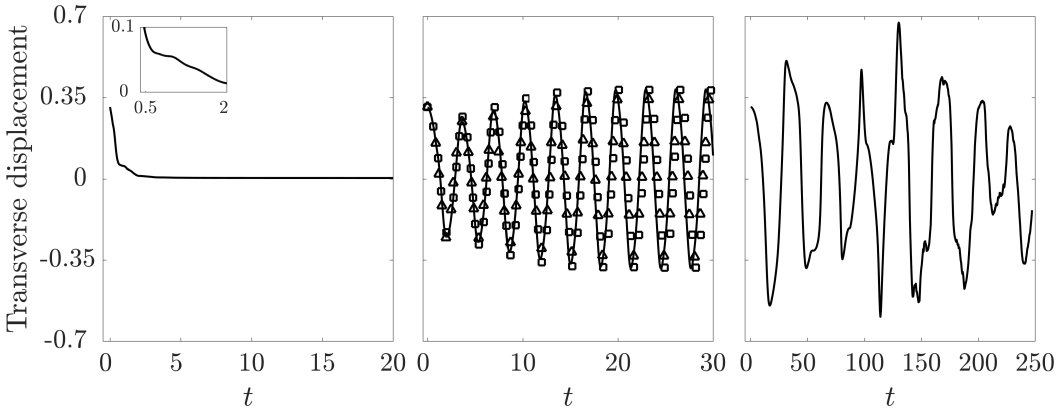

Figure 3.3: Transverse displacement of the flag's trailing edge for $Re = 200$, $K_B = 0.0015$, and $Fr = 1.4$. Left panel: $M_\rho = 0.0001$, middle panel: $M_\rho = 1.5$, right panel: $M_\rho = 100$. Present: —, Lee and Choi [47]: □, Huang, Shin, and Sung [35]: △. The insert on the left panel is a zoom-in of the $M_\rho = 0.0001$ case for $t \in [0.5, 2]$. Note the different horizontal axis values on each panels.

In figure 3.4, we show vorticity contours at different time instances for $M_\rho = 0.0001$, $M_\rho = 1.5$, and $M_\rho = 100$. When $M_\rho = 0.0001$, the impulsive start pushes the flag down quickly towards the $\theta = 0°$ position. At $t \approx 0.5$, the vortical structure created during the impulsive start reaches the trailing edge of the flag. Due to the flag's small inertia, this substantially affects the trailing edge displacement (see insert in figure 3.3). The vortical structure then advects away from the body, and the fluid wake becomes symmetric as the flag fully reaches its $\theta = 0°$ position.

This symmetric wake is a well known feature of flow past thin rigid bodies at low Reynolds numbers, and the small inertia of the flag does not allow for any minor flag deformations to break the flow symmetry. Thus, the flag stays in this neutral position for all remaining time. When $M_\rho = 1.5$, the limit cycle flapping of the flag is associated with a periodic vortex street [35, 47, 88]. As the flag becomes increasingly massive, the flapping amplitude increases. This is associated with a thicker, more irregular wake profile and more chaotic flapping behavior. Figure 3.3 shows that the $M_\rho = 100$ case does not enter into limit cycle flapping after 250 convective time units and several periods of flapping. The destabilizing nature of increasing the mass ratio was also noted by Connell and Yue [17].

Flow past a flag in the inverted configuration

An inverted flag initially placed at $\theta = 0^\circ$ can enter a wide range of possible dynamical regimes. Three of these are the undeformed equilibrium (UE), deformed equilibrium (DE), or small-deflection deformed flapping (SF) [32] (see figure 3.5 for an illustration). In table 3.3, we summarize the regimes we obtained by varying K_B for $Re = 200$, $M_\rho = 0.1$, and $Fr = 0$. Our finest sub-domain for this problem was of size $[-0.2, 1.8]\times[-0.5, 0.5]$, and the total domain size was $[-15.20, 16.80]\times[-16, 16]$. The grid spacing on the finest domain was $h = 0.005$, and the time step was $\Delta t = 0.001$. Using $h = 0.004$ change our reported results by less than one percent. There were a total of 400,000 points in the flow domain, and it took 5.56 hours to run one simulation on a single CPU core. Three iterations of (3.30), (3.32), and (3.33) were required for the first time step, and a maximum of two iterations were required for all remaining time steps. The table also shows the regimes computed by Gurugubelli and Jaiman [32] for the same parameter ranges.

	K_B									
	0.42	0.43	0.44	0.45	0.46	0.47	0.48	0.49	0.50	0.51
[32]	SF	SF	SF	SF	DE	DE	DE	DE	DE	UE
Present	SF	SF	SF	DE	DE	DE	DE	DE	DE	UE

Table 3.3: Flapping regimes obtained for different K_B values. SF = small-deflection deformed flapping, DE = deformed equilibrium, UE = undeformed equilibrium. The other parameters were $Re = 200$, $M_\rho = 0.1$, and $Fr = 0$.

We next consider the case when $Re = 1000$, $M_\rho = 0.1$, $K_B = 0.4$, and $Fr = 0$. For this set of parameters, the flag enters large amplitude limit cycle flapping. Table 3.4 shows the amplitude and frequency of the leading edge transverse displacement computed in our work and in reference [32]. Our finest sub-domain for this problem

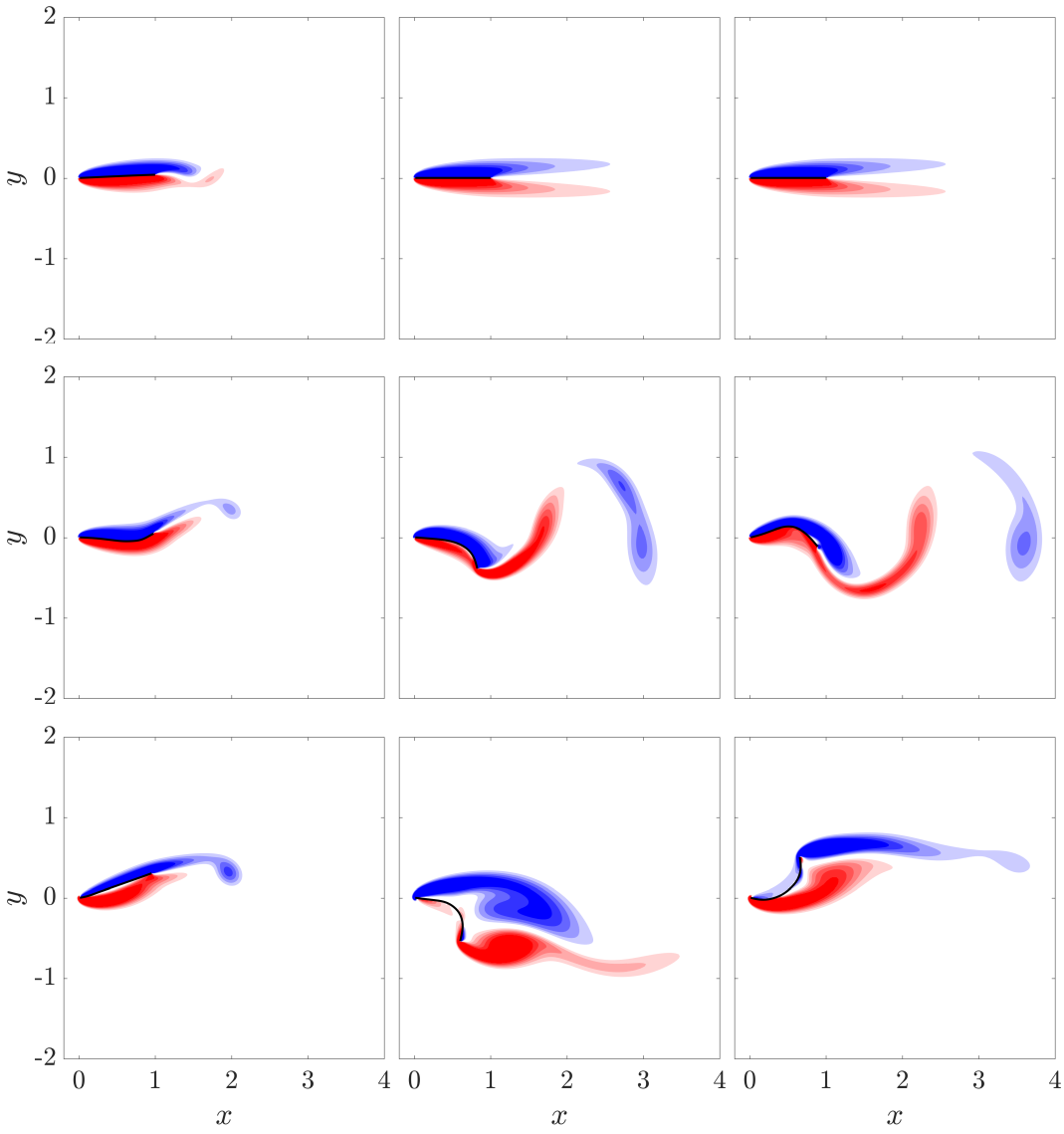

Figure 3.4: Vorticity contours of flow past a deforming flag for $M_\rho = 0.0001$ (top row), $M_\rho = 1.5$ (middle row), and $M_\rho = 100$ (bottom row). Left column: $t = 1.2$; middle column: $t = 18$; right column: $t = 31.2$. Contours are in 15 evenly spaced increments from -5 to 5. The other parameters were $Re = 200$, $M_\rho = 1.5$, and $Fr = 1.4$.

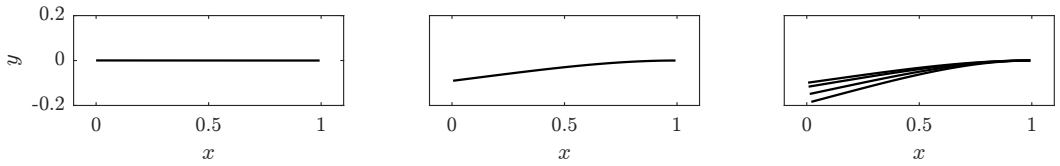

Figure 3.5: Snapshots of the flag at various times for the unstable equilibrium (left), deformed equilibrium (middle), and small-deflection deformed flapping (right) regimes. Only one curve is visible for the unstable equilibrium and deformed equilibrium regime, since the flag does not deflect about these equilibrium positions.

was of size $[-0.2, 1.8] \times [-1, 1]$, and the total domain size was $[-15.20, 16.80] \times [-14.35, 14.35]$. The grid spacing on the finest domain was $h = 0.0033$, and the time step was $\Delta t = 0.0003$. Using $h = 0.0025$ did not change our reported results. There were a total of 1,800,000 points on the flow domain, and it took 106 hours to run the simulation on a single CPU core. Three iterations of (3.30), (3.32), and (3.33) were required for the first time step, and a maximum of two iterations were required for all remaining time steps.

	Amplitude	Frequency (St)
Gurugubelli and Jaiman [32]	±0.83	0.204
Present	±0.82	0.198

Table 3.4: Amplitude and frequency associated with the transverse displacement of the flag's leading edge; obtained for $Re = 1000$, $M_\rho = 0.5$, $K_B = 0.4$, and $Fr = 0$.

Figure 3.6 shows vorticity contours at four different times during a flapping cycle. The figure shows features consistent with what was observed by Gurugubelli and Jaiman [32]. As the flag reaches its negative peak displacement, a positive leading edge vortex forms (leftmost figure). The flag then moves back towards the centerline and the leading edge vortex detaches and advects downstream (second from leftmost figure). As the flag continues to swing towards its positive peak displacement, a negative trailing edge vortex forms and advects downstream to form a vortex pair with the leading edge vortex shed earlier (second from rightmost figure). At the same time, a new negative leading edge vortex forms as the flag reaches its peak displacement and detaches once the flag moves back towards the centerline (rightmost figure). The result of this upward-downward flag motion is limit cycle flapping that repeats indefinitely.

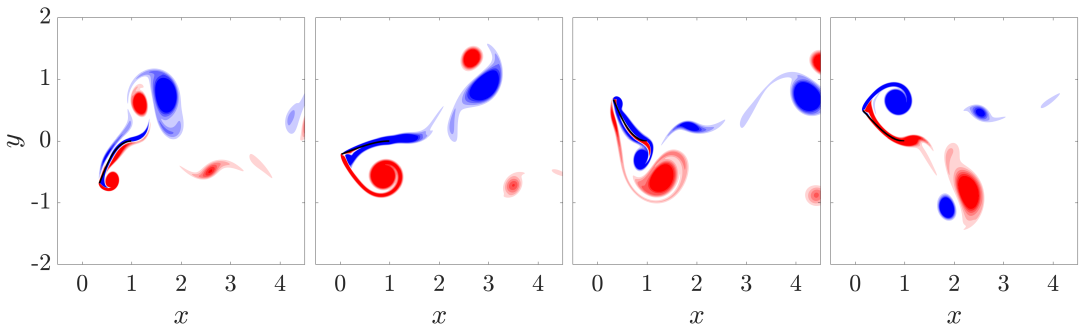

Figure 3.6: Vorticity contours during a flapping cycle for $Re = 1000$, $M_\rho = 0.5$, $K_B = 0.4$, $Fr = 0$. Contours are in 15 evenly spaced increments from -5 to 5.

3.5 An efficient iteration procedure in primitive variables

The above method was derived in a discrete vorticity-streamfunction formulation, which is perhaps best suited for two-dimensional problems. We derive here an analogous formulation using primitive variables for the fluid that can be applied in 2D or 3D. In this primitive variable representation, the differential-algebraic semidiscrete FSI system is

$$\dot{u} + \mathcal{N}(u) = -Gp + Lu - E^T(\chi) f \tag{3.35}$$

$$M\dot{\zeta} = -R(\chi) + Q(g + W(\chi) f) \tag{3.36}$$

$$\dot{\chi} = \zeta \tag{3.37}$$

$$Du = 0 \tag{3.38}$$

$$E(\chi)u - \zeta = 0 \tag{3.39}$$

Using the same time discretization schemes as in section 3 and introducing the decomposition $\chi_{n+1}^{(k+1)} = \chi_{n+1}^{(k)} + \Delta\chi$, $\zeta_{n+1}^{(k+1)} = \zeta_{n+1}^{(k)} + \Delta\zeta$, we have the following system to within first order in the increments and Δt:

$$\begin{bmatrix} A & G & 0 & 0 & E_{n+1}^{(k)T} \\ G^T & 0 & 0 & 0 & 0 \\ 0 & 0 & 0 & \hat{K}^{(k)} & -QW_{n+1}^{(k)} \\ 0 & 0 & -I & \frac{2}{\Delta t} I & 0 \\ E_{n+1}^{(k)} & 0 & -I & 0 & 0 \end{bmatrix} \begin{bmatrix} u \\ p_{n+1} \\ \Delta\zeta \\ \Delta\chi \\ f_{n+1}^{(k+1)} \end{bmatrix} = \begin{bmatrix} \tilde{r}_n^f \\ \tilde{r}_n^p \\ r^{\zeta\,(k)} \\ r^{\chi\,(k)} \\ r^{c\,(k)} \end{bmatrix} \tag{3.40}$$

where the right hand side terms are known and analogous to those in section 3.

Performing a block-LU decomposition of (3.40) gives the sequence of equations

$$u^* = A^{-1}\tilde{r}_n^f - A^{-1}G(G^TA^{-1}G)^{-1}(G^TA^{-1}\tilde{r}_n^f - \tilde{r}^p) \tag{3.41}$$

$$p^* = (G^TA^{-1}G)^{-1}(G^TA^{-1}\tilde{r}_n^f - \tilde{r}_n^p) \tag{3.42}$$

$$\begin{bmatrix} \tilde{B}_{n+1}^{(k)} & I \\ -\frac{2}{\Delta t}QW_{n+1}^{(k)} & \hat{K}^{(k)} \end{bmatrix} \begin{bmatrix} f_{n+1}^{(k+1)} \\ \Delta\zeta \end{bmatrix} = \begin{bmatrix} E_{n+1}^{(k)}u^* - r^{c\,(k)} \\ \frac{2}{\Delta t}r^{\zeta\,(k)} + r^{\chi\,(k)} \end{bmatrix} \tag{3.43}$$

$$\Delta\chi = \frac{2}{\Delta t}(\Delta\zeta + r^{\chi\,(k)}) \tag{3.44}$$

$$p_{n+1} = p^* - (G^TAG)^{-1}G^TA^{-1}E_{n+1}^{(k)\,T}f_{n+1} \tag{3.45}$$

$$u_{n+1} = u^* - A^{-1}(I - G(G^TA^{-1}G)^{-1}G^TA^{-1})E_{n+1}^{(k)\,T}f_{n+1} \tag{3.46}$$

where $\tilde{B}_{n+1}^{(k)} = E_{n+1}^{(k)}A^{-1}(I - G(G^TA^{-1}G)^{-1}G^TA^{-1})E_{n+1}^{(k)\,T}$.

As in section 3, all iterations are restricted to (3.43)–(3.44), which have dimensions on the order of the number of body points; (3.41)–(3.42) may be computed once and for all at the start of a time step, and (3.45)–(3.46) need only be solved after all iterations are completed to convergence.

Again, when $(\hat{K}^{(k)})^{-1}$ can be computed and stored, the system (3.43) may be reformulated as the sequence of equations given by

$$\left(\tilde{B}_{n+1}^{(k)} + \frac{2}{\Delta t}(\hat{K}^{(k)})^{-1}QW_{n+1}^{(k)}\right) f_{n+1}^{(k+1)} = E_{n+1}^{(k)}u^* - r^{c\,(k)} - \frac{2}{\Delta t}(\hat{K}^{(k)})^{-1}r^{\zeta\,(k)} + r^{\chi\,(k)} \tag{3.47}$$

$$\Delta U = \frac{2}{\Delta t}(\hat{K}^{(k)})^{-1}(r^{\zeta\,(k)} + QW_{n+1}^{(k)}f_{n+1}^{(k)}) - r^{\chi\,(k)} \tag{3.48}$$

A similar block-LU based immersed boundary method was developed for bodies undergoing prescribed kinematics [51, 79]. The method we propose in (3.41)–(3.46) is different from these in the nonlinear iterations introduced in (3.43)–(3.44). Since these iterations are restricted to small dimensional subsystems, we do not believe they will drastically affect the effectiveness of the method.

3.6 Conclusions

We presented an immersed-boundary method for fully coupled flow-structure interaction problems involving thin deforming surfaces. The method is strongly-coupled, and is therefore stable for wide ranges of structure-to-fluid mass ratios and large body motions. As with many strongly-coupled methods, our method requires the solution

of a nonlinear system of equations at each time step. This system is solved by iteration, using a linearization of the nonlinearly coupled equations and a block-LU factorization of the linearized system to reduce iterations to small-dimensional subsystems of equations. The iteration process does not involve heuristic relaxation parameters. We derived the method for general deforming surfaces, and verified it for 2D flow past deforming flags. The test problems involved a wide range of mass ratios and large body motions, and the method required a small number of iterations to converge for all cases considered. It is straightforward to extend the method to fully coupled problems involving rigid bodies.

Chapter 4

GLOBAL STABILITY ANALYSIS OF FLUID-STRUCTURE INTERACTION[1]

4.1 Introduction

Global stability analysis has been used to elucidate important instability-driving mechanisms in a variety of fluid flows without immersed bodies or with rigid bodies undergoing prescribed kinematics, such as bluff body flows [60], jet flows [4], and boundary layers [22]. In the context of FSI systems, this technique has been applied to the problem of an elastically mounted cylinder allowed to vibrate in the transverse direction [58], but, to our knowledge, has not been extended to problems involving deforming bodies.

We present here a global stability solver for general thin deforming bodies that may be used in concert with the nonlinear solver described in chapter 3. We validate our global stability solver using results from the literature on conventional flag flapping, and show in particular that a global mode analysis of conventional flags accurately predicts the onset of flutter and the associated flapping frequency once flapping ensues.

We note that previous stability analyses have been performed on conventional flag flapping to accurately predict the onset of flapping and the associated flapping frequencies [2, 17]. These studies focused on the governing equations of the flag with the effect of the fluid modeled as a source term using either inviscid [2] or laminar boundary layer [17] theory. Thus, the associated modes provided the least damped flag shapes, but did not reveal the corresponding fluid structures that drive the system to instability. Our present analysis is based on a linearization of the fully-coupled equations of motion, and therefore identifies both important flag shapes and fluid structures.

4.2 Numerical method

We derive the linearized equations of motion in this section and describe the algorithm for computing global modes of the fully-coupled FSI system. Note that an

[1] This chapter is based on the publication Goza and Colonius [27], for which my contributions were devising and implementing the numerical method, running all simulations, and being the primary author of the article.

equilibrium (steady-state) solution about which to linearize the system is required, and we define our algorithm for computing this equilibrium at the end of this section.

Linearized equations and global stability solver

The spatially discrete, temporally continuous equations of the nonlinear fully-coupled flow-structure system may be written as (see chapter 3 for more details)

$$C^T C\dot{s} = -C^T \mathcal{N}(s) + \frac{1}{Re} C^T L C s - C^T E^T(\chi) f \tag{4.1}$$

$$M\dot{\zeta} = -R(\chi) + Q(g + W(\chi) f) \tag{4.2}$$

$$\dot{\chi} = \zeta \tag{4.3}$$

$$0 = E(\chi) C s - \zeta \tag{4.4}$$

For ease of notation in developing the linearized equations, we define the state vector $y = [s, \zeta, \chi, f]^T$ and let $r(y)$ be the right hand side of (4.1)–(4.4). We write the state y as $y = y_b + y_p$, where $y_b = [s_b, \zeta_b, \chi_b, f_b]^T$ is a base state and $y_p = [s_p, \zeta_p, \chi_p, f_p]^T$ is a perturbation. Plugging this expression for y into (4.1)–(4.4), Taylor expanding about y_b, and retaining only first order terms in the perturbation variables gives the linearized equations:

$$B\dot{y}_p = A(y_b) y_p \tag{4.5}$$

where

$$B = \begin{bmatrix} C^T C & & & \\ & M & & \\ & & I & \\ & & & 0 \end{bmatrix}, \; A(y_b) = \begin{bmatrix} J^{ss} & 0 & -J^{\chi s} & -C^T E^T \\ 0 & 0 & -K + J^{\chi\chi} & QW \\ 0 & I & 0 & 0 \\ EC & -I & J^{\chi c} & 0 \end{bmatrix}_{y=y_b} \tag{4.6}$$

and the remaining sub-blocks of the Jacobian matrix A are given in index notation as

$$(J^{ss})_{ik} = -(C^T C)^2_{ik} - C^T_{ij} \frac{\partial \mathcal{N}_j}{\partial s_k} \tag{4.7}$$

$$(J^{\chi s})_{ik} = C^T_{ij} \frac{\partial E^T_{jl}}{\partial \chi_k} (f_b)_l \tag{4.8}$$

$$(J^{\chi\chi})_{ik} = Q_{ij} \frac{\partial W_{jl}}{\partial \chi_k} (f_b)_l \tag{4.9}$$

$$(J^{\chi c})_{ik} = \frac{\partial E_{ij}}{\partial \chi_k} C_{jl} (s_b)_l \tag{4.10}$$

Note that we used $B\dot{y}_b = r(y_b)$ in arriving at the linearized equations (4.5).

Global modes are eigenvectors v of the generalized eigenvalue problem $Av = \lambda Bv$, where λ is the corresponding eigenvalue. We build and store A and B sparsely and solve the generalized eigenvalue problem using an implicitly restarted Arnoldi algorithm (see Lehoucq, Sorensen, and Yang [48] for more details).

In the results below, 1×10^{-10} was used as the tolerance for convergence of the computed eigenvalues and eigenvectors. Global eigenfunctions are unique to a scalar multiple, and were scaled to unit norm, $||y||_2 = 1$.

Equilibrium computations

Undeformed and deformed equilibria are steady state solutions to the fully-coupled equations (4.1)-(4.4) with all time derivate terms set to zero; *i.e.*, these equilibria satisfy $0 = r(y)$, where $y = [s, \zeta, \chi, f]^T$ is the state vector and $r(y)$ is the right hand side of (4.1)-(4.4). This is a nonlinear algebraic system of equations that we solve using a Newton-Raphson method. With this method, the k^{th} guess for the base state, $y^{(k)}$, is updated as $y^{(k+1)} = y^{(k)} + \Delta y$, where

$$\Delta y = -(A(y^{(k)}))^{-1} r(y^{(k)}) \tag{4.11}$$

Note that the Jacobian matrix A in (4.11) is the same matrix as in (4.6) evaluated at $y = y^{(k)}$.

The guess for the state y is updated until the residual at the current guess is less than a desired threshold (*i.e.*, until $||r(y^{(k)})||_2 / ||y^{(k)}||_2 < \epsilon$). In the results shown below we used $\epsilon = 1 \times 10^{-6}$.

4.3 Validation on conventional flag flapping

We use known results about the onset of flapping of conventional flags to validate our global stability solver. We also investigate the structure of the global modes for different parameters along the flutter boundary to identify how instability-driving mechanisms are affected by changes to these parameters.

We do not consider the effect of gravity in these results (*i.e.*, $Fr = 0$). As mentioned in chapter 3, the driving dimensionless parameters are the Reynolds number and mass and stiffness ratios, defined as

$$Re = \frac{U_\infty L}{\nu}, \; M_\rho = \frac{\rho_s h}{\rho_f L}, \; K_B = \frac{EI}{\rho_f U_\infty^2 L^3} \tag{4.12}$$

Simulation Grid

The flow equations are solved using a multidomain approach: the finest grid surrounds the body and grids of increasing coarseness are used as distance from the body increases (see reference [15] for details). For all cases, the immersed boundary spacing is set to be twice that of the flow grid spacing on the finest sub-domain. The domain size of the finest sub-domain was $[-0.2, 1.8] \times [-0.6, 0.6]$ and the total domain size was $[-31.04, 32.04] \times [-19.04, 19.04]$. The grid spacing on the finest domain was $h = 2/400 \approx 0.005$. To determine the suitability of these simulation parameters, a grid convergence study was performed for $M_\rho = 0.1, K_B = 0.00069$ – decreasing the grid spacing by 30% and increasing the total domain size to $[-40.1, 41.1] \times [-27.08, 27.08]$ caused a change in leading eigenvalue of less than 2%.

Flapping Stability Boundary

Akcabay and Young [1] plotted a flutter map as a function of M_ρ and K_B using simulation and experimental data at Reynolds numbers ranging from $O(100 - 100,000)$, and showed that the onset of flutter is largely independent of Re. From this large set of experimental and simulation data they identified empirical fits for the flutter boundary as a function of M_ρ and K_B in the low- and high-mass ratio regimes. Akcabay and Young [1] found that at low mass ratios the fluid inertia plays a substantial role in the flapping dynamics, and that the stiffness at which flapping initiates is sensitive to flag mass. In this low-mass regime, the fit nearly satisfies $M_\rho \approx K_B$, which shows that flutter occurs when the flag inertia is in balance with the internal stresses in the flag. Akcabay and Young [1] then showed that at higher masses the fluid inertia becomes less important and the critical stiffness at which flapping initiates is roughly constant. In the left plot in figure 4.1, we superimpose our global mode prediction of the flutter boundary onto these empirical fits, and good agreement is seen.

Akcabay and Young [1] also demonstrated that the flapping frequencies at the flutter boundary were largely independent of Re, and determined an empirical fit to this flapping frequency for the large data set they considered. We demonstrate in the right plot of figure 4.1 that the global mode prediction of the flapping frequency (given by the imaginary part of the leading eigenvalue) agrees well with this empirical fit (depicted by the solid black line). We also show that for very massive flags (large M_ρ) the frequency tends towards the value of an Euler-Bernoulli beam in a vacuum (illustrated by the dashed line). Note, however, that the vacuum-scaling is

not reflective of the frequency behavior in the low M_ρ regime where fluid effects dominate.

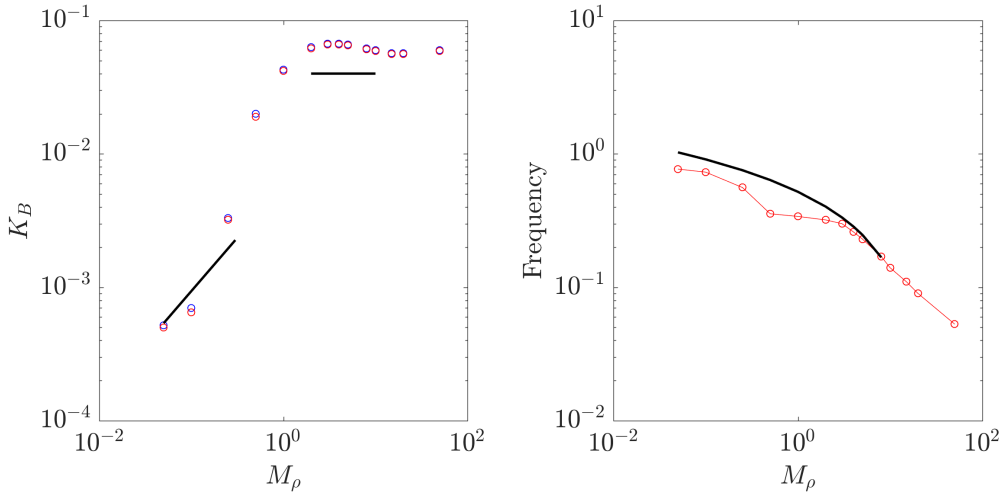

Figure 4.1: Left: modal prediction of the flutter boundary (○) for various mass (M_ρ) and stiffness (K_B) values (stable modes are in blue and unstable modes are in red), along with empirical fits (—) for small masses ($M_\rho < 1/3$) and large masses ($M_\rho > 2$) computed by Akcabay and Young [1] from experimental and computational data over Reynolds numbers $O(100 - 100,000)$. Right: modal frequencies of the unstable mode near the flutter boundary (○-), empirical fit of Akcabay and Young [1] to the aforementioned numerical and experimental data (—).

Mode Characteristics For Different Parameters

We show in figures 4.2–4.4 the leading global modes on the flutter boundary for $M_\rho = 0.05$ ($K_B = 0.005$), $M_\rho = 1$ ($K_B = 0.042$), and $M_\rho = 50$ ($K_B = 0.06$). Note that we change stiffness for the various masses to remain on the flutter boundary, which allows us to identify the modal structure associated with the transition to flapping. In each figure, the real and imaginary part of the modal vorticity is shown on the left and the real and imaginary part of the modal flag shape is shown on the right.

The flag shape has a higher spatial frequency for the low mass ($M_\rho = 0.05$) case than for the other cases [1]. Note that this is reflected in the modal vorticity, as there are more vortical structures on the flag compared with the higher mass modes. In addition, the higher temporal (flapping) frequency of this low mass flag (as given in the right plot of figure 4.1) is reflected in the wake structure – there are more vortical structures in the wake, and each structure is compressed compared to the heavier

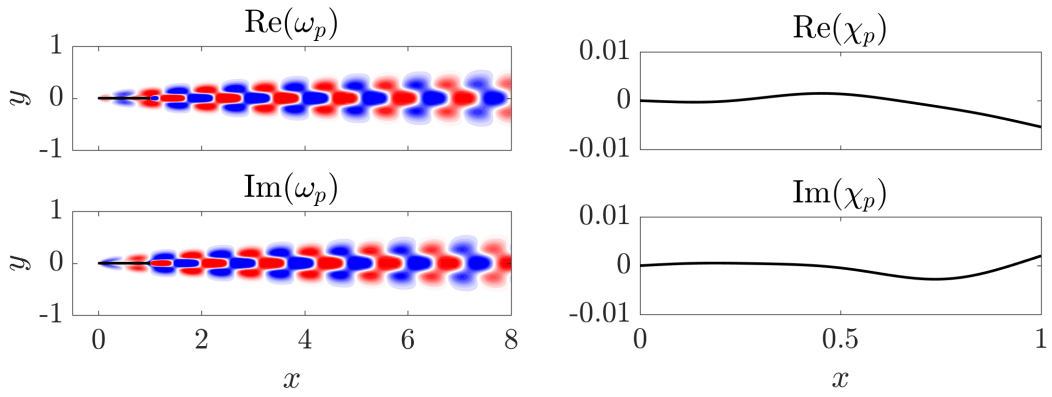

Figure 4.2: Real and imaginary parts of the modal vorticity (left) and flag shape (right) of a conventional flag for $M_\rho = 0.05$, $K_B = 0.005$ (an unstable mode near the flutter boundary). Contours of vorticity are in twenty evenly spaced increments from -0.2 to 0.2.

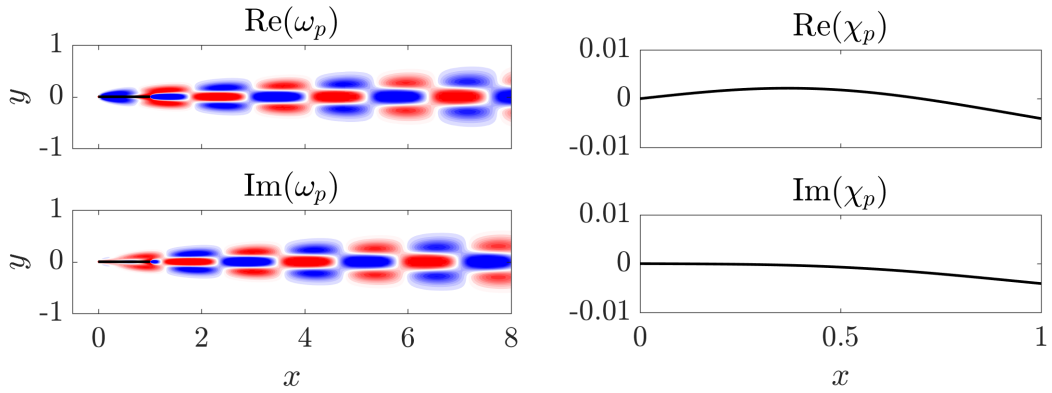

Figure 4.3: Real and imaginary parts of the modal vorticity (left) and flag shape (right) of a conventional flag for $M_\rho = 1$, $K_B = 0.042$ (an unstable mode near the flutter boundary). Contours of vorticity are in twenty evenly spaced increments from -0.2 to 0.2.

flag modes. When the flag and fluid inertias are in balance ($M_\rho = 1$), "lower mode" flapping occurs, with the spatial frequency of the flag decreased from in the light flag case [1]. This is matched by fewer vortical structures on the flag. In addition, the lower temporal flapping frequency is marked by an elongation of vortical structures in the flag wake. In the heaviest case, "lower mode" flapping persists with a similar vortical structure on the flag to what was seen in the $M_\rho = 1$ figure. However, the substantially reduced flapping frequency causes a corresponding lengthening of the wake structures.

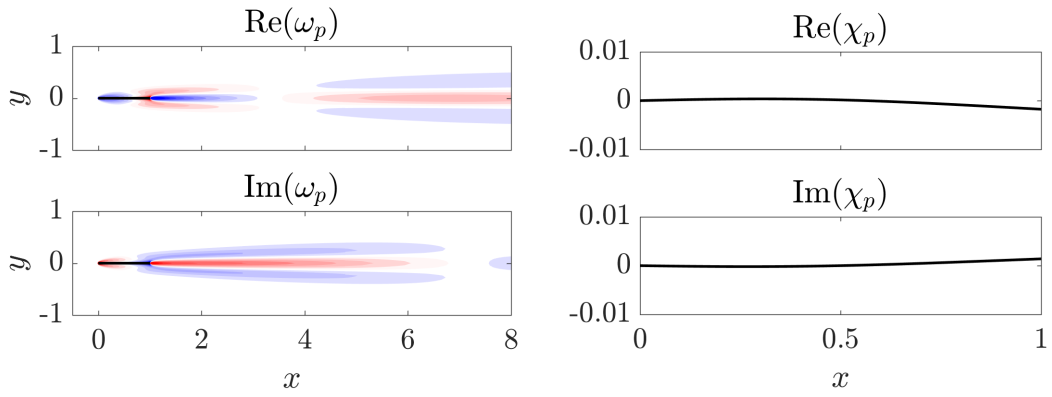

Figure 4.4: Real and imaginary parts of the modal vorticity (left) and flag shape (right) of a conventional flag for $M_\rho = 50$, $K_B = 0.06$ (an unstable mode near the flutter boundary). Contours of vorticity are in twenty evenly spaced increments from -0.2 to 0.2.

4.4 Conclusions

We presented a global stability solver for FSI problems that may be applied to fairly general thin deforming body problems. We validated this solver on the problem of conventional flag flapping, and demonstrated that the global stability analysis of the system accurately predicted the onset of flapping along with the associated flapping frequency. The main purpose of this chapter was to present and validate this global stability solver. We use this analysis in part II to elucidate new physical mechanisms in inverted flag flapping.

Chapter 5

DATA ANALYSIS OF FLUID-STRUCTURE INTERACTION[1]

5.1 Introduction

Data-analysis techniques such as proper orthogonal decomposition (POD) and dynamic mode decomposition (DMD) have been used to elucidate important physical mechanisms and develop reduced-order models for turbulent wall-bounded flows (see, *e.g.*, Berkooz, Holmes, and Lumley [8] for a review), flow past a cylinder [3, 14], and a jet in cross-flow [68, 73], to name a few examples.

These techniques were developed for flows without bodies or flows involving stationary bodies, and have been applied less extensively in the context of fluid-structure interaction (FSI) where the fluid motion is coupled to deformation and/or vibration of an immersed structure. In this FSI setting, data analysis is typically done on data of either the fluid or the structure without incorporating the other. The former approach has been used to identify important flow phenomena for flow past a flexible membrane [73], a cantilevered beam [13], and an elastically-mounted cylinder undergoing vortex-induced vibration [9]. The latter approach has allowed the determination of physics-driving structural behavior in fish swimming [11, 81] and flag flapping [40, 55]. At the same time, incorporating only fluid or structure data does not allow for identification of physical mechanisms in the omitted quantity. Thus, the way in which significant fluid and structure modes are correlated to one another is not revealed through these approaches.

We propose here a framework for data analysis of FSI systems where the fluid and structure are treated together, which allows for important flow features, structural behavior, and their correlation to be identified. As part of this formulation, we define a norm in terms of the total energy of the FSI system. This combined fluid-structure data-analysis procedure is then demonstrated on flapping flags in both the conventional configuration (with the flag pinned at its leading edge) and the inverted configuration (with the flag clamped at its trailing edge; see Kim et al. [40] for details). We first consider limit-cycle flapping for both flag configurations. For the conventional configuration, the dominant mode is shown to contain both

[1]This chapter is based on the publication in preparation Goza and Colonius [29], for which my contributions were devising and implementing the data analysis techniques, running all simulations, and being the primary author of the article.

flapping and vortex shedding that are correlated to one another. Subsequent modes are then identified to not be associated with flapping; they instead reflect harmonic responses of the fluid to the dominant flapping motion. For the inverted configuration, large-amplitude flapping occurs with significant flag motion occurring in both the transverse and streamwise directions. The modal decompositions reflect this, and identify the vortical structures correlated to each distinct motion.

We then use our FSI data-analysis framework to elucidate the driving physical mechanisms of chaotic flapping of conventional flags. Chaotic flapping has been observed in inviscid fluids [2] and for flows at Reynolds numbers of $O(1000)$ [17], and can be triggered by increasing the flag mass: with increasing mass the flag goes from a stable equilibrium state to limit-cycle flapping. Further increasing the mass leads to a growth in the limit-cycle flapping amplitude, and eventually to chaotic flapping. Connell and Yue [17] showed that for viscous flows at moderate Reynolds numbers, the onset of chaos is associated with the appearance of an additional flapping frequency that is a non-integer harmonic of the dominant flapping frequency.

We identify the mechanism responsible for the appearance of this non-integer harmonic. We first show that the increase in flapping amplitude associated with increasing flag mass leads the flag to become sufficiently bluff to the flow at its peak deformation to trigger the bluff-body wake instability. The frequency of this bluff-body mode is not a sub- or super-harmonic of the dominant flapping mode, and is instead reflective of a new physical mechanism. We moreover show that the flapping motion at the non-integer harmonic is a result of a triadic combination of the bluff-body wake-instability with the dominant flapping motion. This triadic consistency is required by the quadratic nonlinearity in the Navier-Stokes equations [21].

We focus here on proper-orthogonal decomposition (POD) and dynamic-mode decomposition (DMD) because of their widespread use and their expected suitability for the problems considered here. The limit-cycle cases described in section 5.3 are associated with one dominant frequency, and thus DMD is a natural candidate because of its localized harmonic nature [54]. POD is also expected to be suitable because of the near-harmonic decomposition it typically yields for limit-cycle flows (such as occurs in vortex shedding past a cylinder near the critical Reynolds number of approximately 47; see, *e.g.*, Kutz et al. [42]). For the chaotic flapping problem described in section 5.4, the non-broadband ('peaky') nature of the system again makes DMD a fitting technique. However, POD and DMD are not ideal for all con-

texts. For example, Towne, Schmidt, and Colonius [84] observed that in statistically stationary flows with broadband frequency content – as are observed in the majority of turbulent flows – spectral POD provides an optimal decomposition. The major goal of the current work is to demonstrate the utility of performing data analysis in a manner that accounts for both the fluid and the structure, rather than advertise a specific decomposition technique. Future work should incorporate the methodology presented here into the appropriate technique for the intended application.

5.2 POD and DMD of fluid-structure interaction

We consider snapshot-based methods of discrete data with associated data matrices organized so that each column provides the state of the system at an instance in time and each row contains the time history of a specific state variable. For simplicity we present our formulation in a two-dimensional setting; the extension to three dimensions is straightforward.

We assume fluid data is given on a stationary Cartesian grid, Ω, made up of n_f points ($\Omega \subset \mathbb{R}^{n_f}$), and let the streamwise and transverse fluid velocities at the i^{th} time instance, t_i, be $\mathbf{u}_i, \mathbf{v}_i \in \Omega$. Fluid data is often provided in this format by immersed boundary methods and experiments; some numerical methods use moving meshes at each time step that conform to the moving structure, and data obtained from these methods would have to be interpolated onto a single stationary grid for all time instances to use the method we propose here.

We assume structural data is provided in a Lagrangian setting, with the structural domain, Γ, comprised of n_s points (Γ depends on time). We let $\boldsymbol{\chi}_i, \boldsymbol{\eta}_i \in \Gamma$ denote the streamwise and transverse structural displacements from an undeformed reference configuration at the i^{th} time instance, and $\boldsymbol{\xi}_i, \boldsymbol{\zeta}_i \in \Gamma$ be the corresponding structural velocities. We define the total state vector at t_i as $\mathbf{y}_i = [\mathbf{u}_i, \mathbf{v}_i, \boldsymbol{\chi}_i, \boldsymbol{\eta}_i, \boldsymbol{\xi}_i, \boldsymbol{\zeta}_i]^T \in \mathbb{R}^{2n_f+4n_s}$, and define the data matrix, $\mathbf{Y} \in \mathbb{R}^{n\times m}$ ($n = 2n_f + 4n_s$ is the size of the state and m is the number of snapshots), as $\mathbf{Y} = [\mathbf{y}_1, \ldots, \mathbf{y}_m]$.

POD modes are computed from the mean-subtracted data matrix, $\tilde{\mathbf{Y}}$, whose i^{th} column is defined as $\tilde{\mathbf{Y}}_i = \mathbf{Y}_i - \boldsymbol{\mu}$, where $\boldsymbol{\mu} = 1/m \sum_{k=1}^{m} \mathbf{y}_k$ is the sample temporal mean of $\mathbf{Y}$. For DMD, Chen, Tu, and Rowley [14] found that the use of $\tilde{\mathbf{Y}}$ reduces DMD to a discrete Fourier transform in time, and that instead using $\mathbf{Y}$ allows for growth-rate information to be retained. For this reason, DMD is performed on $\mathbf{Y}$ below.

Proper orthogonal decomposition

POD decomposes the data into orthogonal uncorrelated modes that are ordered such that the leading k modes ($k \leq m$) provide the most energetically dominant rank k representation of $\tilde{\mathbf{Y}}$. This energetically optimal representation is defined with respect to a norm, and we propose a norm based on the mechanical energy of the FSI system. Defining $\mathbf{x}$ as an Eulerian spatial coordinate and $\mathbf{s}$ as a Lagrangian variable that parameterizes the structure, and letting $u(\mathbf{x}, t)$, $v(\mathbf{x}, t)$, $\chi(\mathbf{s}, t)$, $\eta(\mathbf{s}, t)$, $\xi(\mathbf{s}, t)$, and $\zeta(\mathbf{s}, t)$ be continuous analogues of the discrete variables defined earlier, the mechanical energy in the system is

$$E(t) = \frac{1}{2}\int_{\Omega} u^2(\mathbf{x}, t) + v^2(\mathbf{x}, t)d\mathbf{x} + \int_{\Gamma} \kappa(\chi(\mathbf{s}, t), \eta(\mathbf{s}, t)) + \frac{1}{2}M_{\rho}(\xi^2(\mathbf{s}, t) + \zeta^2(\mathbf{s}, t))d\mathbf{s} \tag{5.1}$$

where Ω and Γ are continuous analogous of the discrete domains defined earlier. The terms corresponding to the fluid and structural velocities represent the kinetic energy in the system (M_{ρ} is the solid-to-fluid mass ratio) and $\kappa(\chi(\mathbf{s}, t), \eta(\mathbf{s}, t))$ is the potential energy within the structure (for deforming bodies this is the strain energy). The potential (strain) energy for flapping flags will be defined in the next section.

While there are a variety of definitions of energy one could use (so long as the result induces a norm), the mechanical energy is a natural choice because it is nonincreasing in time and accounts for the transfer of energy between the fluid and structure apart from viscous dissipation in the fluid. That is, through a straightforward computation one can show that in the absence of body forces and under the assumption that the shear stress is negligible on the boundary of Ω (which occurs for sufficiently large Ω),

$$\frac{dE(t)}{dt} = -\frac{2}{Re}\int_{\Omega} \left(\nabla\mathbf{u} + (\nabla\mathbf{u})^T\right) : \left(\nabla\mathbf{u} + (\nabla\mathbf{u})^T\right) d\mathbf{x} \leq 0 \tag{5.2}$$

In the discrete setting of interest, the corresponding norm is defined as $||(\cdot)||_{\mathbf{W}} \equiv ||\mathbf{W}(\cdot)||_2$, where

$$\mathbf{W} = \begin{bmatrix} \frac{1}{2}\mathbf{I}^{2n_f} & \mathbf{0} & \mathbf{0} \\ \mathbf{0} & \mathbf{L} & \mathbf{0} \\ \mathbf{0} & \mathbf{0} & \frac{1}{2}\sqrt{M_{\rho}}\mathbf{I}^{2n_s} \end{bmatrix} \tag{5.3}$$

In the above, $\mathbf{I}^n$ is the $n \times n$ identity matrix and $\mathbf{L}$ is the operator that maps the structural displacements to the potential energy of the structure. We assume that $\mathbf{L}$ is formulated to be positive definite and symmetric so that $\mathbf{W}$ is positive definite and symmetric.

The inner product associated with this weighting matrix is defined as $\langle \mathbf{q}, \mathbf{p} \rangle_{\mathbf{W}} \equiv \mathbf{q}^T \mathbf{W}^2 \mathbf{p} = (\mathbf{W}\mathbf{q})^T (\mathbf{W}\mathbf{p}) \; \forall \mathbf{q}, \mathbf{p} \in \mathbb{R}^n$ and the induced norm is $||\mathbf{q}||_{\mathbf{W}} \equiv \sqrt{\langle \mathbf{q}, \mathbf{q} \rangle_{\mathbf{W}}} = \sqrt{(\mathbf{W}\mathbf{q})^T (\mathbf{W}\mathbf{q})} \; \forall \mathbf{q} \in \mathbb{R}^n$, which is a discrete approximation of the square root of (5.1) scaled by one on the length between data points, Δx. (This assumes that the distance between points of the fluid and structural domains is equal; unequal spacings can be incorporated into $\mathbf{W}$).

The energetically ordered POD modes with respect to the $\mathbf{W}$-weighted norm may be written in terms of the singular value decomposition (SVD) $\mathbf{W}\tilde{\mathbf{Y}} = \mathbf{U}\mathbf{\Sigma}\mathbf{V}^T$, where $\mathbf{\Sigma}$ is a diagonal matrix containing the singular values $\sigma_1, \ldots, \sigma_m$ ordered by decreasing energy, and $\mathbf{U}$ ($\mathbf{V}$) has columns $\mathbf{u}_j$ ($\mathbf{v}_j$) containing the left (right) singular vectors that correspond to σ_j. In this notation, the POD modes are $\hat{\mathbf{U}} \equiv \mathbf{W}^{-1}\mathbf{U}$ (note that they are orthogonal with respect to the $\mathbf{W}$-weighted inner product). These modes are written in terms of the SVD, but may be computed more efficiently using the method of snapshots [78]. The energetically optimal rank k ($k \leq m$) approximation of a snapshot $\mathbf{y}_i$ may be expressed through an orthogonal projection onto the POD modes as

$$\mathbf{y}_i \approx \sum_{j=1}^{k} \hat{\mathbf{u}}_j^T (\mathbf{W}\mathbf{y}_i) \hat{\mathbf{u}}_j \tag{5.4}$$

Dynamic mode decomposition

Whereas POD modes define an energetically optimal representation of the data, DMD modes are obtained from a linear regression that best represents the dynamics of a (potentially nonlinear) data set. Though there are more general variants [85], we compute DMD modes from the matrix $\mathbf{A}$ that best maps the progression of the state from one time instance to the next; *i.e.*, the $\mathbf{A}$ that best satisfies $\min \sum_{j=1}^{m-1} ||\mathbf{y}_{j+1} - \mathbf{A}\mathbf{y}_j||_2$[2]. This relation can often be satisfied exactly under reasonable conditions on the data (such as linear independence of the columns of $\mathbf{Y}$), and the best-fit matrix is $\mathbf{A} = \mathbf{Y}'(\mathbf{Y}'')^{\#}$, where $\mathbf{Y}' = [\mathbf{y}_2, \ldots, \mathbf{y}_m]$, $\mathbf{Y}'' = [\mathbf{y}_1, \ldots, \mathbf{y}_{m-1}]$, and $(\mathbf{Y}'')^{\#}$ is the pseudo-inverse of $\mathbf{Y}''$.

DMD modes are the eigenvectors of $\mathbf{A}$, denoted as $\mathbf{\Phi} = [\phi_1, \ldots, \phi_{m-1}]$. These modes may be computed efficiently without forming $\mathbf{A}$ explicitly (see [85] for more details). The corresponding eigenvalues, $\hat{\gamma}_1, \ldots, \hat{\gamma}_{m-1}$, are structured such that $\hat{\gamma}_j = e^{\gamma_j \Delta t}$, where Δt is the time step between two snapshots and γ_j is a complex number whose real and imaginary parts give the growth rate and frequency,

[2]The minimization can also be performed with respect to the $\mathbf{W}$-weighted norm, but we retain the use of the standard 2-norm for consistency with most approaches in the literature.

respectively, of mode j. Note that γ_j can be computed from $\hat{\gamma}_j$ via $\gamma_j = \log(\hat{\gamma}_j)/\Delta t$. A k^{th} order ($k \leq m-1$) representation of the system at the i^{th} time instance t_i may be written in terms of the DMD modes as

$$\mathbf{y}_i \approx \sum_{j=1}^{k} c_j e^{\gamma_j t_i} \boldsymbol{\phi}_j \tag{5.5}$$

where $c_j = (\boldsymbol{\Phi}^{\#}\mathbf{y}_1)_j$ represents the initial condition in terms of the j^{th} DMD mode.

The above describes the DMD formulation derived for flows without bodies or flows involving stationary bodies, and may be used without modification for FSI problems to obtain the coupled flow-structure behavior that best represents the full system dynamics.

5.3 Limit-cycle flapping of conventional and inverted flags

The dynamics of conventional- and inverted-flag flapping are governed by the Reynolds number (Re) and the dimensionless mass (M_ρ) and bending stiffness (K_B), defined as

$$Re = \frac{\rho_f U L}{\mu},\ M_\rho = \frac{\rho_s h}{\rho_f L},\ K_B = \frac{EI}{\rho_f U^2 L^3} \tag{5.6}$$

where ρ_f (ρ_s) is the fluid (structure) density, U is the freestream velocity, L is the flag length, μ is the dynamic viscosity of the fluid, h is the flag thickness, and EI is the bending stiffness.

The potential (strain) energy in the flag is given by the flag displacement in the direction normal to the flag. This displacement is written as $\chi_n(s,t)$, where s is the arclength of a material position relative to the leading edge. In this notation, the strain energy is $\kappa(\chi_n(\mathbf{s},t)) = K_B(\partial^2\chi_n/\partial s^2)^2/2$. In the case of inextensible flags considered here, this may be expressed in terms of the streamwise and transverse displacements as $\kappa(\chi(s,t),\eta(s,t)) = K_B(\partial^2\chi/\partial s^2 + \partial^2\eta/\partial s^2)^2/2$. We therefore define the $\mathbf{L}$-submatrix of $\mathbf{W}$ using the standard second-order central difference formula for the χ and η sub-blocks, which results in a symmetric positive definite weighting matrix.

The data for this analysis was obtained using the immersed-boundary method described in chapter 3. The method allows for arbitrarily large flag displacements and rotations, and is strongly-coupled to account for the nonlinear coupling between the flag and the fluid. The method was validated on several flapping flag problems. The physical parameters for each run are described in the subsequent subsections; see

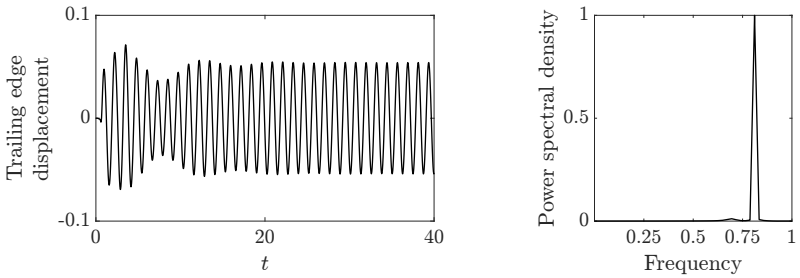

Figure 5.1: Transverse displacement (left) and spectral density (right) of conventional flag flapping for $Re = 500, M_\rho = 0.1, K_B = 0.0001$.

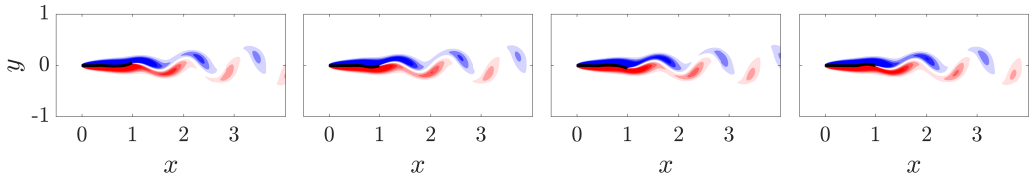

Figure 5.2: Vorticity contours at four snapshots of a flapping period of a conventional flag in limit-cycle flapping with $Re = 500, M_\rho = 0.1, K_B = 0.0001$. Vorticity contours are in 18 increments from -5 to 5.

chapter 3 for details about the simulation parameters such as the grid spacing and time step that were used for the different simulations.

Limit cycle flapping of conventional flags

We consider a POD and DMD analysis of limit-cycle flag flapping of a conventional flag with $Re = 500, M_\rho = 0.1$, and $K_B = 0.0001$. Figure 5.1 shows the transverse displacement of the trailing edge of the flag as a function of time along with the corresponding power spectral density. Our analysis is performed after the transient region, once the system enters periodic behavior of fixed amplitude and frequency (beginning at $t \approx 20$ in figure 5.1). Figure 5.2 shows contours of vorticity at four snapshots in time during a period of flapping in the limit cycle regime. Snapshots were obtained over the range $t \in [20, 40]$ in increments of $\Delta t = 0.05$.

Figure 5.3 shows the singular values σ from POD along with the DMD eigenvalues γ of largest growth rate (real part). The four leading POD modes (which represent approximately 66% of the total system energy) are shown in the top row of figure 5.4. Apart from the mode corresponding to the temporal mean, DMD modes typically come in complex conjugate pairs (*e.g.*, the two leading modes are $\phi_1, \bar{\phi}_1$). We show in the bottom row of figure 5.4 the real and imaginary parts of ϕ_1 and ϕ_2 (the mode corresponding to the temporal mean is not pictured here). The POD and DMD

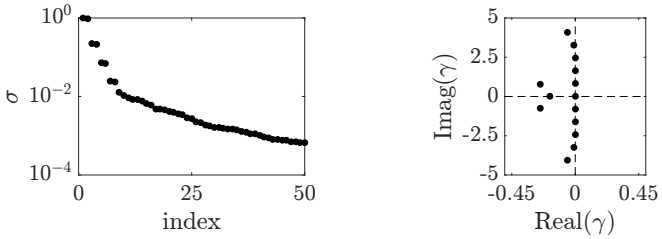

Figure 5.3: POD singular values σ normalized by σ_1 (left) and γ obtained through DMD (right) for limit-cycle flapping of a conventional flag with $Re = 500, M_\rho = 0.1, K_B = 0.0001$.

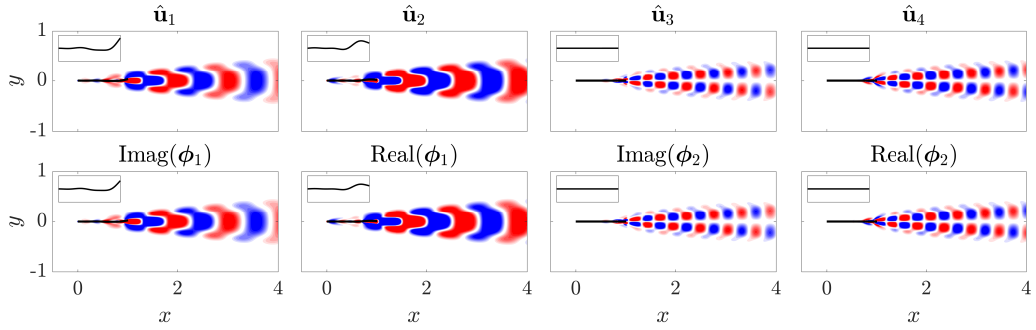

Figure 5.4: Leading POD (top row) and DMD (bottom row) modes for the limit-cycle conventional-flag problem.

modes are nearly identical since this system is characterized by a specific frequency (*c.f.*, figure 5.1). The energetically optimal modes are therefore driving behavior at this dominant frequency and its harmonics. In both decompositions, the first two modes oscillate at the peak frequency of approximately 0.8 depicted in figure 5.1, and the subsequent modes correspond to the higher harmonic of roughly 1.6. The flag behavior is conveyed through the leading two POD modes (leading complex-conjugate pair of DMD modes): these modes represent phase-shifted flapping at the dominant frequency to create the traveling wave behavior of high spatial frequency that the flag undergoes for these parameters [17]. The two leading modes also demonstrate the creation and advection of vortices associated with flapping. The higher modes are not associated with flag flapping (this information is conveyed entirely through the leading modes), and instead describe the higher-harmonic fluid responses to this dominant flapping motion.

Finally, we note that low-order decompositions accurately reproduce the system dynamics. Figure 5.5 shows snapshots of the same four time instances as shown in figure 5.2 using reconstructions from the six leading modes for both POD and DMD.

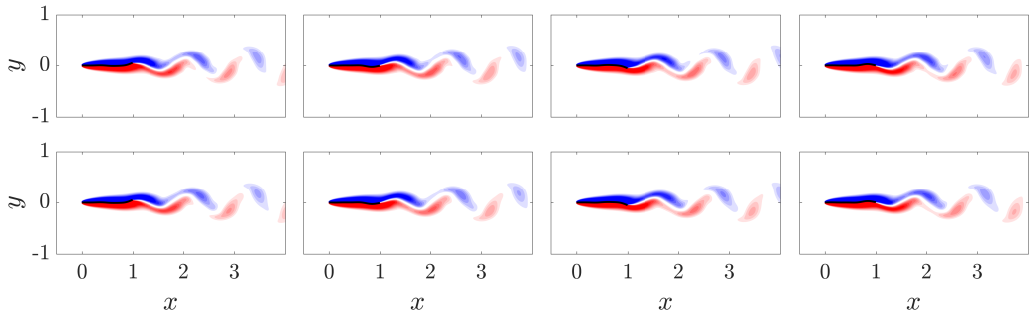

Figure 5.5: Six mode POD (top row) and DMD (bottom row) reconstructions of the system for the snapshots in figure 5.2. Vorticity contours are in 18 increments from -5 to 5.

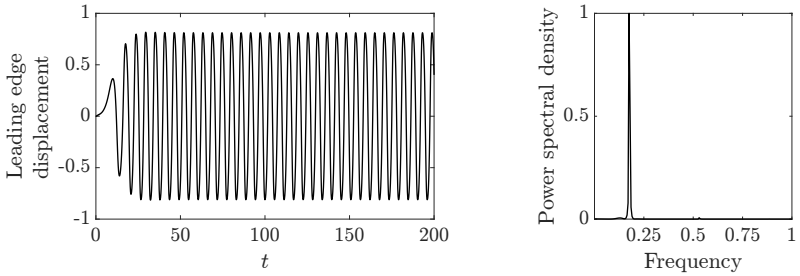

Figure 5.6: Transverse displacement (left) and spectral density (right) of limit-cycle flapping of an inverted flag for $Re = 200, M_\rho = 0.5, K_B = 0.35$.

Limit cycle flapping of inverted flags

We now consider a POD and DMD analysis of limit cycle flag flapping of an inverted flag with $Re = 200, M_\rho = 0.5$, and $K_B = 0.35$. Figure 5.6 shows the transverse displacement of the trailing edge of the flag as a function of time along with the corresponding power spectral density. Our analysis is performed after the transient region, once the system enters periodic behavior of fixed amplitude and frequency (beginning at $t \approx 30$ in figure 5.6). Figure 5.7 shows contours of vorticity at four snapshots in time during a half-period of flapping in the limit cycle regime. Snapshots were obtained over the range $t \in [100, 165]$ in increments of $\Delta t = 0.05$.

Figure 5.3 shows the singular values σ from POD along with the values γ with the largest growth rate (real part) obtained through DMD. The four leading POD modes (which represent approximately 88% of the total system energy) and DMD modes (omitting the mode corresponding to the temporal mean) are shown in figure 5.9. As with the previous example, the dominant frequency signature of this system leads to similar POD and DMD modes (*i.e.*, POD essentially results in a harmonic decomposition). In this case, the first and third POD modes (leading complex-

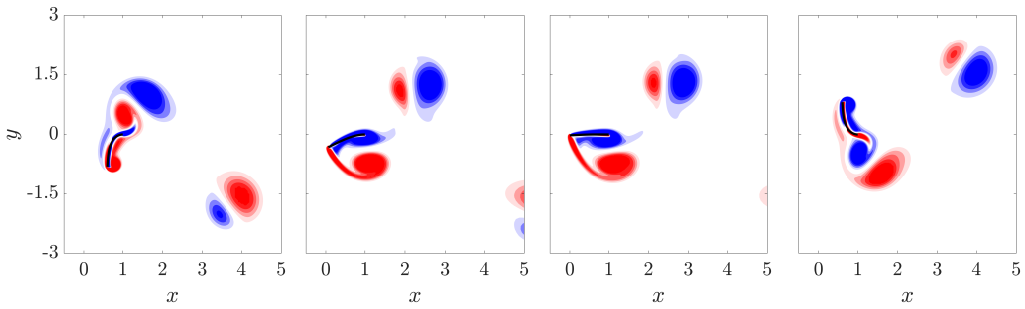

Figure 5.7: Vorticity contours at four snapshots of a half-period of an inverted flag in limit-cycle flapping with $Re = 200, M_\rho = 0.5, K_B = 0.35$. Vorticity contours are in 18 increments from -5 to 5.

conjugate pair of DMD modes) oscillate at the dominant frequency of roughly 0.18 and the other pictured modes correspond to the higher harmonic of 0.36.

For this large-amplitude flapping problem, significant flag motion occurs in both the transverse and the streamwise directions, and both POD and DMD decompose this different behavior into separate modes. In the case of POD, the leading mode expresses the transverse motion of the flag. It also identifies the creation of the leading edge vortex at the flag's peak displacement, and the downstream advection of this vortex. The third POD mode oscillates at the same frequency of the leading mode and does not convey any flapping information, but instead provides a phase-shifted set of vortical structures to those of the first mode that, along with the leading mode, represent the dominant vortex-shedding behavior. By contrast, the second POD mode describes the streamwise displacement of the flag, which oscillates at double the frequency since for every period of flapping there are two peaks in streamwise displacement for each peak in transverse displacement. The second mode also describes a fine-scale leading-edge vortical structure that beats at twice the frequency of the leading-edge structures depicted in the first mode, as well as the creation and advection of the trailing edge vortex formed when the flag is at its peak displacement. Analogous to the third POD mode, the fourth POD mode does not describe flag motion, and instead provides phase-shifted vortex shedding to that of the second mode to provide the dominant fluid behavior at the higher frequency harmonic.

The DMD modes are similar to the POD modes, except that the imaginary part of the leading mode corresponds to the third POD mode and the real part of the second mode corresponds to the second POD mode, as DMD requires that a given mode oscillate at the same frequency. Note also that the imaginary part of the leading

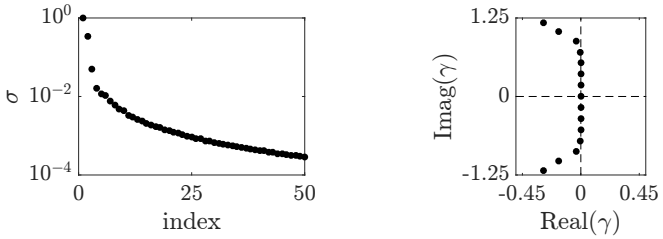

Figure 5.8: POD singular values σ normalized by σ_1 (left) and γ obtained through DMD (right) for limit-cycle flapping of an inverted flag with $Re = 200, M_\rho = 0.5, K_B = 0.35$.

DMD mode is associated with a slightly deflected flag, and therefore describes minor modifications to the flapping behavior described in the real parts of modes 1 and 2. This is unlike in POD, where the first and third modes entirely describe the flapping motion. This distinction attests to the energetic efficiency of conveying flapping information for this system using a minimal number of modes. It also provides an explanation for why the singular values are not ordered in pairs in figure 5.8: the first POD mode conveys both fluid and flapping information, whereas the third POD mode only conveys fluid motion that occurs at the same frequency as the first mode (this conclusion applies to modes two and four as well).

We note that one consequence of decomposing transverse and streamwise displacements into separate modes is that a given mode may not correspond to motion of an inextensible flag. However, as seen from the six mode-POD and DMD reproductions of the dynamics shown in figure 5.10, only a few modes are necessary to describe the inextensible nature of the flag for this problem.

5.4 Chaotic flapping of conventional flags

Chaotic flapping of conventional flags can be triggered for flags of low stiffness (K_B) by increasing the flag mass (M_ρ). For flows at moderate Reynolds numbers of $O(1000)$, the system transitions with increasing mass from a stable equilibrium to limit-cycle flapping of increasing amplitude, then to chaotic flapping [17]. Similar transitions occur in inviscid fluids [2]. We focus here on the case of moderate Reynolds number; establishing similarities in the driving mechanisms is an avenue of future work.

We show in figure 5.11 the tip displacement and spectral density of conventional-flag flapping for $M_\rho = 0.18$ and $M_\rho = 0.25$ (the other parameters were $Re = 500$ and $K_B = 0.0001$ for both cases). These M_ρ values are near the critical value for

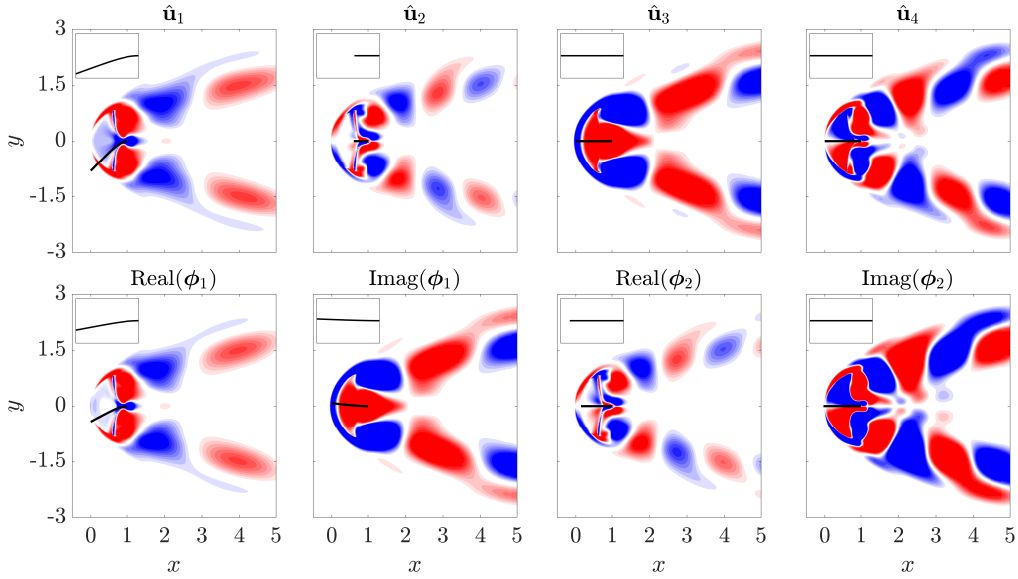

Figure 5.9: Leading POD (top row) and DMD (bottom row) modes for the limit-cycle inverted-flag problem.

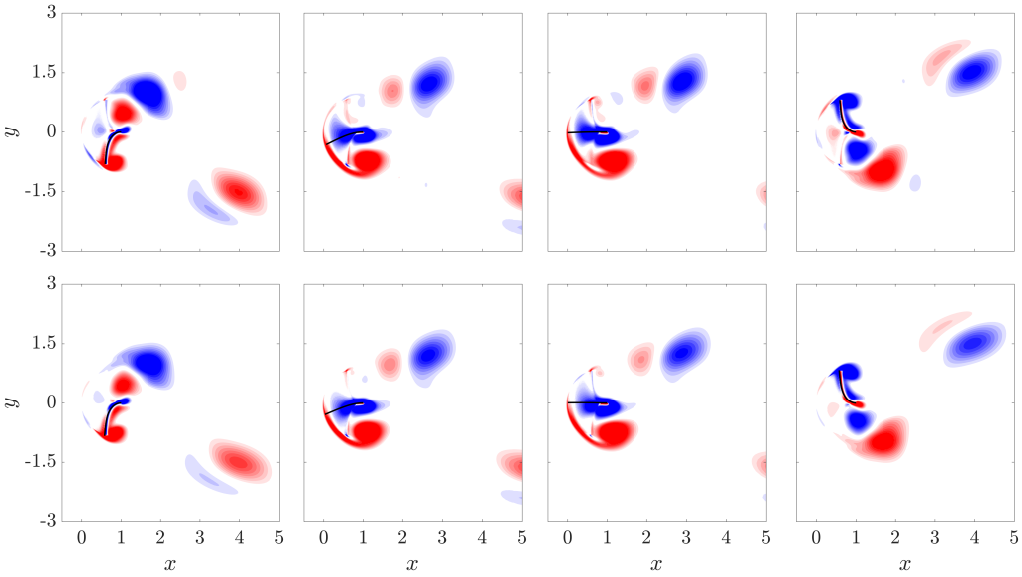

Figure 5.10: Six mode POD (top row) and DMD (bottom row) reconstructions for the same snapshots as in figure 5.7. Vorticity contours are in 18 increments from -5 to 5.

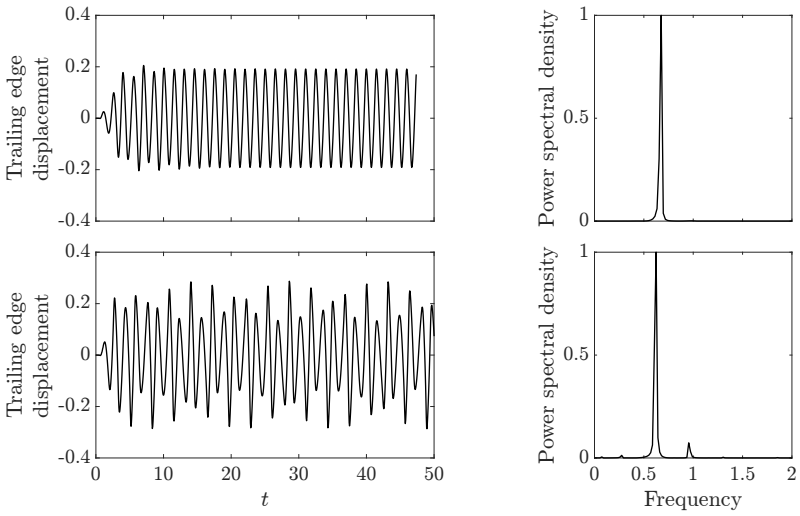

Figure 5.11: Transverse displacement (left) and spectral density (right) of conventional-flag flapping for $Re = 500$ and $K_B = 0.0001$. Top row: limit-cycle flapping ($M_\rho = 0.18$); bottom row: chaotic flapping ($M_\rho = 0.25$).

which chaos is triggered. For $M_\rho = 0.18$, limit cycle flapping occurs with a single dominant frequency (note the increased flapping amplitude from the $M_\rho = 0.1$ case of the previous section due to the increase in mass ratio). The flapping amplitude increases for $M_\rho = 0.25$ and flapping becomes chaotic with multiple frequencies present. Connell and Yue [17] observed that the sub-dominant frequency coincides approximately with the 3/2 harmonic of the dominant frequency in this chaotic regime. While the half-harmonic is not present in a spectrum of the flag's motion, Connell and Yue [17] argued that chaos is related to period doubling in the sense that the 3/2 harmonic is periodic over a period of the half-harmonic. Using a DMD analysis within our FSI framework, we propose in this section that the onset of chaos is caused by a different mechanism. DMD is selected to isolate behavior at distinct frequencies; this can be done in a POD context using spectral POD (SPOD) [84], and an avenue of future work is to compare the results of DMD and SPOD for this problem.

To contrast DMD modes in the chaotic regime with those from a limit cycle near the onset of chaos, we first show in figures 5.12 and 5.13 the DMD eigenvalues γ and four leading modes ϕ (omitting the mode associated with the mean) for the limit-cycle case of $M_\rho = 0.18$. Note that the modal decomposition is similar to that of the lower mass ratio despite the increase in amplitude. The leading mode captures nearly all flapping behavior, has vortical structures similar to those for the lower mass ratio, and has a corresponding eigenvalue at the dominant flapping frequency. Moreover,

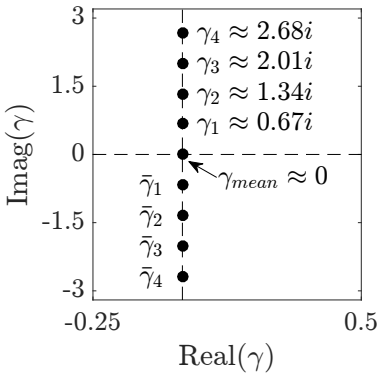

Figure 5.12: DMD eigenvalues γ for limit-cycle flapping of a conventional flag with $Re = 500, M_\rho = 0.18, K_B = 0.0001$.

subsequent modes have eigenvalues at harmonics of the dominant frequency and are associated with negligible flag motion. That is, they correspond to harmonic responses in the fluid to the flag motion captured by the leading mode.

We now show in figures 5.14 and 5.15 the DMD eigenvalues γ and four leading modes ϕ (omitting the mode associated with the mean) for the chaotic case of $M_\rho = 0.25$. The dominant and non-integer harmonic frequencies from the nonlinear simulations manifest themselves in DMD modes ϕ_1 and ϕ_3. Note that despite the significant change in behavior from the limit-cycle regime, ϕ_1 remains largely unchanged. Yet, due to the increased system complexity, flapping is no longer conveyed entirely through the first mode, and both ϕ_1 and ϕ_3 are associated with flapping motion and a correlated set of flow features.

By contrast, ϕ_2 is not associated with flapping (the flag mode in the insert is undeformed). This is consistent with the absence of the γ_2 frequency in the spectral density plot of figure 5.11 (the small peak at low frequency in figure 5.11 corresponds to $\gamma_4 \approx 0.27$). Thus, the mode represents a response of the fluid to the dominant flapping motion. The pronounced shear layers at the top and bottom peak displacement and the corresponding wake vortices are reflective of a bluff-body vortex-shedding mode that appears because of the increased flapping amplitude compared with the limit-cycle case. This is further evidenced by the modal frequency, which agrees with the classical 0.2 Strouhal scaling [66] when normalized by the projected length of the maximum peak-to-peak-amplitude ($0.35 \times 0.5 \approx 0.18$). Note also that γ_2 is not a sub-harmonic of the dominant flapping frequency γ_1, and thus this bluff-body mode is reflective of the appearance of a new physical mechanism rather than of resonance or harmonic interactions.

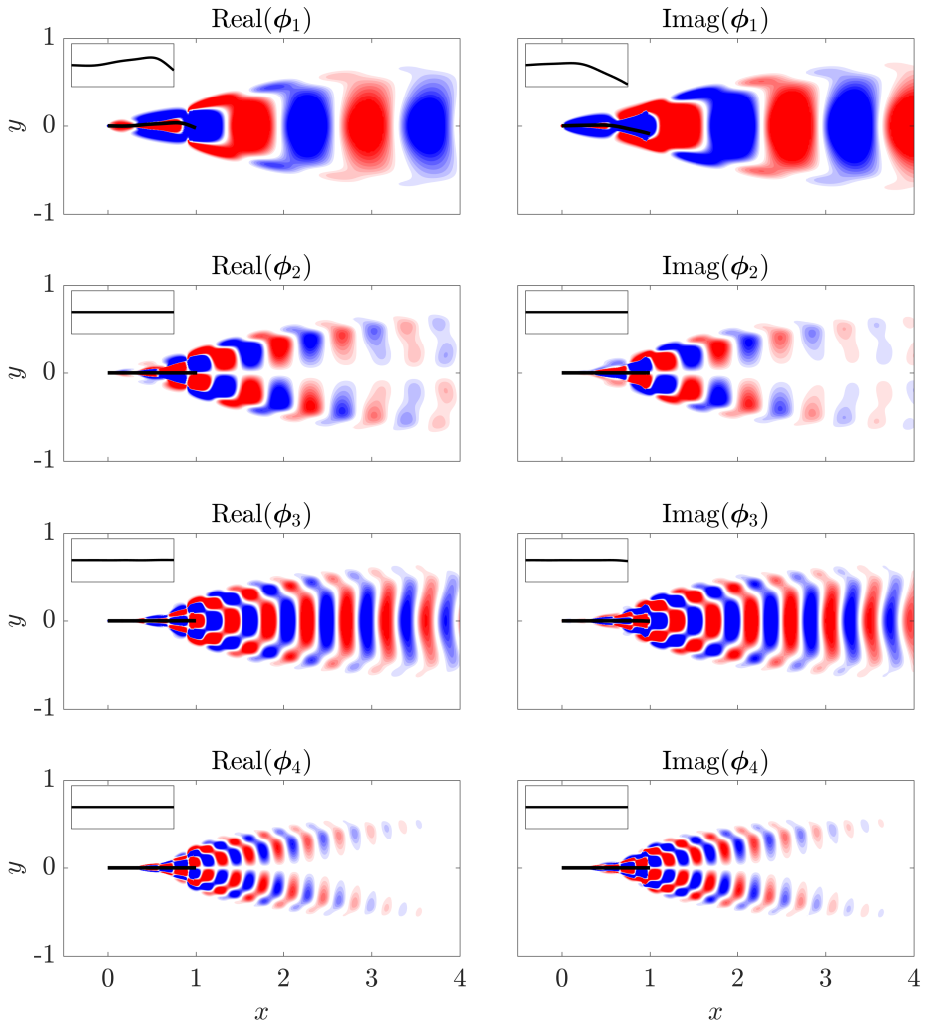

Figure 5.13: Leading DMD modes for the limit-cycle conventional-flag problem with $Re = 500$, $K_B = 0.0001$, $M_\rho = 0.18$.

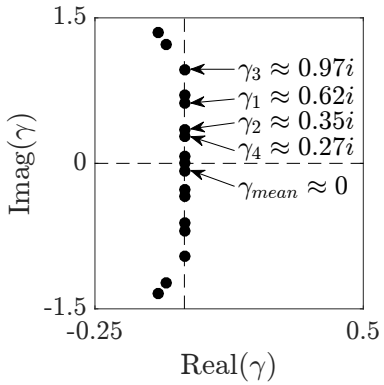

Figure 5.14: DMD eigenvalues γ for chaotic flapping of a conventional flag with $Re = 500$, $M_\rho = 0.25$, $K_B = 0.0001$.

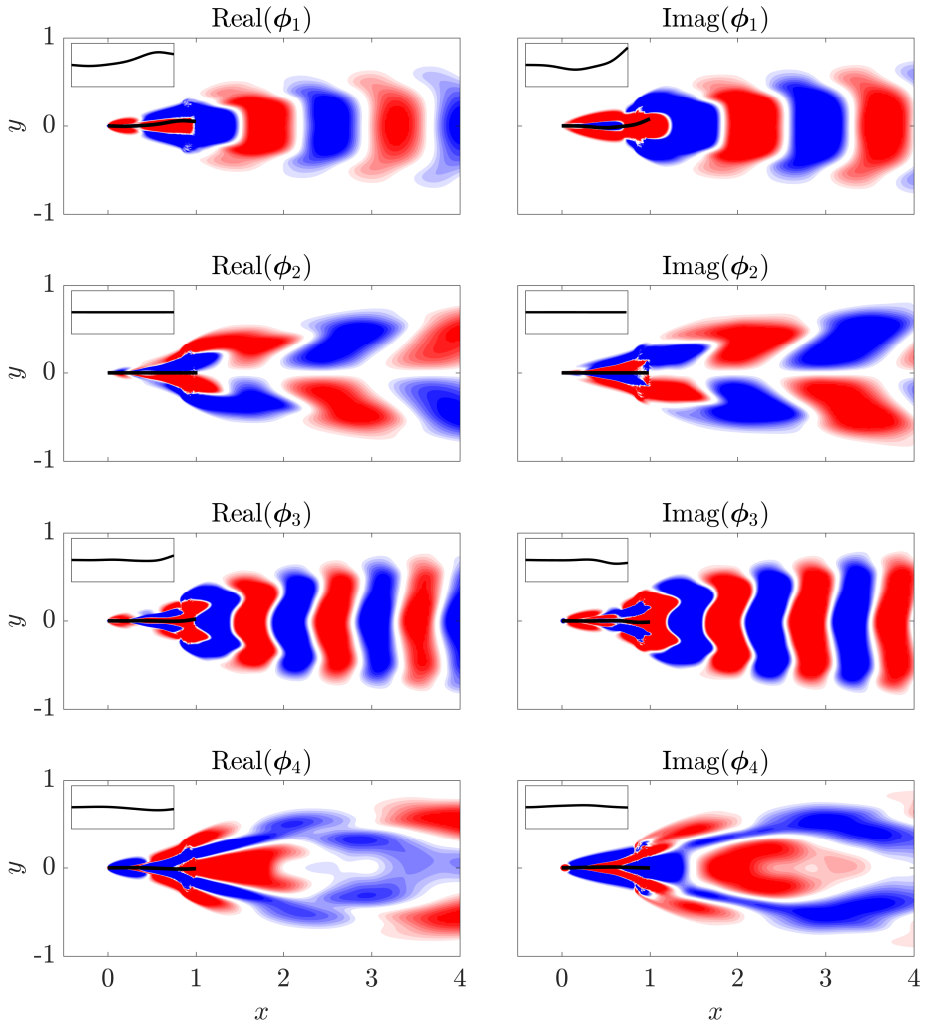

Figure 5.15: Leading DMD modes for chaotic flapping of a conventional flag with $Re = 500, M_\rho = 0.25, K_B = 0.0001$.

This bluff-body mode is key to understanding the sub-dominant flapping behavior of the flag occurring at frequency γ_3: the sub-dominant frequency is a triadic combination of the frequencies of the dominant flapping mode and the bluff-body mode; *i.e.*, $\gamma_3 = \gamma_1 + \gamma_2$. Moreover, the other sub-dominant frequency of approximately 0.27 in figure 5.11 is manifested in ϕ_4, which is also a triadic combination of ϕ_1 and ϕ_2 ($\gamma_4 = \gamma_1 - \gamma_2$). The triadic interaction of oscillatory behavior are required by the quadratic nonlinearity of the advective term in the Navier-Stokes equations [21].

5.5 Conclusions

While data analysis of fluid systems is a pervasive tool for understanding driving physical mechanisms, its application to FSI problems remains limited. For these FSI problems, data analyses are often performed only on data of fluid or structure variables, rather than incorporating both. Thus, modes are not identified for the omitted quantity. Moreover, correlations between physical mechanisms in the flow and structure can not be determined through this approach.

We presented a formulation for performing data analysis on FSI problems that accounts for both the fluid and the structure. We designed this formulation to be compatible with the manner in which data is typically obtained for experiments and nonconforming mesh simulations. As part of this framework, we defined a physically meaningful norm for FSI systems. We considered POD and DMD because of their widespread use, but extensions to other methods are straightforward. The main goal of this work was to demonstrate the utility of performing data analysis on FSI problems in a way that accounts for both the fluid and the structure, rather than promote a specific data-analysis method. Future work should incorporate the above-described methodology into the appropriate decomposition technique for the problem of interest.

Our formulation was first applied to limit-cycle flapping of flags in the conventional and inverted configuration. Because of the dominant frequency associated with this limit-cycle behavior, both POD and DMD give similar decompositions. In the conventional-flag case, the leading two POD modes (leading complex-conjugate pair of DMD modes) convey both the flapping information of the flag and the dominant vortical structures associated with this motion. Subsequent modes describe harmonic responses in the fluid to the flapping described in the leading modes. In the inverted-flag case, large-amplitude flapping occurs and significant flag motion is exhibited in the transverse and streamwise directions. POD separates these motions, with the leading mode describing flag and fluid structures associated with transverse motion and the second mode conveying correlated flag and fluid behavior from streamwise motion. All flapping information is conveyed through these first two POD modes, with the remaining modes again presenting harmonic responses in the fluid to this dominant flag motion. DMD yields a similar decomposition, though slight mixing of the transverse and streamwise flag motion occurs for the two leading modes.

Finally, the physical mechanism driving chaotic flapping of conventional flags was

clarified. Connell and Yue [17] identified that the transition from limit-cycle flapping to chaotic flapping coincides with the appearance of a new flapping frequency that near the 3/2 harmonic of the dominant flapping frequency. We identified the mechanism driving this non-integer harmonic through a DMD analysis. We first demonstrated that at the onset of chaos, the flag becomes sufficiently bluff at its peak deflection to initiate a bluff-body wake instability. This is in contrast to limit-cycle flapping, where flapping amplitudes are smaller and this bluff-body instability is not instigated. The associated shedding frequency of this new behavior coincides with the Strouhal scaling of 0.2 common to bluff-body flows [66]. Moreover, we demonstrated that this bluff-body mode combines triadically with the dominant flapping behavior to produce the observed flapping near the 3/2 harmonic.

Finally, we note that data analysis is often used to develop reduced-order models of complex flow. For FSI systems, these models are typically derived by performing a data-driven decomposition of the fluid and coupling this to the full governing equations for the structure (see Dowell and Hall [20] for a review). This approach may require more modes than those derived from a combined fluid-structure treatment, and there are avenues for future work in evaluating the efficiency of our proposed data-analysis technique in the context of reduced-order models.

Chapter 6

OUTLOOK

In part I of this thesis, we developed numerical tools for performing high-fidelity simulations and analysis of FSI systems. Yet, there are many opportunities for further development of the work described in chapters 2–5. For computing accurate surface stresses (chapter 2), we demonstrated that more differentiable smeared delta functions lead to smoother, higher fidelity stresses. Smoother delta functions typically have a wider support and therefore involve a larger computational cost, and future work could identify narrower-width delta functions that retain sufficient smoothness to preserve the desired accuracy in the computed stresses and forces.

In the context of the FSI method we developed (chapter 3), the solver is based on a two-dimensional (2D) discrete streamfunction-vorticity formulation. While a primitive-variable formulation was presented that could be applied in 2D or 3D, this has yet to be implemented, and accomplishing this (particularly in 3D) could enable simulations of a wider range of FSI systems. Finally, for either the streamfunction-vorticity or primitive-variable formulation, the IB method places fictitious fluid inside of bodies that produces unphysical contributions to the surface stresses for any body of finite thickness. For this reason, the current FSI algorithm is only valid for thin structures. While the unphysical contributions of the fictitious fluid can be removed in rigid body problems [43], doing so for thick deforming bodies remains a challenge.

For global stability analysis of FSI systems (chapter 4), the same restriction to thin structures applies, and again extending the applicability of the solver to thick bodies would allow for a wider range of FSI problems to be studied. In addition, the linear systems involved in FSI problems are typically large, and there are inherent challenges to computing the associated eigenvalues and eigenvectors. Our current approach uses a shift-and-invert procedure, which involves an LU factorization of the linear system. Performing this decomposition may be infeasible for problems of larger dimension than we have considered, and other means of computing the eigenvalues and eigenvectors would have to be adopted (*e.g.*, using an Arnoldi method based on snapshots from the linearized time-stepper [4]). We note that the use of these alternative methods would be particularly important if the 3D

primitive-variable formulation is adopted due to the increase in dimensionality of the system.

For data analysis of FSI systems (chapter 5), we have thus far only consider problems in which behavior is associated with a specific frequency, and applying this analysis to dynamical systems with more broadband frequency content could elucidate physical mechanisms in this more complex scenario. Additionally, our formulation was developed for POD and DMD, and extending this derivation to other snapshot-based methods would provide a larger tool set for understanding FSI systems.

Part II

Physics of inverted flag flapping

Chapter 7

INTRODUCTION[1]

Uniform flow past a conventional flag – where the flag is pinned or clamped at its leading edge with respect to the oncoming flow – has been studied widely beginning with the early work of Taneda [80] (see Shelley and Zhang [76] for a recent review). By contrast, studies of flow past an inverted flag, in which the flag is clamped at its trailing edge, have only been reported recently. The inverted-flag system displays a wide range of dynamical regimes [32, 40, 69], many of which are depicted in figure 7.1. This figure is produced from the numerical simulations described in section 8.1.

One of the dynamical regimes depicted is large-amplitude flapping (figure 7.1d), which is associated with a larger strain energy than that of conventional flag flapping. These large bending strains make the inverted-flag system a promising candidate for energy harvesting technologies that convert strain energy to electricity, *e.g.*, by using piezoelectric materials. Shoele and Mittal [77] studied this energy harvesting potential in detail by performing numerical simulations of a fully-coupled fluid-structure-piezoelectric model.

Transitions between the various regimes in figure 7.1 depend on the Reynolds number (Re), dimensionless mass ratio (M_ρ), and dimensionless bending stiffness

[1]This part of the thesis is based on the publication in preparation Goza, Colonius, and Sader [30], for which my contributions were identifying the mechanism responsible for the onset of flapping, distinguishing parameters under which vortex-induced vibration occurs in large-amplitude flapping, characterizing the chaotic regime, running all simulations, and being the primary author of the article.

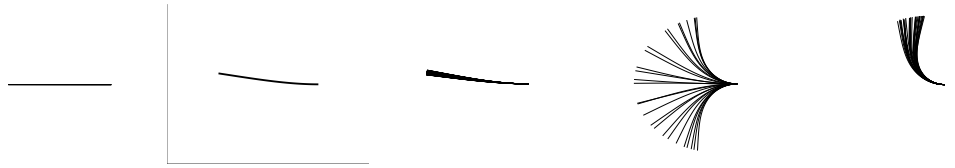

(a) (b) (c) (d) (e)

Figure 7.1: Time lapses of flag position for (a) the undeformed equilibrium, (b) small-deflection stable, (c) small-deflection deformed flapping, (d) large-amplitude flapping, and (e) deflected-mode regimes. In all figures, the flag is clamped at its right edge and the flow direction is from left to right.

(K_B), defined as

$$Re = \frac{\rho_f U L}{\mu},\ M_\rho = \frac{\rho_s h}{\rho_f L},\ K_B = \frac{EI}{\rho_f U^2 L^3} \tag{7.1}$$

where ρ_f (ρ_s) is the fluid (structure) density, U is the freestream velocity, L is the flag length, μ is the shear viscosity of the fluid, h is the flag thickness, and EI is the flexural rigidity of the flag. In experiments, regime transitions are triggered by increasing the flow rate [40]. This coincides with a decrease in K_B and an increase in Re for fixed M_ρ, by virtue of (7.1). In contrast, numerical simulations often decrease the flag's stiffness at fixed Re and M_ρ, which isolates the effect of various parameters and facilitates comparison to previous numerical studies of flow-induced vibration.

Simulations show that for moderate Reynolds numbers ($\lesssim 1000$), a systematic decrease in K_B causes a change from a stable undeformed equilibrium state (figure 7.1a) to a small-deflection stable state (figure 7.1b). This is followed by a transition to small-deflection deformed flapping (figure 7.1c), then to large-amplitude flapping (figure 7.1d), and finally to a deflected-mode regime (figure 7.1e) [32, 69]. These simulations have been performed primarily for $M_\rho \leq O(1)$ (heavy fluid loading), though Shoele and Mittal [77] considered large values of M_ρ.

The same regime transitions persist at higher Reynolds numbers, $Re \sim O(10^4)$, except that the small-deflection stable and small-deflection deformed flapping regimes discussed above are no longer present. That is, the undeformed equilibrium directly gives way to large-amplitude flapping [40]. Moreover, Sader et al. [71] experimentally identified a chaotic flapping regime (not shown in figure 7.1) at these higher Reynolds numbers that has yet to be reported using numerical simulations with $Re \leq O(1000)$.

At low Reynolds numbers ($Re < 50$), numerical simulations have shown that the inverted flag's dynamics can change significantly: no flapping occurs, with the only observed regimes being the undeformed equilibrium and stable deflected states [69]. These simulations were performed over a wide range of K_B for only one value of M_ρ, and the system's dependence on these two parameters remains an open question at these lower Reynolds numbers.

Several driving mechanisms of the various regimes illustrated in figures 7.1(a)–(e) have been identified. The bifurcation from the undeformed equilibrium is caused by a divergence instability (*i.e.*, the instability is independent of M_ρ). This mechanism

was originally suggested by Kim et al. [40], and subsequently found computationally [32] and mathematically via a linear stability analysis [71]. For large-amplitude flapping, Sader et al. [71] used experiments and a scaling analysis to argue that this regime is a vortex-induced vibration (VIV) for a range of parameters. The primary role of vortex shedding in large-amplitude flapping is further evidenced by the above-mentioned observation of Ryu et al. [69] that flapping does not occur below $Re \approx 50$ (for certain values of M_ρ). The aforementioned scaling analysis of Sader et al. [71] was also used to predict that VIV should cease as the mass ratio, M_ρ, increases – a prediction that is yet to be verified. With respect to the deflected-mode regime, small-amplitude flapping about a large mean-deflected position occurs, and Shoele and Mittal [77] showed that the flapping frequency is identical to that of the vortex shedding caused by the flag's bluffness.

We use here high-fidelity nonlinear simulations and a global linear stability analysis to further characterize the regimes in figure 7.1 and explore their driving physical mechanisms. We emphasize that our global stability analysis is based on a linearization of the fully-coupled fluid-structure system of equations. Moreover, the computed equilibria are steady-state solutions of the fully-coupled nonlinear equations described in section 8.1. Our results are presented for Reynolds numbers of 20 and 200, various values of K_B, and values of M_ρ spanning four orders of magnitude.

Using this approach, we (i) study the mechanisms responsible for the onset of small-deflection deformed flapping, (ii) probe the role of vortex shedding and VIV in large-amplitude flapping, and (iii) investigate whether chaotic flapping occurs at low-to-moderate Reynolds numbers ($Re = 20$ and 200). To explore (i), we first demonstrate that the small-deflection stable state is an equilibrium of the fully-coupled fluid-structure system. Through a global stability analysis, we show that the subsequent transition to small-deflection deformed flapping (figure 7.1c) as the bending stiffness decreases is a supercritical Hopf bifurcation of this deformed equilibrium. For point (ii), we confirm the arguments of Sader et al. [71] that large-amplitude flapping is a VIV for $Re = 200$ and lower values of the mass ratio, $M_\rho < O(1)$. We then show that the nature of flapping in this large-amplitude regime qualitatively changes for large M_ρ, consistent with the scaling analysis of Sader et al. [71]. Large-amplitude flapping is also shown to occur for large M_ρ at the lower Reynolds number of $Re = 20$. Vortex shedding is absent at this low Reynolds number, and flapping thus occurs through a non-VIV mechanism. Consistent with the simulation results of Ryu et al. [69], we find no flapping at this low Reynolds

number for $M_\rho < O(1)$. Finally, with respect to (iii), we confirm that chaotic flapping persists at moderate Reynolds numbers ($Re = 200$) for light flags with $M_\rho < 1$, and demonstrate that the structure of the associated strange attractor is controlled by a combination of the large-amplitude and deflected-mode regimes. Chaos does not occur for heavy flags at $Re = 200$ or for any mass ratio considered at $Re = 20$. Thus, chaos is associated with parameters for which VIV flapping occurs.

We contextualize the simulation results over this wide range of parameters using bifurcation diagrams. These provide an overview of the equilibria, their stability, and the flapping dynamics. Figure 7.2 shows an *illustrative* bifurcation diagram that summarizes what will be shown in later sections. In these bifurcation diagrams, the leading edge transverse displacement (tip displacement) is plotted versus the flag flexibility ($1/K_B$) for a particular choice of Re and M_ρ (see the caption for details). Note that even though the undeformed and deformed equilibria become unstable with a decrease in K_B, they nonetheless remain as equilibria of the system. We demonstrate below through a global stability analysis that these unstable deformed equilibria are key to understanding a variety of flapping behavior of the inverted-flag system.

Two-dimensional (2D) simulations are presented throughout. As mentioned above, many similarities exist between the 3D experiments of [40] and 2D simulations of [32, 69, 77]. This suggests that features of the 2D dynamics persist in 3D (though Sader, Huertas-Cerdeira, and Gharib [70] demonstrated that substantial differences occur for low-aspect ratio flags). Yet, 3D effects could alter the critical parameters at which bifurcations occur, as well as the mechanisms driving these bifurcations. Exploring these similarities and differences between 2D and 3D geometries is a subject of future work and is not considered here. Quantities presented below are dimensionless, with length scales, velocity scales, and time scales nondimensionalized by L, U, and L/U, respectively.

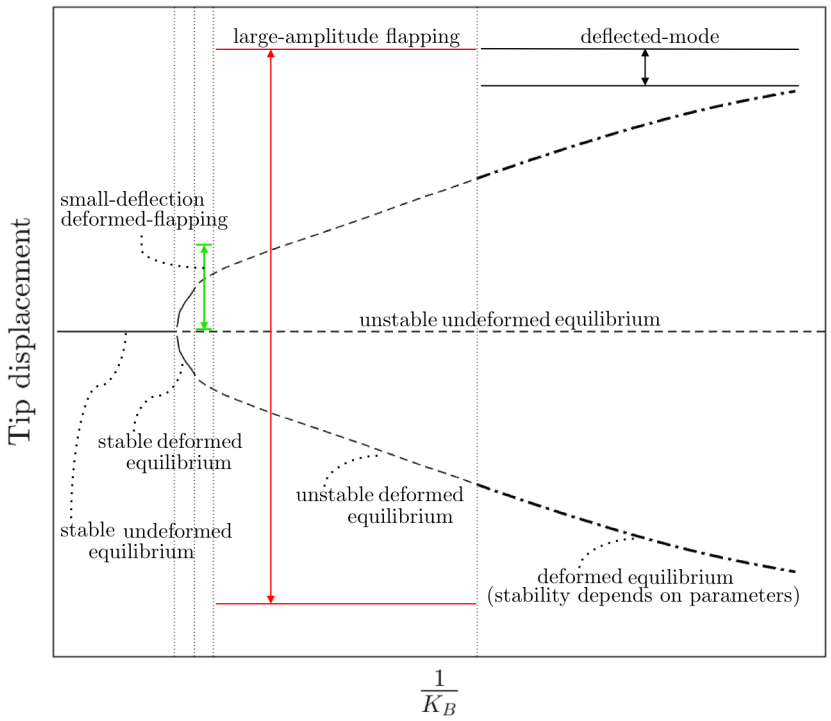

Figure 7.2: A schematic bifurcation diagram that summarizes the results obtained for various parameters considered in the present work. Equilibria are presented by lines (—, stable equilibria; – –, unstable equilibria; • —, stability depends on parameters). The lines with the double arrows indicate regimes where flapping occurs, with the top and bottom lines representing the peak-to-peak flapping amplitude. The diagram shows that with decreasing K_B (moving left to right), the system transitions from the undeformed equilibrium to a stable deformed equilibrium. Following this, the system bifurcates to small-deflection deformed flapping, then large-amplitude flapping (chaotic flapping can also occur in this regime depending on parameters), and finally to a deflected-mode regime whose dynamics depend on Reynolds number: for $Re = 20$, no flapping occurs and the large-deflection state is an equilibrium of the fully-coupled system; for $Re = 200$, the large-deflection state is characterized by small-amplitude flapping. The above diagram only corresponds to cases when flapping occurs. For $Re = 20$ and $M_\rho < O(1)$, no flapping occurs and the only two regimes are the undeformed and deformed equilibria.

Chapter 8

NONLINEAR SIMULATIONS AND GLOBAL MODE ANALYSIS OF INVERTED FLAG FLAPPING

8.1 Simulation parameters

The results presented below use the nonlinear solver described in chapter 3 of part I and the global stability solver described in chapter 4 of part I.

The flow equations are treated using a multidomain approach: the finest grid surrounds the body and grids of increasing coarseness are used at progressively larger distances [16]. In all computations below, the domain size of the finest sub-domain was $[-0.2, 1.8]\times[-1.1, 1.1]$ and the total domain size was $[-15.04, 16.64]\times[-17.44, 17.44]$. The grid spacing on the finest domain was $h = 0.01$ and the grid spacing for the flag was $\Delta s = 0.02$. For computations involving time marching, the time step was $\Delta t = 0.001$, which gave a maximum Courant-Friedrichs-Levy number of ≈ 0.15.

To determine the suitability of these parameters, we performed a grid convergence study of the nonlinear solver using $Re = 200, M_\rho = 0.5, K_B = 0.35$. For these parameters the flag enters limit cycle flapping of fixed amplitude and frequency. Using the grid described above, the amplitude and frequency of these oscillations were $a = \pm 0.81$, $f = 0.180$, respectively. Refining the grid spacing to $h = 0.0075$ on the finest domain and increasing the domain such that the finest sub-domain size was $[-0.2, 2.8] \times [-1.5, 1.5]$ and the total domain size was $[-22.58, 25.18] \times [-23.88, 23.88]$ changed these values to $a = \pm 0.80$, $f = 0.183$, respectively.

8.2 Dynamics for $Re = 200$

We now consider the inverted-flag system for $Re = 200$. We demonstrate the existence of a deformed equilibrium that is stable over a small range of stiffnesses and becomes unstable as K_B is decreased. The transition to small-deflection deformed flapping associated with this decrease in K_B is shown through a global stability analysis to be a supercritical Hopf bifurcation of the deformed equilibrium. We next consider the large-amplitude flapping regime, and confirm the arguments of Sader et al. [71] that this regime is a VIV for small values of M_ρ – flapping and vortex shedding synchronize to a common frequency. This large-amplitude regime

is then shown to be qualitatively different for larger mass ratios, consistent with the scaling analysis of Sader et al. [71]. In this large-M_ρ case, flapping occurs at a lower frequency than vortex shedding, and similarities and differences to VIV are discussed. We then use a global stability analysis to confirm the argument of Shoele and Mittal [77] that small-amplitude flapping in the deflected-mode regime is driven by the bluff-body vortex-shedding instability. Finally, we show that for a range of K_B, light flags with $M_\rho \leq O(1)$ exhibit chaotic flapping characterized by switching between large-amplitude flapping and the deflected-mode state. No chaotic flapping is observed for heavy flags, *i.e.*, $M_\rho > O(1)$.

Bifurcation diagrams and general observations

Figure 8.1 shows bifurcation diagrams at four different masses for $Re = 200$. Each plot gives the transverse leading edge displacement (tip deflection, δ_{tip}, nondimensionalized by the flag length L) as a function of the reciprocal stiffness ($1/K_B$). Solid lines represent stable equilibria, and dashed lines correspond to unstable equilibria. Information for unsteady regimes is conveyed through the markers. A set of markers at a given stiffness corresponds to tip deflection values from a single nonlinear simulation at moments when the tip velocity is zero (*i.e.*, when the flag changes direction at the tip). From a dynamical systems perspective, the markers correspond to zero tip velocity Poincaré sections of a tip velocity-tip displacement phase portrait. All nonlinear simulations were started with the flag in its undeflected position and the flow impulsively started to its freestream value. A small body force was introduced at an early time to trigger any instabilities in the system. All simulations contain a minimum of 15 flapping cycles except for the chaotic flapping regime, where a minimum of 55 cycles were used. To avoid representing transient behavior in the figures, we omit the first several flapping cycles in the diagrams. The bifurcation diagrams were insensitive to starting conditions – the results were unchanged by running a corresponding set of simulations with the flag initialized in its deformed equilibrium state.

To illustrate the meaning of the markers in figure 8.1 further, consider $1/K_B \approx 4$ for $M_\rho = 0.5$. The system enters into large-amplitude limit cycle flapping with a fixed amplitude of $\approx \pm 0.8$, and the bifurcation diagram reflects this with a marker at these peak tip displacements, which are the only tip displacement values where the tip velocity is zero. Note that there are actually several markers superposed onto one another at this stiffness since multiple flapping periods were used to plot these diagrams, though only one marker is visible because of the limit cycle behavior

exhibited. As another example, the bifurcation diagram at $1/K_B \approx 6$ for $M_\rho = 0.05$ depicts chaotic flapping. Many markers are visible at this stiffness because the flag changes direction at several different values of δ_{tip}. The value of using zero tip-velocity Poincaré sections for the bifurcation diagrams is seen through chaotic flapping: these Poincaré sections demonstrate the variety of transverse locations where the flag changes direction – a fact not captured through, for example, plotting the peak-to-peak flapping amplitudes at a given stiffness.

The bifurcation diagrams in figure 8.1 depict the undeformed equilibrium (I), deformed equilibrium (II), small-deflection deformed flapping (III), large-amplitude flapping (IV), deflected mode (VI), and chaotic flapping (V) regimes. In small-deflection deformed flapping, flapping is seen about the upward deflected equilibrium. There is a corresponding deformed equilibrium with a negative flag deflection, and different initial conditions would result in flapping about this equilibrium. We refrain from plotting this behavior to avoid confusion with large-amplitude flapping.

The undeformed equilibrium becomes unstable with decreasing stiffness due to a divergence instability (the critical stiffness for instability is independent of the mass ratio) [32, 40, 71]. We see from figure 8.1 that this instability causes a transition to a regime where the flag is in a steady deflected position. As stiffness is decreased, this steady deflected state is characterized by increasingly large tip deflections (see figure 8.2). This regime was first observed by Gurugubelli and Jaiman [32] and Ryu et al. [69], and we note that it represents a deformed equilibrium state (*i.e.*, in the notation of section 8.1 it satisfies the steady state equations $r(y) = 0$). Moreover, even for masses where flapping occurs, the deformed equilibrium still exists as an unstable steady-state solution to the fully-coupled equations (4.1)–(4.4). Note also that for a given stiffness the tip deflection of the deformed equilibrium is constant for all masses, since the equilibrium is a steady state solution of (4.1)–(4.4) and therefore does not depend on flag inertia. Figure 8.2 provides illustrations of deformed equilibria for various stiffnesses (some of which are unstable).

Figure 8.3 gives the peak flapping frequency for the various regimes where flapping occurs. For all masses considered, small-deflection flapping is associated with a low frequency that is not indicative of VIV behavior: using the maximal tip displacement as the length scale, the largest Strouhal number over all masses is 0.02. We show in the next section that this regime is caused by the transition to instability of the leading global mode of the deformed equilibrium. Note that the frequency is dependent on flag mass in this regime, illustrating the fully-coupled nature of the problem.

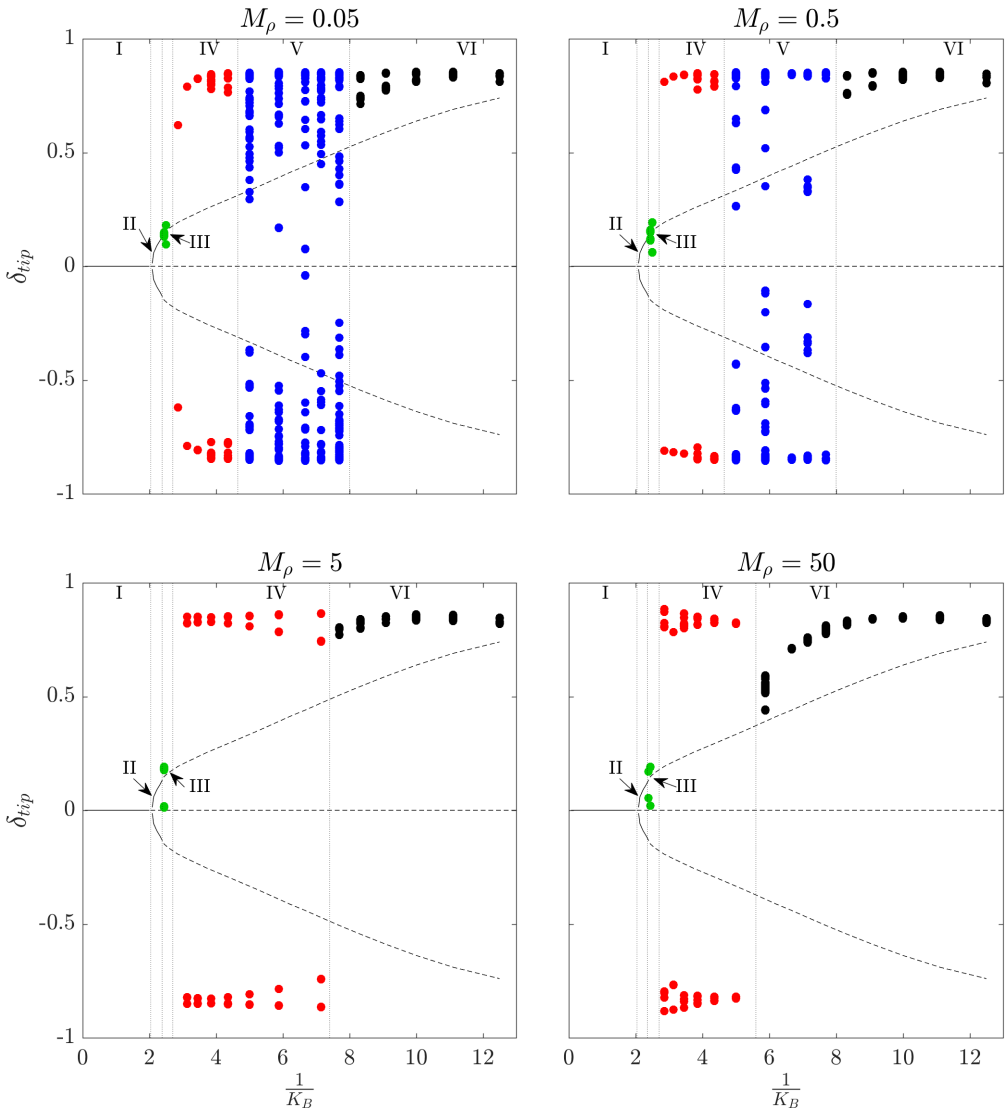

Figure 8.1: Bifurcation diagrams of inverted-flag dynamics at $Re = 200$ that show leading edge transverse displacement (tip deflection, δ_{tip}) versus inverse stiffness ($1/K_B$). I: undeformed equilibrium, II: deformed equilibrium, III: small-deflection deformed flapping, IV: large-amplitude flapping, V: chaotic flapping, VI: deflected mode. See the main text for a description of the various lines and markers and details on how the diagrams were constructed.

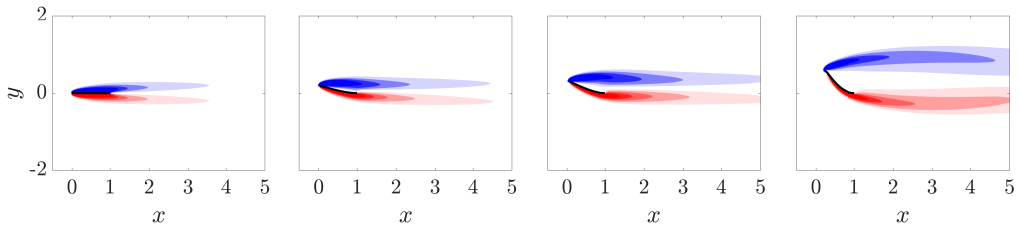

Figure 8.2: Vorticity contours for equilibrium states of the flow-inverted-flag system at $Re = 20$. From left to right: $K_B = 0.5, 0.35, 0.22, 0.11$. The three rightmost equilibria are unstable for all masses considered. Contours are in 18 increments from -5 to 5.

Large-amplitude flapping is qualitatively different for light flags ($M_\rho = 0.05, 0.5$) and heavy flags ($M_\rho = 5, 50$). *Light flags*: the flapping frequency is roughly constant across an order-of-magnitude change in M_ρ, which demonstrates the flow-driven nature of flapping in this regime. Sader et al. [71] found that for a range of parameters large-amplitude flapping exhibits several properties of a VIV, and we confirm below that for light flags the fluid forces on the flag and flag displacement oscillate at the same frequency to form a VIV. *Heavy flags*: the flapping frequency is decreased relative to light flags, and we show in a later section that this corresponds to additional shed vortices per flapping period. Thus, for heavy flags the fluid forces and flag displacements are associated with different dominant frequencies. This is consistent with the scaling analysis of Sader et al. [71], and we discuss similarities and differences to VIV in section 8.2.

For all masses, the deflected-mode regime (occurring at low stiffness/ high flow rate) has a peak frequency that matches the bluff-body shedding frequency (depicted by the dashed lines). This regime is therefore flow-driven and caused by the canonical bluff-body wake instability irrespective of flag mass [77]. We show in section 8.2 that the global stability analysis reflects this behavior.

Finally we note that for light flags ($M_\rho = 0.05, 0.5$), large-amplitude flapping bifurcates (with decreasing stiffness) to chaotic flapping before entering into the deflected-mode regime. The frequency plot for $M_\rho = 0.05, 0.5$ in figure 8.3 illustrates this transition further: in the large-amplitude flapping regime (region IV), decreasing stiffness leads to a corresponding decrease in flapping frequency. Eventually the decrease in frequency becomes significant enough that de-synchronization between flag flapping and vortex shedding occurs. At this point, chaotic flapping (region V) characterized by multiple frequencies ensues. The multiple frequencies in region V of figure 8.3 were obtained from a power-spectral density plot at each

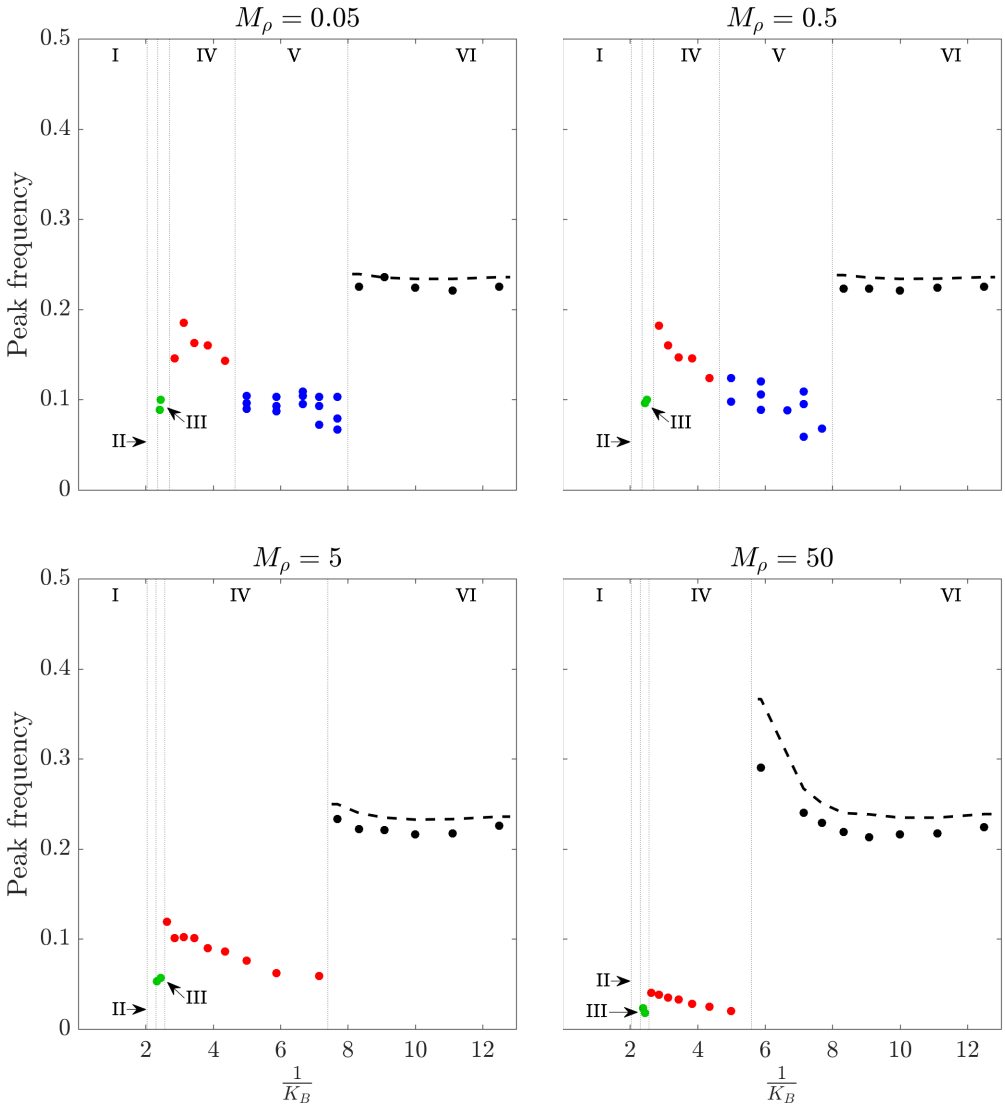

Figure 8.3: Markers: peak flapping frequency at $Re = 200$ for the parameters corresponding to the bifurcation diagrams shown in figure 8.1; (--): bluff-body shedding frequency ($= 0.2/L_p$, where L_p is the projected length of the flag to the flow defined using the maximum tip deflection at a given stiffness).

stiffness: frequencies accounting for at least 20% of the total spectral energy were plotted. The chaotic regime is discussed in more detail in section 8.2.

Small-deflection deformed flapping

Table 8.1 demonstrates that the bifurcation to small-deflection deformed flapping is a supercritical Hopf bifurcation of the deformed equilibrium. For all four mass ratios (M_ρ), the onset of flapping is associated with the transition to instability

M_ρ	K_B	Leading mode		Peak frequency of nonlinear simulation
		Growth rate	Frequency	
0.05	0.415	-0.0021	0.110	N/A (stable equilibrium)
0.05	0.41	0.0052	0.110	0.108
0.5	0.42	-0.0031	0.104	N/A (stable equilibrium)
0.5	0.415	0.0073	0.103	0.101
5	0.425	-0.0014	0.073	N/A (stable equilibrium)
5	0.42	0.0039	0.072	0.071
50	0.435	-0.0022	0.028	N/A (stable equilibrium)
50	0.43	0.0045	0.027	0.028

Table 8.1: Growth rate and frequency of the leading global mode of the deformed equilibrium compared with nonlinear behavior for parameters near the onset of small-deflection deformed flapping.

of the leading mode of the deformed equilibrium. Table 8.1 also shows that the leading mode accurately captures the flapping frequency observed in the nonlinear simulations near this stability boundary where flapping amplitudes remain small.

Figures 8.4 and 8.5 show the leading mode of the deformed equilibrium near the critical stiffness values where bifurcation occurs for $M = 0.5$ and $M = 5$, respectively. Flapping is associated with vortical structures isolated near the flag surface. Note that the vortical structures are longer for $M_\rho = 5$ (figure 8.5) than for $M_\rho = 0.5$ (figure 8.4), which is commensurate with the lower flapping frequency seen for the more massive case.

To demonstrate how the leading mode manifests itself in the nonlinear simulations, we show in figure 8.6 snapshots during a flapping period of a flag with $M_\rho = 0.5, K_B = 0.41$ (*i.e.*, in the small-deflection flapping regime). Note in particular the absence of vortex shedding – the entire flapping period is associated with long vortical structures that extend from the flag into the wake. This is distinct from the large-amplitude flapping behavior discussed in the next section, and emphasizes that even at the moderate Reynolds number of $Re = 200$, inverted flags have a flapping mechanism devoid of vortex shedding.

Large-amplitude flapping

Decreasing stiffness in the small-deflection deformed flapping regime is associated with an increasingly unstable leading mode (see table 8.2) and a corresponding increase in flapping amplitude. Eventually, the amplitude is sufficiently large for the flag to reach past the centerline ($\delta_{tip} = 0$) position, and large-amplitude flapping

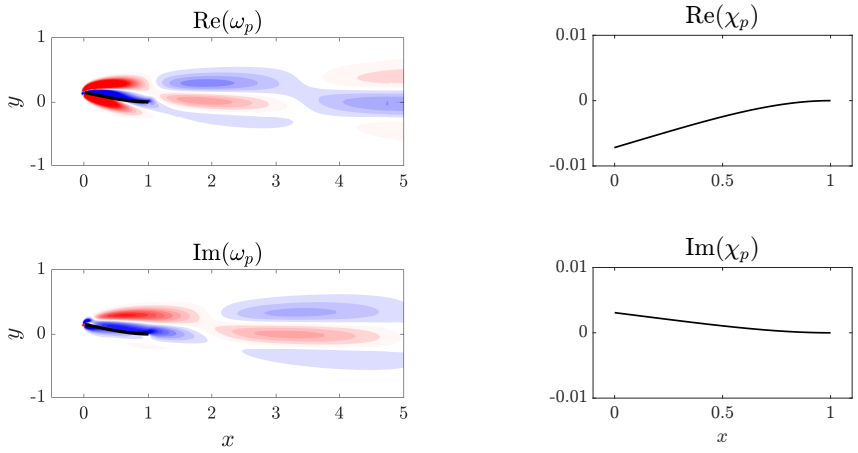

Figure 8.4: Real (top) and imaginary (bottom) parts of vorticity (left) and flag displacement (right) of the leading global mode of the deformed equilibrium for $M_\rho = 0.5, K_B = 0.41$ and $Re = 200$ (corresponding to small-deflection deformed flapping). Vorticity contours are in 20 increments from -0.05 to 0.05.

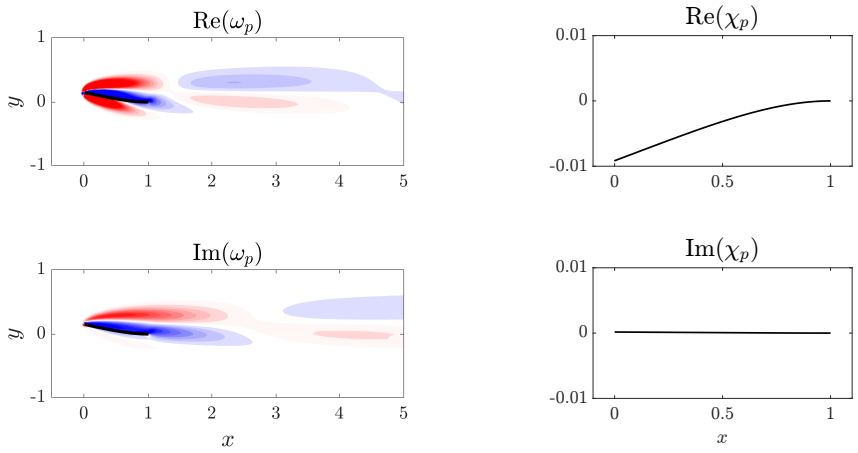

Figure 8.5: Real (top) and imaginary (bottom) parts of vorticity (left) and flag displacement (right) of the leading global mode of the deformed equilibrium for $M_\rho = 5, K_B = 0.41$ and $Re = 200$ (corresponding to small-deflection deformed flapping). Vorticity contours are in 20 increments from -0.2 to 0.2.

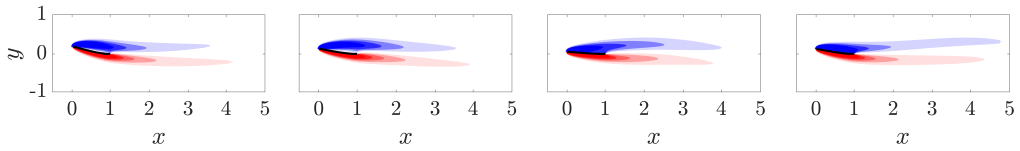

Figure 8.6: Vorticity contours at four snapshots of a flapping period of a flag in small-deflection deformed flapping. The figures were obtained from a nonlinear simulation with $Re = 200, M_\rho = 0.5, K_B = 0.41$. Contours are in 18 increments from -5 to 5.

K_B	Leading mode growth rate
0.41	0.022
0.38	0.123
0.35	0.250
0.33	0.313

Table 8.2: Growth rate of the leading global mode of the deformed equilibrium for $M_\rho = 0.5$ for stiffnesses in the small-deflection deformed flapping and large-amplitude flapping regimes.

ensues.

At this Reynolds number, the large-amplitude behavior is associated with sufficient bluffness to the flow that vortex shedding occurs. As discussed in section 8.2, the resulting dynamics are dependent on flag mass, and we therefore consider light flags and heavy flags separately in what follows.

We emphasize that in either the light- or heavy-flag case, vortex shedding interacts with intrinsic flapping behavior that can be understood through the deformed equilibria of the system. In large-amplitude flapping, the deformed equilibrium is unstable and has a sufficiently large saturation amplitude for the flag to flap past the centerline position and into the region of attraction of the deformed equilibrium on the other side of the centerline. This newly sampled deformed equilibrium is also associated with a saturation amplitude that leads the flag to flap past the centerline, so an indefinite process ensues with flapping occurring around these two equilibria. The existence of this intrinsic flapping mechanism is particularly pronounced at $Re = 20$ for large values of M_ρ, for which flapping occurs without vortex shedding (see section 8.3). This result attests to the presence of non-VIV flapping mechanisms and to the potential for large-amplitude flapping in the absence of any vortex shedding.

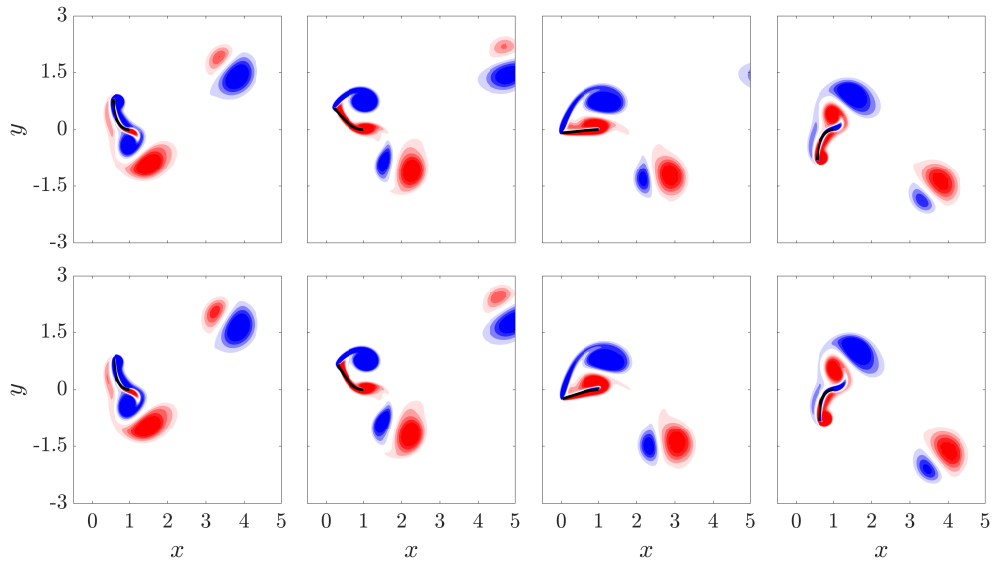

Figure 8.7: Vorticity contours at four snapshots of a flapping period of a flag in large-amplitude flapping for $M_\rho = 0.05$ (top row) and $M_\rho = 0.5$ (second row). The other parameters were $Re = 200, K_B = 0.32$. Contours are in 18 increments from -5 to 5.

Large-amplitude flapping of light flags

For sufficiently light flags ($M_\rho \leq 0.5$ in our studies), flapping was shown to synchronize with specific vortex-shedding patterns [32, 77], and Sader et al. [71] used experiments and a scaling analysis to argue that this regime is a VIV. To illustrate the synchronization of vortex shedding and flapping, we show snapshots from a half-period of large-amplitude flapping for $M_\rho = 0.05, 0.5$ in figure 8.7. Note that despite an order of magnitude change in mass, the vortex-shedding pattern in the top two rows of the figure is similar: when the flag reaches its peak amplitude the leading edge vortex formed during the upstroke grows (left plot); as the flag begins its downstroke the leading edge vortex is released and a trailing edge vortex forms (second from left plot); the vortices grow in size as the flag reaches its centerline position (second from right plot); while the leading and trailing edge vortices advect downstream to form a P vortex pair (see Williamson and Roshko [89] for a description of this vortex characterization), a leading edge vortex forms as the flag continues its downstroke (rightmost plot). When the flag reaches its peak position, an analogous process to the one just described occurs during the upstroke (with oppositely signed vorticity).

To confirm that this regime is a VIV, we show in figure 8.8 time traces of the coef-

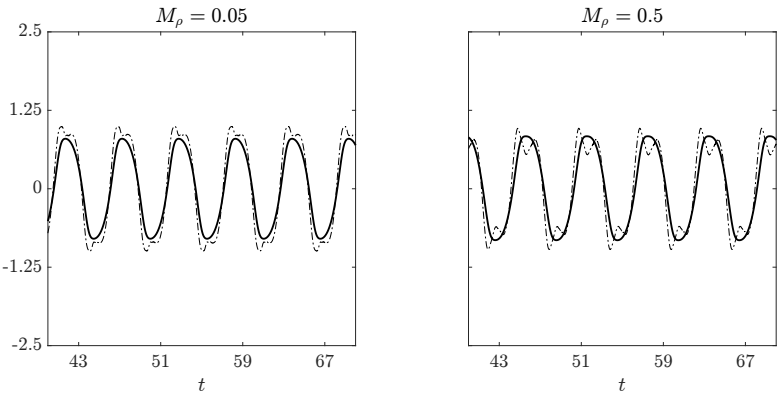

Figure 8.8: Tip displacement (−) and coefficient of lift (·−) for an inverted flag in large-amplitude flapping with $Re = 200$, $K_B = 0.32$.

ficient of lift and tip displacement for $M_\rho = 0.05, 0.5$. The lift and tip displacement are synchronized and share a common dominant frequency, and therefore satisfy the definition of VIV [39, 72].

Large-amplitude flapping of heavy flags

The interaction between vortex shedding and flapping is qualitatively different as the flag mass is increased further. Figure 8.9 shows that for $M_\rho = 5, 50$ additional vortices are shed per half-period. The flapping cycle for $M_\rho = 5$ is similar to the lighter flag cases, except that during the downstroke an additional leading edge vortex forms (first row, second from rightmost plot) and advects downstream along with the original leading and trailing edge vortices (rightmost plot). The additional vortex leads to a P + S wake structure. For $M_\rho = 50$, even more vortices are shed during the downstroke: the first leading and trailing edge vortices are shed when the flag is still near its peak amplitude (second row, leftmost plot); the flag begins its downstroke and another leading-trailing edge vortex pair are formed (second from leftmost plot); as the flag nears its centerline position, a third leading edge vortex forms (second from rightmost plot); this leading edge vortex combines with a newly formed trailing edge vortex during the downstroke phase to form a third pair that is advected downstream; at the end of the downstroke phase, new vortices form at the leading and trailing edge as the flag reaches its peak amplitude (rightmost plot).

The different frequency behavior of flapping and vortex shedding is illustrated further through time traces of the coefficient of lift and tip displacement (see figure 8.10). Unlike in the light-flag case, heavy flags contain multiple lift peaks for a given peak in tip displacement. Moreover, for $M_\rho = 50$, there is a slight departure from

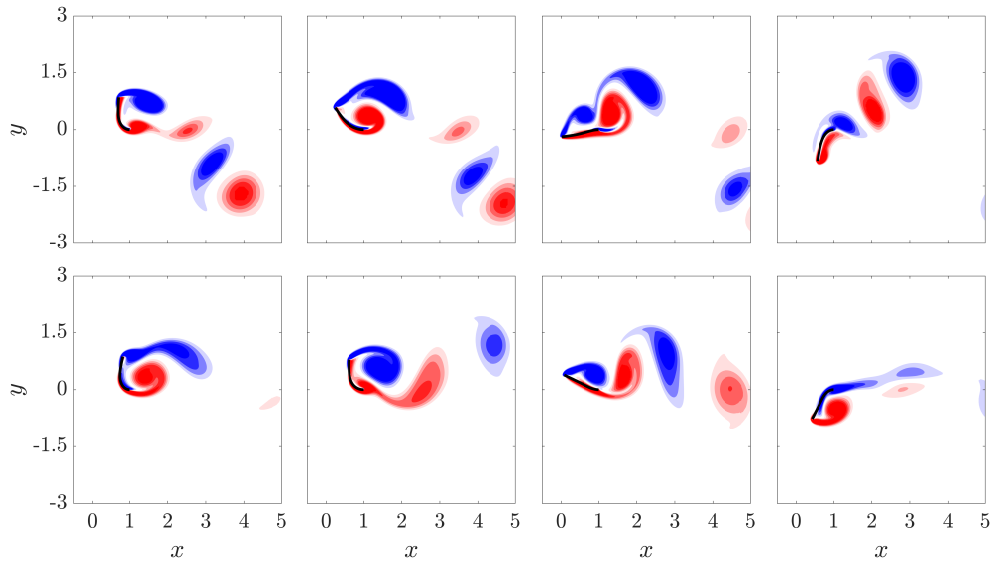

Figure 8.9: Vorticity contours at four snapshots of a flapping period of a flag in large-amplitude flapping for $M_\rho = 5$ (first row) and $M_\rho = 50$ (second row). The other parameters were $Re = 200, K_B = 0.32$. Contours are in 18 increments from -5 to 5.

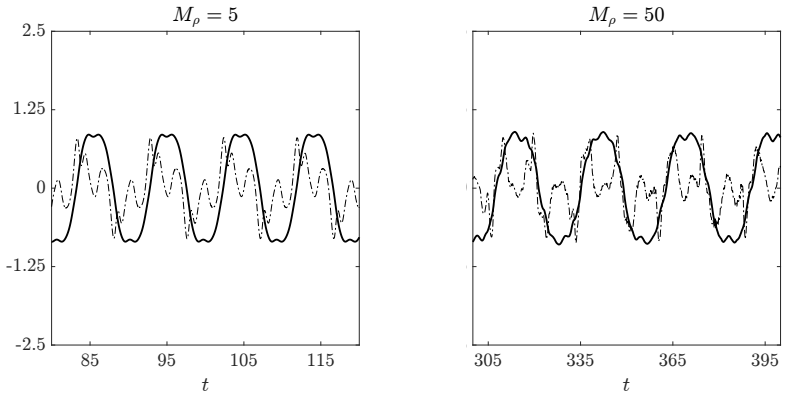

Figure 8.10: Tip displacement (−) and coefficient of lift (·−) for an inverted flag in large-amplitude flapping with $Re = 200$, $K_B = 0.32$.

periodicity that can be observed in figure 8.10 (and is reflected in the bottom right bifurcation diagram in figure 8.1). The disparity between the dominant frequency of the coefficient of lift and tip displacement is reflective of a break from canonical-VIV behavior, and is consistent with the scaling analysis of Sader et al. [71] that VIV should cease for sufficiently large M_ρ.

Yet, similarities to VIV persist for large values of M_ρ. For $M_\rho = 5$, it is clear from figure 8.10 that the lift coefficient is periodic over a period of flapping, and thus the

large-amplitude response could be a result of synchronization between flapping and a higher harmonic in the vortex-shedding response of the fluid. This relation between the dominant flapping motion and a harmonic response in the fluid could also be occurring for $M_\rho = 50$, though the slight aperiodicity in the system emphasizes the continued departure from canonical VIV behavior with increasing mass ratio.

Deflected-mode regime

For low stiffnesses the system transitions to a large-deflection state about which small-amplitude flapping occurs. As seen in figure 8.1, this flapping is not centered about the deformed equilibrium position (*i.e.*, the mean and equilibrium states are different).

The nature of flapping in this regime is qualitatively distinct from that of small-deflection deformed flapping and large-amplitude flapping. Shoele and Mittal [77] observed that when the flapping frequency is scaled by the freestream velocity and mean tip amplitude (*i.e.*, the mean projected length to the flow), it agrees well with the classical 0.2 value found for vortex shedding past bluff bodies [66]. They used this finding to argue that the bluff-body wake instability is responsible for the small-amplitude flapping in this regime.

The global stability analysis of the deformed equilibrium confirms this previous conclusion. Figure 8.11 shows that the least damped mode is characterized by a vortical structure in the wake of the flag similar to the leading mode of a rigid stationary cylinder [5]. This is in contrast to the leading mode found for small-deflection deformed flapping and large-amplitude flapping, which has isolated vortical structures near the flag surface[1]. Moreover, as seen in table 8.3, the flapping frequency of this leading mode is independent of mass ratio (M_ρ). This is also distinct from the mass-dependent flapping frequency of the least damped mode for the previously discussed regimes. The similar vortical structure of the mode to other bluff-body flows and the independence of the structural parameters on the modal frequency demonstrate that the leading instability is associated with vortex shedding and is flow-driven.

The presence of vortex shedding in this deflected-mode regime is also the cause of the difference between the mean and equilibrium flapping positions. Vortex shedding is associated with an increase in the mean forces on the flag compared

[1]The analogous mode to the leading global mode for small-deflection deformed flapping and large-amplitude flapping is also unstable in the deflected-mode regime, but is associated with a smaller growth rate.

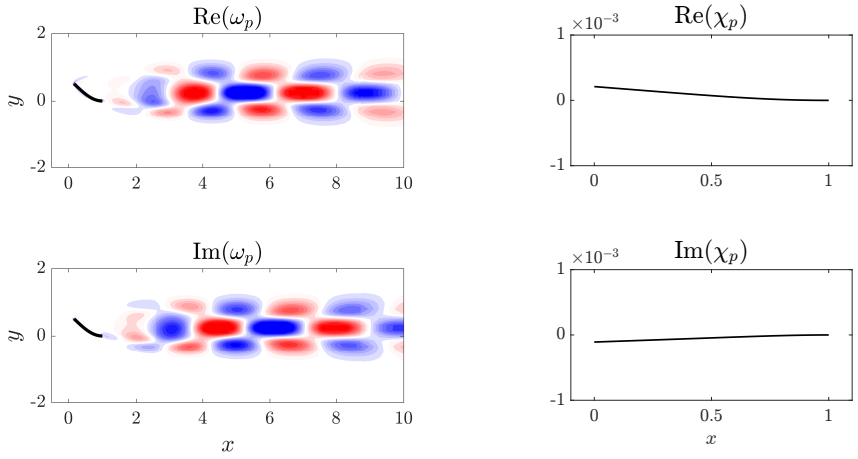

Figure 8.11: Real (top) and imaginary (bottom) parts of vorticity (left) and flag displacement (right) of the leading global mode of the deformed equilibrium for $M_\rho = 0.5, K_B = 0.12$ and $Re = 200$. Vorticity contours are in 20 increments from -0.2 to 0.2. The eigenvectors are identical for $M_\rho = 0.05, 0.5$, and 50.

M_ρ	Leading mode frequency
0.05	0.205
0.5	0.205
5	0.205
50	0.205

Table 8.3: Frequency of the leading global mode of the deformed equilibrium for $K_B = 0.12$ and four different masses. All cases correspond to the deflected-mode regime.

with the equilibrium state (which is devoid of vortex shedding; *c.f.*, figure 8.2). To demonstrate this increase in fluid forces, we ran a simulation with the flag fixed in the deformed equilibrium position corresponding to $K_B = 0.1$. With the flag fixed in this position, the bluffness of the body causes the flow to enter limit-cycle vortex shedding with a mean lift and drag of 0.356 and 0.583, respectively. By contrast, when the fully-coupled system is in the deformed equilibrium and vortex shedding is absent, the lift and drag forces are 0.192 and 0.344, respectively. The increase in mean forces causes a corresponding increase in flag deflection, and thus in the nonlinear simulations flapping occurs about a mean position that is raised from the equilibrium state.

We emphasize that this vortex shedding mode is stable for small-deflection deformed flapping and large-amplitude flapping found at higher stiffnesses (and studied in the

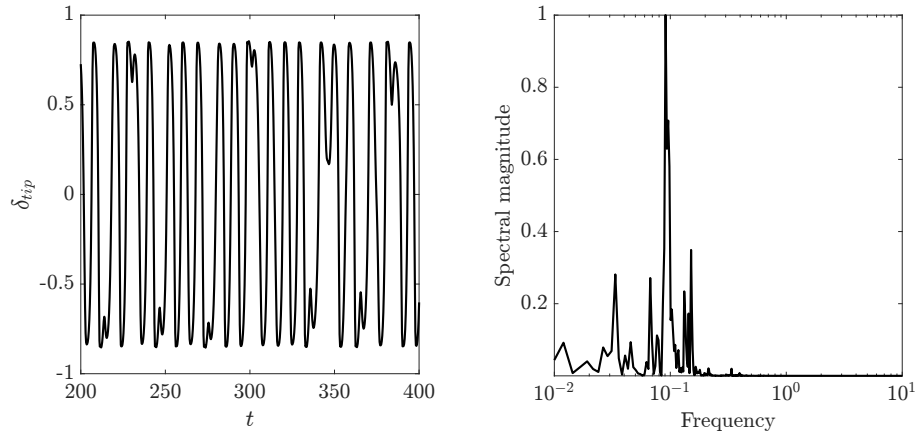

Figure 8.12: Tip displacement as a function of time (left) and spectral density of tip displacement (right) for a flag in the chaotic flapping regime, with $M_\rho = 0.05$, $K_B = 0.17$, $Re = 200$. The left plot shows a zoomed in version of the total time window used for the spectral density computation, $t \in [20, 500]$.

previous sections). For example, the growth rate of the vortex shedding mode for the large-amplitude flapping parameters $K_B = 0.2$, $M_\rho = 0.5$ is -0.392. The vortex-shedding mode is therefore not the cause of instability of the deformed equilibrium in those regimes.

Chaotic flapping

For sufficiently light flags ($M_\rho \leq 0.5$ in our studies), large-amplitude flapping (region IV in the bifurcation diagrams of figure 8.1) bifurcates to chaotic flapping (region V) before entering into deflected-mode flapping (region VI). Figure 8.12 shows that the time trace of the tip displacement is aperiodic and associated with broadband frequency content.

To demonstrate mathematically that this behavior is chaotic, we compute the Lyapunov exponent of the system using the time-delay method of Wolf et al. [90] (this approach was also used by Connell and Yue [17] to identify chaotic flapping of conventional flags). The method computes an approximation of the distance in time, $d(t)$, of two trajectories starting close to one another at an initial time t_0. The evolution of this distance is written as

$$d(t) = d(t_0)e^{\gamma(t-t_0)} \tag{8.1}$$

where γ is the Lyapunov exponent that represents the departure or convergence of the two trajectories. A zero value of γ corresponds to a stationary state where the system is in limit cycle behavior; a positive value of γ corresponds to divergence of the two

M_ρ	K_B	Lyapunov exponent (γ)	Flapping regime
0.05	0.35	-0.0012	Large-amplitude flapping (region IV)
0.05	0.17	0.068	Chaotic flapping (region V)
0.05	0.08	-0.0023	Deflected-mode (region VI)
0.5	0.35	-0.0015	Large-amplitude flapping (region IV)
0.5	0.17	0.059	Chaotic flapping (region V)
0.5	0.08	0.0009	Deflected-mode (region VI)

Table 8.4: Lyapunov exponents for different flapping regimes. For each regime, the corresponding region from the bifurcation diagram of figure 8.1 is indicated in parentheses.

trajectories, and thus to chaotic flapping. Table 8.4 shows the Lyapunov exponent computed for various values of M_ρ and K_B. For large-amplitude and deflected-mode flapping, the exponent is approximately zero, coincident with limit-cycle flapping. In the chaotic regime that occurs at stiffnesses between large-amplitude and deflected-mode flapping, the exponent is positive and larger by an order of magnitude, indicative of a transition to chaotic behavior in this regime.

The bifurcation diagrams in figure 8.1 demonstrate that increasing mass reduces the chaotic behavior. In moving from $M_\rho = 0.05$ to $M_\rho = 0.5$, there were certain stiffnesses within the chaotic flapping regime that exhibited periodic flapping instead of chaotic flapping (see figure 8.1). We believe that this is an artifact of only running the simulations for finite time, but the absence of chaotic flapping over a minimum of 55 flapping periods for certain stiffnesses at $M_\rho = 0.5$ speaks to the effect of increasing inertia on reducing the chaotic behavior. For the heavier flag cases of $M_\rho = 5, 50$, chaotic flapping disappears altogether. Thus, chaotic flapping is only associated with mass ratios (M_ρ) for which VIV flapping occurs.

To elucidate the nature of chaotic flapping, we show in figure 8.13 phase portraits of tip velocity versus tip displacement for inverted flags in the large-amplitude flapping, chaotic flapping, and deflected-mode regimes. The figures demonstrate that the chaotic flapping phase portrait contains both the large periodic orbit of large-amplitude flapping and the small-amplitude large-deflection periodic orbit of deflected-mode flapping. Thus, chaotic flapping is a regime in which large-amplitude flapping and the deflected mode hybridize to form a new strange attractor involving both states. The chaotic nature of the regime is associated with the apparent randomness in switching between these two orbits.

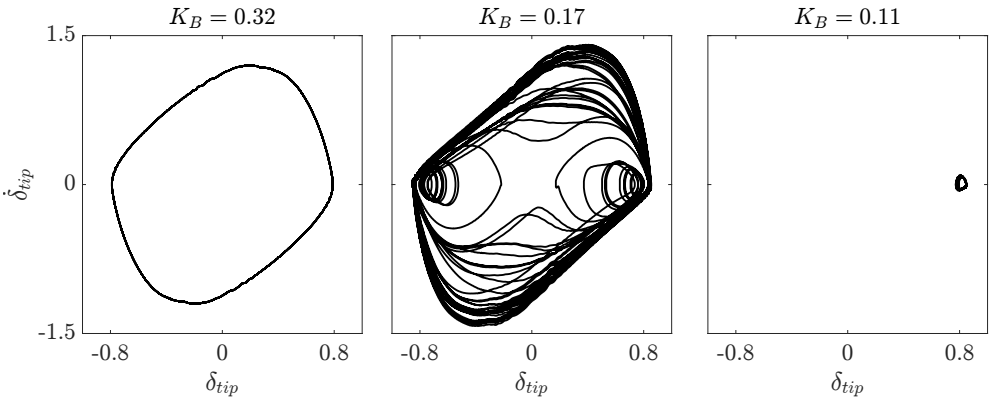

Figure 8.13: Tip velocity-tip displacement phase portraits for $M_\rho = 0.05$ and $K_B = 0.32$ (left), $K_B = 0.17$ (middle), and $K_B = 0.11$ (right).

8.3 Dynamics for $Re = 20$

Previous numerical simulations of Ryu et al. [69] demonstrated the absence of flapping for flags with $M_\rho \leq O(1)$ and $Re < 50$. We now consider $Re = 20$ to investigate the stability and dynamics of the inverted-flag system below this previously identified critical Reynolds number. In agreement with Ryu et al. [69], we find that light flags with $M_\rho = 0.05, 0.5$ do not flap. Heavy flags with $M_\rho = 5, 50$ are shown to undergo both small-deflection deformed flapping and large-amplitude flapping. Such behavior has yet to be reported, and we demonstrate that for this heavy flag case neither flapping regime is a VIV. As was observed for $Re = 200$, small-deflection flapping is caused by a supercritical Hopf bifurcation of the deformed equilibrium associated with the transition to instability of the least damped mode of the deformed equilibrium. Large-amplitude flapping is characterized by an increase in saturation amplitude of small-deflection flapping until eventually the flag swings past the centerline and begins a process where it samples both deflected equilibria. Finally, we show that at this low Reynolds number the deflected-mode state is not associated with flapping, and is instead a formal stable equilibrium of the fully-coupled system.

Bifurcation diagrams and general observations

Figure 8.14 gives bifurcation diagrams of the inverted-flag system at four different masses. These figures were plotted as described in section 8.2. The bifurcation diagrams reveal four distinct regimes: a stable undeformed equilibrium (I), a stable deformed equilibrium (II), small-deflection deformed flapping (III), and large-amplitude flapping (IV).

While many of the same bifurcations found at $Re = 200$ remain for $Re = 20$, there are also distinctions between them that are visible through the bifurcation diagrams. First, flapping does not occur for all masses considered at this lower Reynolds number, which demonstrates the stabilizing effect of fluid diffusion for inverted-flag dynamics. Second, the deflected-mode state no longer corresponds to flapping at this lower Reynolds number, and is instead a formal stable equilibrium of the fully-coupled fluid-structure equations of motion. Finally, chaotic flapping does not occur for any of the considered values of M_ρ at this lower Reynolds number.

As was seen for $Re = 200$, the divergence instability of the undeformed equilibrium (caused by decreasing K_B) leads to a stable deformed equilibrium that is independent of the mass ratio, M_ρ. This follows from the fact that the deformed equilibria are steady state solutions and therefore do not depend on flag inertia.

As stiffness is decreased, light flags remain in this deformed equilibrium regime – no flapping occurs at this Reynolds number for $M_\rho = 0.05, 0.5$. Moreover, since the equilibrium states do not depend on flag inertia, their bifurcation diagrams are identical. By contrast, with decreasing stiffness heavy flags transitioned from the deformed equilibrium to (respectively) small-deflection flapping and large-amplitude flapping before returning at even lower stiffnesses to a stable deformed equilibrium. To demonstrate the non-VIV nature of flapping at this low Reynolds number, we show in figure 8.16 the peak flapping frequency for the parameters corresponding to the bifurcation diagrams in figure 8.14. For all cases, the flapping frequency from the nonlinear simulations (denoted by the markers) is substantially different from the bluff-body vortex-shedding frequency. In the remainder of this section we explore the physical mechanisms behind the various regimes and the transitions between them.

Small-deflection deformed flapping

We show in table 8.5 that the transition from the deformed equilibrium to small-deflection deformed flapping is associated with the least damped global mode of the deformed equilibrium becoming unstable. Thus, as was seen for $Re = 200$, small-deflection deformed flapping is a supercritical Hopf bifurcation of the deformed equilibrium state. Table 8.5 also shows that the corresponding eigenvalue accurately predicts the flapping frequency of the nonlinear simulations near the stability boundary.

To illustrate the vortical structures and flag shapes associated with the instability

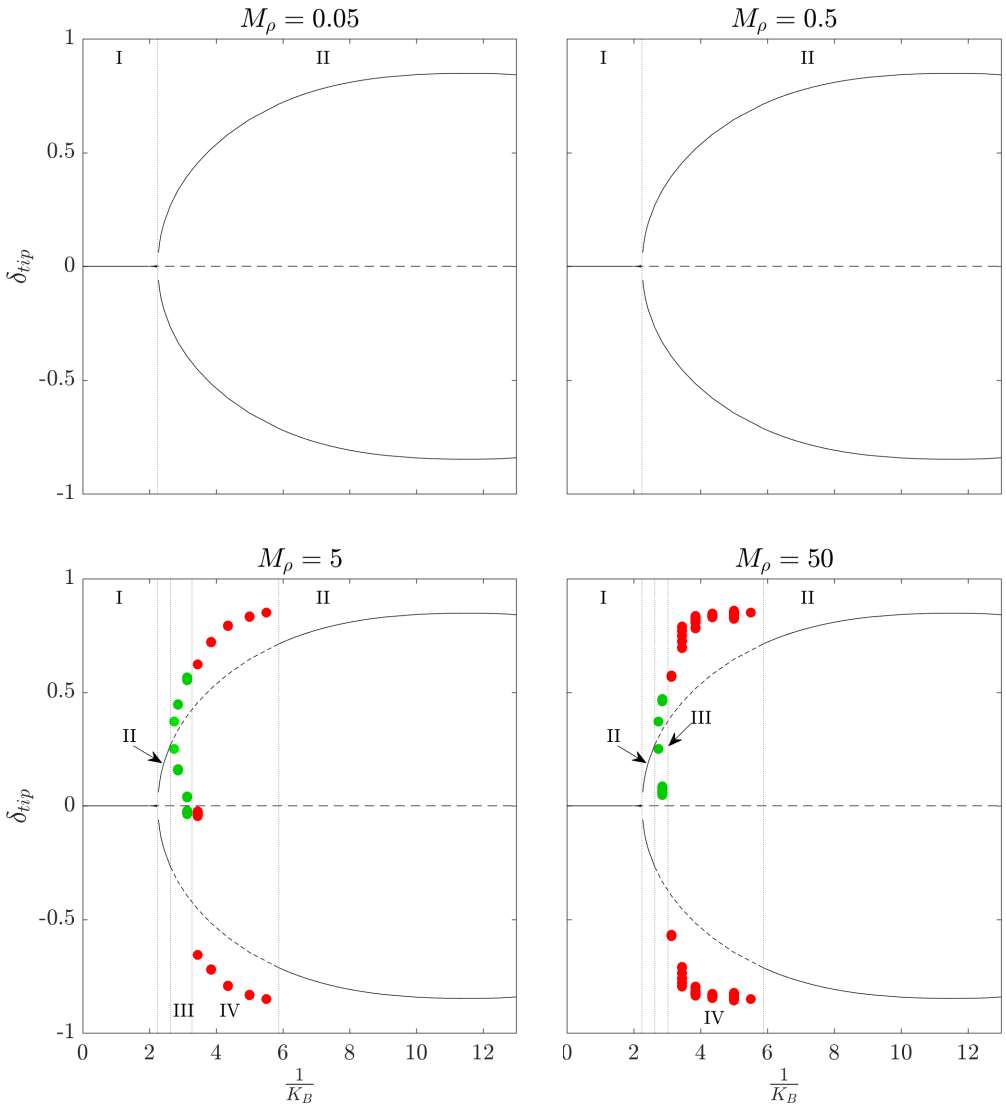

Figure 8.14: Bifurcation diagrams of inverted-flag dynamics at $Re = 20$ that show leading edge transverse displacement (tip deflection, δ_{tip}) versus inverse stiffness ($1/K_B$). I: undeformed equilibrium, II: deformed equilibrium, III: small-deflection deformed flapping, IV: large-amplitude flapping. See the main text for a description of the various lines and markers and details on how the diagrams were constructed.

M_ρ	K_B	Leading mode		Peak frequency of nonlinear simulation
		Growth rate	Frequency	
5	0.374	-0.0061	0.083	N/A (stable equilibrium)
5	0.371	0.0039	0.082	0.080
50	0.40	-0.003	0.031	N/A (stable equilibrium)
50	0.397	0.001	0.030	0.030

Table 8.5: Growth rate and frequency of the leading global mode of the deformed equilibrium compared with nonlinear behavior for parameters near the onset of small-deflection deformed flapping.

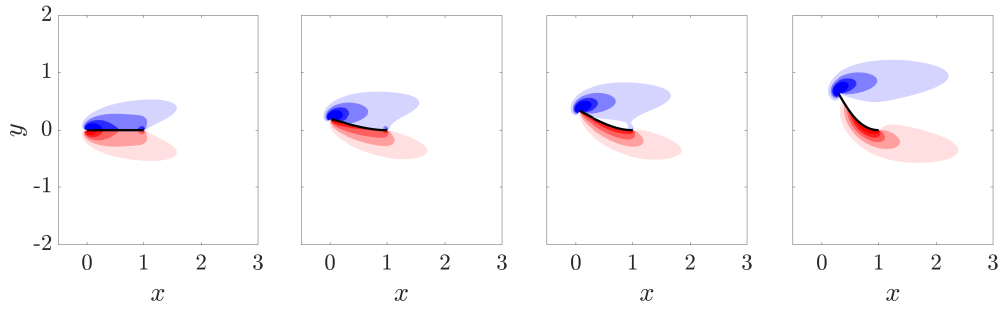

Figure 8.15: Vorticity contours for equilibrium states of the inverted-flag system at $Re = 20$. From left to right: $K_B = 0.5, 0.41, 0.35, 0.2$. The two rightmost equilibria are unstable for $M_\rho = 5, 50$. Contours are in 18 increments from -5 to 5.

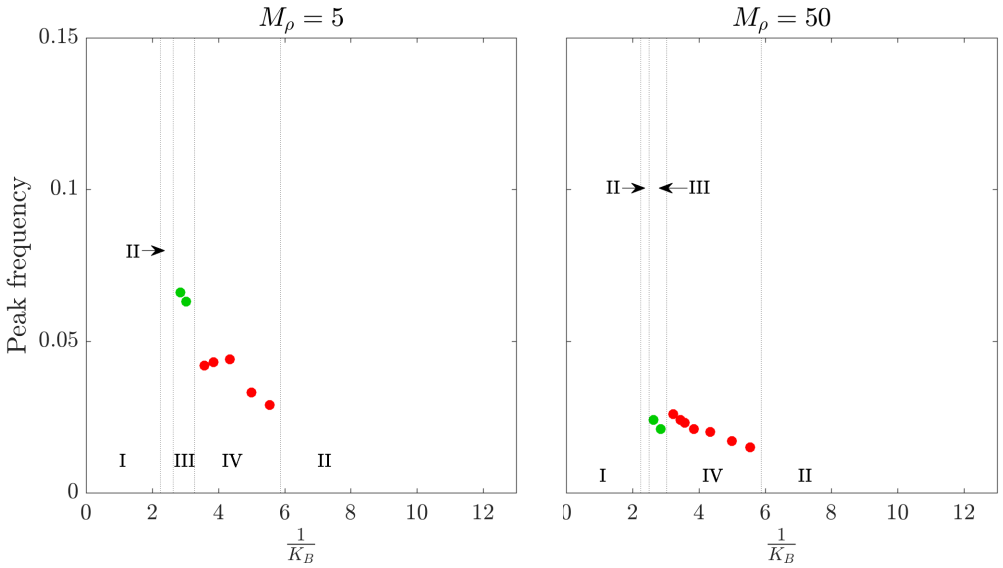

Figure 8.16: Markers: peak flapping frequency at $Re = 20$ for the parameters corresponding to the bifurcation diagrams shown in figure 8.14.

mechanism at this lower Reynolds number, we plot the real and imaginary parts of the leading global mode near the critical stiffness for $M_\rho = 5$ in figure 8.17 (the plot is similar for $M_\rho = 50$). Flag motion is associated with four vortical structures isolated near the flag surface.

We emphasize that a linear stability analysis of the undeformed equilibrium state is associated with a zero-frequency (non-flapping) unstable mode, and therefore does not capture the flapping behavior observed in the nonlinear simulations. This demonstrates that the divergence instability derived by Sader et al. [71] for inviscid fluids persists at lower Reynolds numbers.

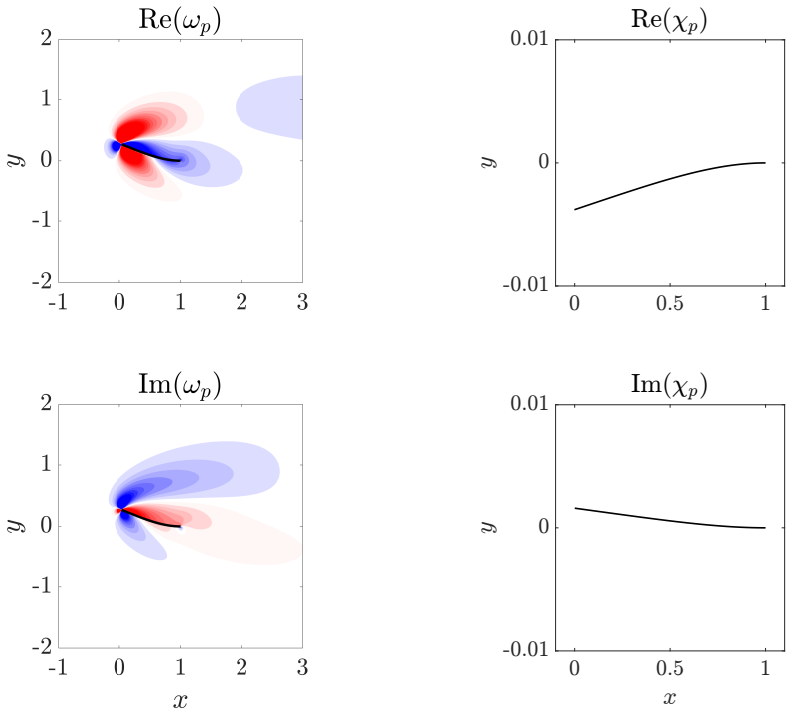

Figure 8.17: Real (top) and imaginary (bottom) parts of vorticity (left) and flag displacement (right) of the leading global mode of the deformed equilibrium for $M_\rho = 5, K_B = 0.37$ and $Re = 20$. Vorticity contours are in 20 increments from -0.05 to 0.05.

Figure 8.18 shows the leading global mode of the undeformed equilibrium. The mode has a similar flag shape and set of vortical structures to the real part of the leading mode of the deformed equilibrium. A noticeable distinction between the two, however, is that the vortical structures of the undeformed equilibrium mode are symmetric about the equilibrium flag position while those of the deformed equilibrium mode are not. The presence of asymmetry associated with flapping is indicative of the interplay between fluid forces, flag inertia, and internal flag stresses necessary to sustain flapping. To explore this interplay, consider a perturbation of the deformed equilibrium that sets the flag into motion in the direction of increasing deflection. This causes an increase in internal flag stresses that act to restore the flag to its deformed equilibrium. These stresses are opposed by the flag inertia and by forces from the oncoming fluid, which tend to destabilize the system further away from its deformed equilibrium. By contrast, if the flag is set into motion the other direction (towards the undeformed state), the fluid forces act to restore the flag to its deformed equilibrium and the flag inertia and internal flag stresses act as destabilizing forces. The exchange of internal flag stresses and fluid forces as

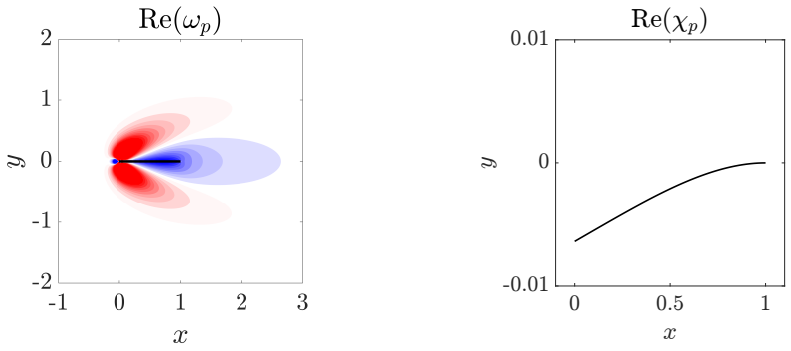

Figure 8.18: Real part of vorticity (left) and flag displacement (right) of the leading global mode of the undeformed equilibrium for $M_\rho = 5, K_B = 0.37$ and $Re = 20$. Vorticity contours are in 20 increments from -0.05 to 0.05.

destabilizing quantities is a unique feature of flapping about the deflected state – an analogous perturbation to a flag in the undeformed equilibrium results in flag stresses that are always restoring and fluid forces that are always destabilizing.

Large-amplitude flapping

We now consider the transition from small-deflection deformed flapping to large-amplitude flapping. Within the small-deflection deformed flapping regime, the bifurcation diagrams show that decreasing stiffness causes an increase in flapping amplitude. This is associated with an increase in growth rate of the leading mode (see table 8.6). The mechanism through which the increasingly unstable leading mode develops into large-amplitude flapping is similar to what was discussed for heavy flags at $Re = 200$. Eventually, the growth in saturation amplitude leads the flag to deform past the centerline position and into the region of attraction of the deformed equilibrium on the other side of the centerline. This newly sampled deformed equilibrium is also associated with a saturation amplitude that leads the flag to flap past the centerline, and indefinite flapping occurs around these two equilibria. We emphasize that at this low Reynolds number, vortex shedding does not occur, and the flapping frequency from figure 8.16 demonstrates that flapping is not a VIV in this regime. The nonlinear behavior characterized by flapping around the two unstable deformed equilibria provides the necessary non-VIV flapping mechanism.

We note that this non-VIV flapping mechanism is distinct from what is observed in large-amplitude oscillations of elastically mounted cylinders at subcritical Reynolds numbers. In the elastically mounted cylinder case, Mittal and Iaccarino [56] showed through nonlinear simulations and a global stability analysis that VIV persists at sub-critical Reynolds numbers for certain parameters, and that large-amplitude vibrations

K_B	Leading mode growth rate
0.37	0.008
0.35	0.039
0.32	0.120
0.29	0.342

Table 8.6: Growth rate of the leading global mode of the deformed equilibrium for $M_\rho = 5$ for stiffnesses in the small-deflection deformed flapping and large-amplitude flapping regimes.

are a result of this VIV. They moreover demonstrated that for these parameters the vibration frequency matched the bluff-body shedding frequency. By contrast, in the case of large-amplitude inverted-flag flapping, the flapping frequency is substantially smaller than the bluff-body vortex-shedding frequency.

Large-deflection equilibrium (deflected-mode regime)

A continued decrease in stiffness leads to a bifurcation from large-amplitude flapping back to a stable deformed equilibrium with large deflection. This transition corresponds to the re-stabilization of the leading global mode (*e.g.*, for $M_\rho = 5$, $K_B = 0.17$ the growth rate of the leading mode is -0.032). Note that this deflected-mode state is distinct from that found at higher Reynolds numbers, where the flag undergoes small-amplitude oscillations driven by vortex shedding [71, 77]. Since vortex shedding is absent at $Re = 20$, the deflected-mode regime is a formal equilibrium of the fully-coupled equations of motion.

8.4 Conclusions

We used 2D high-fidelity nonlinear simulations and a global linear stability analysis of inverted-flag flapping to (i) investigate the physical mechanisms responsible for the onset of flapping, (ii) study the role of vortex shedding in large-amplitude flapping, and (iii) further characterize various regime bifurcations that were previously identified and explored [32, 40, 69, 71, 77]. We performed studies at $Re = 20$ and 200 for a wide range of K_B and over a four-order-of-magnitude range of M_ρ. For $Re = 20$ and $M_\rho \leq O(1)$, no flapping occurs and the flag transitions with decreasing stiffness from an undeformed equilibrium to a deformed equilibrium. For all other combinations of Re and M_ρ considered, with decreasing flag stiffness the system transitions from a stable undeformed equilibrium to a stable deflected equilibrium via a divergence instability, to an unstable deformed equilibrium through a supercritical Hopf bifurcation that exhibits small-amplitude flapping, to large-amplitude

flapping, and finally to a deflected-mode state. Below we summarize the key features of each of these regimes.

Stable deflected equilibrium: we demonstrated that for all parameters considered the stationary deflected state identified by Gurugubelli and Jaiman [32] and Ryu et al. [69] is a formal equilibrium of the fully-coupled equations, and that even when flapping occurs this equilibrium persists as an unstable steady-state. A similar deformed equilibrium was found at $Re = O(30,000)$ by Sader et al. [71] through the addition of damping; establishing similarities between these findings is an area for future work.

Small-deflection deformed flapping: the deformed equilibrium becomes unstable and transitions to small-deflection deformed flapping with decreasing stiffness (K_B). This occurred at $Re = 200$ for all mass ratios considered and at $Re = 20$ for heavy flags ($M_\rho > O(1)$). This transition was shown to be initiated by a supercritical Hopf bifurcation of the deformed equilibrium state (i.e. a complex-conjugate set of eigenvectors becomes unstable). For all parameters that exhibited this small-deflection flapping regime, the leading mode and ensuing nonlinear behavior are both devoid of vortex shedding and have a flapping frequency that is not commensurate with a VIV.

Large-amplitude flapping: light flags ($M_\rho < O(1)$) at $Re = 200$ exhibit VIV behavior in which the fluid forces on the flag oscillate with the same dominant frequency exhibited by the flag. This coincides with the arguments of Sader et al. [71] based on experimental measurements and a scaling analysis. By contrast, heavy flags ($M_\rho > O(1)$) flap at a lower frequency and additional vortices are shed per flapping cycle – also consistent with the scaling analysis of Sader et al. [71]. This behavior is distinct from canonical VIV, but could be reflective of synchronization between flapping motion and a higher-harmonic response in the fluid. We also showed that large-amplitude flapping occurs for heavy flags at $Re = 20$, which highlights the existence of an intrinsic flapping mechanism even in the absence of vortex shedding. No flapping was observed for flags with $M_\rho < O(1)$ at $Re = 20$, which is in agreement with the simulations of Ryu et al. [69].

Deflected-mode: for $Re = 200$ we used a global stability analysis to confirm the argument of Shoele and Mittal [77] that this regime is driven by the canonical bluff-body wake instability. For all masses considered, the leading mode has vortical structures similar to the leading global mode found in canonical bluff-bodies [5] and a flapping frequency commensurate with the $St \sim 0.2$ bluff-body scaling [66]. We

then showed that the deflected mode does not exhibit any flapping at any mass ratio for $Re = 20$, and the system is instead in a large-deflection equilibrium state.

Chaotic flapping: we identified chaotic flapping for light flags at $Re = 200$ and characterized this regime by switching between large-amplitude flapping and the deflected-mode regime. No chaotic flapping was observed at $Re = 200$ for $M_\rho > O(1)$ or at $Re = 20$ for any of the mass ratios considered.

These findings demonstrate a wide range of physical mechanisms that drive the various dynamical regimes of the inverted flag system. Moreover, they highlight that the system dynamics depend on both the Reynolds number and mass ratio. At the same time, these results motivate future work that compares our low-to-moderate Reynolds number computational findings with results at higher Reynolds numbers and in three dimensions.

Chapter 9

OUTLOOK

In part II we built on previous studies to further characterize and understand inverted flag flapping. Yet, there remain unanswered questions and opportunities for further study. First, the inverted flag system depends on the Reynolds number and mass and stiffness ratios, but previous work has primarily focused on the effect of the stiffness ratio. We provided some observations about the effect of mass ratio and Reynolds number on the resulting physical regimes and associated physical mechanisms, but further studies into the effect of these parameters is warranted. Along these lines, simulations and experiments are being conducted at disparate Reynolds numbers (by orders of magnitude), and further characterizing the similarities and differences among them would aid in understanding its effect.

There are also open questions about three-dimensional (3D) effects on the system. Experiments at high Reynolds numbers of high aspect-ratio flags [40] identified many similar features as 2D simulations at lower Reynolds numbers [32, 69, 77]. However, the difference in Reynolds numbers makes it difficult to isolate the cause of differences that do appear. Moreover, a recent study by Sader, Huertas-Cerdeira, and Gharib [70] demonstrated that in the limit of very small aspect-ratios significant differences arise from the 2D and large aspect-ratio cases. Future work could characterize the effect of intermediate aspect-ratios in more detail.

There are changes to the configuration that could also provide insights into the system, both scientifically and in terms of its energy harvesting potential. Shoele and Mittal [77] coupled the fluid-structure equations to an electrical model to study the effect of coating the flag with a piezoelectric material. Yet, there are other means of harvesting electrical energy from the flag, such as placing a transducer at its base [46]. Future work could model these alternative energy-harvesting approaches to determine their efficacy. In addition, one could consider the effect of nonzero initial inclination angle of the flag. This was initially investigated by Shoele and Mittal [77], but several questions such as the mechanism responsible for the onset of flapping at nonzero inclination angle remain unanswered. Finally, future efforts could also consider the effect of nonuniform mass or stiffness distribution in the flag, as either of these could influence the system dynamics significantly.

BIBLIOGRAPHY

[1] Deniz Tolga Akcabay and Yin Lu Young. "Hydroelastic response and energy harvesting potential of flexible piezoelectric beams in viscous flow". In: *Physics of Fluids* 24.5 (2012).

[2] Silas Alben. "The flapping-flag instability as a nonlinear eigenvalue problem". In: *Physics of Fluids* 20.10 (2008).

[3] Shervin Bagheri. "Koopman-mode decomposition of the cylinder wake". In: *Journal of Fluid Mechanics* 726 (2013), pp. 596–623.

[4] Shervin Bagheri et al. "Global stability of a jet in crossflow". In: *Journal of Fluid Mechanics* 624 (2009), pp. 33–44.

[5] D Barkley. "Linear analysis of the cylinder wake mean flow". In: *EPL (Europhysics Letters)* 75 (2006).

[6] Klaus Jürgen Bathe. *Finite element procedures*. Prentice-Hall: Englewood Cliffs, NJ, 1996.

[7] Andrey Belov, Luigi Martinelli, and A Jameson. "A new implicit algorithm with multigrid for unsteady incompressible flow calculations". In: *AIAA paper* 95 (1995).

[8] Gal Berkooz, Philip Holmes, and John L Lumley. "The proper orthogonal decomposition in the analysis of turbulent flows". In: *Annual Review of Fluid Mechanics* 25.1 (1993), pp. 359–575.

[9] Antoine Blanchard, Lawrence A Bergman, and Alexander F Vakakis. "Targeted energy transfer in laminar vortex-induced vibration of a sprung cylinder with a nonlinear dissipative rotator". In: *Physica D: Nonlinear Phenomena* 350 (2017), pp. 26–44.

[10] Iman Borazjani, Liang Ge, and Fotis Sotiropoulos. "Curvilinear immersed boundary method for simulating fluid structure interaction with complex 3D rigid bodies". In: *Journal of Computational Physics* 227.16 (2008), pp. 7587–7620.

[11] M Bozkurttas et al. "Low-dimensional models and performance scaling of a highly deformable fish pectoral fin". In: *Journal of Fluid Mechanics* 631 (2009), pp. 311–342.

[12] Paola Causin, Jean-Frédéric Gerbeau, and Fabio Nobile. "Added-mass effect in the design of partitioned algorithms for fluid–structure problems". In: *Computer Methods in Applied Mechanics and Engineering* 194.42 (2005), pp. 4506–4527.

[13] Alper Cesur et al. “Analysis of the wake dynamics of stiff and flexible cantilever beams using POD and DMD”. In: *Computers & Fluids* 101 (2014), pp. 27–41.

[14] Kevin K Chen, Jonathan H Tu, and Clarence W Rowley. “Variants of dynamic mode decomposition: boundary condition, Koopman, and Fourier analyses”. In: *Journal of Nonlinear Science* 22.6 (2012), pp. 887–915.

[15] Tim Colonius and Kunihiko Taira. “A fast immersed boundary method using a nullspace approach and multi-domain far-field boundary conditions”. In: *Computer Methods in Applied Mechanics and Engineering* 197.25 (2008), pp. 2131–2146.

[16] Tim Colonius and Kunihiko Taira. “A fast immersed boundary method using a nullspace approach and multi-domain far-field boundary conditions”. In: *Computer Methods in Applied Mechanics and Engineering* 197.25 (2008), pp. 2131–2146.

[17] Benjamin SH Connell and Dick KP Yue. “Flapping dynamics of a flag in a uniform stream”. In: *Journal of Fluid Mechanics* 581 (2007), pp. 33–67.

[18] MA Criesfield. *Non-linear finite element analysis of solids and structures, vol. 1*. Wiley, New York, 1991.

[19] Joris Degroote, Klaus-Jürgen Bathe, and Jan Vierendeels. “Performance of a new partitioned procedure versus a monolithic procedure in fluid–structure interaction”. In: *Computers & Structures* 87.11 (2009), pp. 793–801.

[20] Earl H Dowell and Kenneth C Hall. “Modeling of fluid-structure interaction”. In: *Annual Review of Fluid Mechanics* 33.1 (2001), pp. 445–490.

[21] Subrahmanyam Duvvuri and Beverley J McKeon. “Triadic scale interactions in a turbulent boundary layer”. In: *Journal of Fluid Mechanics* 767 (2015).

[22] Uwe Ehrenstein and Francois Gallaire. “On two-dimensional temporal modes in spatially evolving open flows: the flat-plate boundary layer”. In: *Journal of Fluid Mechanics* 536 (2005), pp. 209–218.

[23] Vassiliy A Epanechnikov. “Non-parametric estimation of a multivariate probability density”. In: *Theory of Probability & Its Applications* 14.1 (1969), pp. 153–158.

[24] Ronald P Fedkiw et al. “A non-oscillatory Eulerian approach to interfaces in multimaterial flows (the ghost fluid method)”. In: *Journal of Computational Physics* 152.2 (1999), pp. 457–492.

[25] Christiane Förster, Wolfgang A. Wall, and Ekkehard Ramm. “Artificial added mass instabilities in sequential staggered coupling of nonlinear structures and incompressible viscous flows”. In: *Computer Methods in Applied Mechanics and Engineering* 196.7 (2007), pp. 1278–1293.

[26] Anvar Gilmanov, Trung Bao Le, and Fotis Sotiropoulos. “A numerical approach for simulating fluid structure interaction of flexible thin shells undergoing arbitrarily large deformations in complex domains”. In: *Journal of Computational Physics* 300 (2015), pp. 814–843.

[27] Andres Goza and Tim Colonius. “A global mode analysis of flapping flags”. In: Turbulence and Shear Flow Phenomena 10. Chicago, Illinois, 2017.

[28] Andres Goza and Tim Colonius. “A strongly-coupled immersed-boundary formulation for thin elastic structures”. In: *Journal of Computational Physics* 336 (2017), pp. 401–411.

[29] Andres Goza and Tim Colonius. “Data analysis of fluid-structure interaction”. In: *In preparation* (2017).

[30] Andres Goza, Tim Colonius, and John E Sader. “Nonlinear simulations and global modes of inverted flag flapping”. In: *In preparation* (Submitted).

[31] Andres Goza et al. “Accurate computation of surface stresses and forces with immersed boundary methods”. In: *Journal of Computational Physics* 321 (2016), pp. 860–873.

[32] PS Gurugubelli and RK Jaiman. “Self-induced flapping dynamics of a flexible inverted foil in a uniform flow”. In: *Journal of Fluid Mechanics* 781 (2015), pp. 657–694.

[33] Per Christian Hansen. *Rank-deficient and discrete ill-posed problems: numerical aspects of linear inversion*. Vol. 4. SIAM, 1998.

[34] Gene Hou, Jin Wang, and Anita Layton. “Numerical methods for fluid-structure interaction—a review”. In: *Communications in Computational Physics* 12.02 (2012), pp. 337–377.

[35] Wei-Xi Huang, Soo Jai Shin, and Hyung Jin Sung. “Simulation of flexible filaments in a uniform flow by the immersed boundary method”. In: *Journal of Computational Physics* 226.2 (2007), pp. 2206–2228.

[36] Wei-Xi Huang and Hyung Jin Sung. “An immersed boundary method for fluid–flexible structure interaction”. In: *Computer Methods in Applied Mechanics and Engineering* 198.33 (2009), pp. 2650–2661.

[37] C Ji, A Munjiza, and JJR Williams. “A novel iterative direct-forcing immersed boundary method and its finite volume applications”. In: *Journal of Computational Physics* 231.4 (2012), pp. 1797–1821.

[38] Bakytzhan Kallemov et al. “An immersed boundary method for rigid bodies”. In: *Communications in Applied Mathematics and Computational Science* 11.1 (2016), pp. 79 –141.

[39] A. Khalak and Charles HK Williamson. “Motions, forces and mode transitions in vortex-induced vibrations at low mass-damping”. In: *Journal of Fluids and Structures* 13 (1999), pp. 813–851.

[40] Daegyoum Kim et al. “Flapping dynamics of an inverted flag”. In: *Journal of Fluid Mechanics* 736 (2013).

[41] Rainer Kress. *Linear integral equations*. 3rd ed. Vol. 82. Springer, 2014.

[42] J Nathan Kutz et al. *Dynamic Mode Decomposition: Data-Driven Modeling of Complex Systems*. SIAM, 2016.

[43] Uğis Lācis, Kunihiko Taira, and Shervin Bagheri. “A stable fluid–structure-interaction solver for low-density rigid bodies using the immersed boundary projection method”. In: *Journal of Computational Physics* 305 (2016), pp. 300–318.

[44] Ming-Chih Lai and Charles S Peskin. “An immersed boundary method with formal second-order accuracy and reduced numerical viscosity”. In: *Journal of Computational Physics* 160.2 (2000), pp. 705–719.

[45] DV Le, BC Khoo, and KM Lim. “An implicit-forcing immersed boundary method for simulating viscous flows in irregular domains”. In: *Computer Methods in Applied Mechanics and Engineering* 197.25 (2008), pp. 2119–2130.

[46] *Design and experimental evaluation of flextensional-cantilever based piezoelectric transducers for flow energy harvesting*. SPIE Smart Structures, Materials+ Nondestructive Evaluation, and Health Monitoring. 2016.

[47] Injae Lee and Haecheon Choi. “A discrete-forcing immersed boundary method for the fluid–structure interaction of an elastic slender body”. In: *Journal of Computational Physics* 280 (2015), pp. 529–546.

[48] Richard B Lehoucq, Danny C Sorensen, and Chao Yang. *ARPACK users' guide: solution of large-scale eigenvalue problems with implicitly restarted Arnoldi methods*. SIAM, 1998.

[49] Zhilin Li and Ming-Chih Lai. “The Immersed Interface Method for the Navier–Stokes Equations with Singular Forces”. In: *Journal of Computational Physics* 171.2 (2001), pp. 822–842.

[50] Erwan Liberge and Aziz Hamdouni. “Reduced order modelling method via proper orthogonal decomposition (POD) for flow around an oscillating cylinder”. In: *Journal of Fluids and Structures* 26.2 (2010), pp. 292–311.

[51] Sebastian Liska and Tim Colonius. “A fast immersed boundary method for external incompressible viscous flows using lattice Green’s functions”. In: *Journal of Computational Physics* 331 (2016), pp. 257–279.

[52] C Liu, X Zheng, and CH Sung. “Preconditioned multigrid methods for unsteady incompressible flows”. In: *Journal of Computational Physics* 139 (1998), pp. 35–57.

[53] Haoxiang Luo et al. “On the numerical oscillation of the direct-forcing immersed-boundary method for moving boundaries”. In: *Computers & Fluids* 56 (2012), pp. 61–76.

[54] Igor Mezić. “Analysis of fluid flows via spectral properties of the Koopman operator”. In: *Annual Review of Fluid Mechanics* 45 (2013), pp. 357–378.

[55] Sébastien Michelin, Stefan G Llewellyn Smith, and Beverley J Glover. “Vortex shedding model of a flapping flag”. In: *Journal of Fluid Mechanics* 617 (2008), pp. 1–10.

[56] Rajat Mittal and Gianluca Iaccarino. “Immersed boundary methods”. In: *Annual Review of Fluid Mechanics* 37 (2005), pp. 239–261.

[57] Rajat Mittal et al. “A versatile sharp interface immersed boundary method for incompressible flows with complex boundaries”. In: *Journal of Computational Physics* 227.10 (2008), pp. 4825–4852.

[58] Sanjay Mittal and Saurav Singh. “Vortex-induced vibrations at subcritical Re”. In: *Journal of Fluid Mechanics* 534 (2005), pp. 185–194.

[59] Yoichiro Mori and Charles S Peskin. “Implicit second-order immersed boundary methods with boundary mass”. In: *Computer Methods in Applied Mechanics and Engineering* 197.25 (2008), pp. 2049–2067.

[60] Bernd R Noack and Helmut Eckelmann. “A global stability analysis of the steady and periodic cylinder wake”. In: *Journal of Fluid Mechanics* 270 (1994), pp. 297–330.

[61] J Blair Perot. “An analysis of the fractional step method”. In: *Journal of Computational Physics* 108.1 (1993), pp. 51–58.

[62] Charles S Peskin. “Flow patterns around heart valves: a numerical method”. In: *Journal of Computational Physics* 10.2 (1972), pp. 252–271.

[63] Charles S Peskin. “The immersed boundary method”. In: *Acta Numerica* 11 (2002), pp. 479–517.

[64] Alexandre M Roma, Charles S Peskin, and Marsha J Berger. “An adaptive version of the immersed boundary method”. In: *Journal of Computational Physics* 153.2 (1999), pp. 509–534.

[65] Anatol Roshko. *On the development of turbulent wakes from vortex streets*. National Advisory Committee for Aeronautics, 1953.

[66] Anatol Roshko. *On the drag and shedding frequency of two-dimensional bluff bodies*. Tech. rep. National Advisory Committee for Aeronautics; Washington, DC, United States, 1954.

[67] Clarence W Rowley and Scott TM Dawson. “Model reduction for flow analysis and control”. In: *Annual Review of Fluid Mechanics* 49 (2017), pp. 387–417.

[68] Clarence W Rowley et al. “Spectral analysis of nonlinear flows”. In: *Journal of Fluid Mechanics* 641 (2009), pp. 115–127.

[69] Jaeha Ryu et al. “Flapping dynamics of an inverted flag in a uniform flow”. In: *Journal of Fluids and Structures* 57 (2015).

[70] John E Sader, Cecilia Huertas-Cerdeira, and Morteza Gharib. “Stability of slender inverted flags and rods in uniform steady flow”. In: *Journal of Fluid Mechanics* 809 (2016), pp. 873–894.

[71] John E Sader et al. “Large-amplitude flapping of an inverted flag in a uniform steady flow–a vortex-induced vibration”. In: *Journal of Fluid Mechanics* 793 (2016).

[72] Turgut Sarpkaya. “A critical review of the intrinsic nature of vortex-induced vibrations”. In: *Journal of Fluids and Structures* 19 (2004), pp. 389–447.

[73] Peter Schmid. “Dynamic mode decomposition of numerical and experimental data”. In: *Journal of Fluid Mechanics* 656 (2010), pp. 5–28.

[74] Jung Hee Seo and Rajat Mittal. “A sharp-interface immersed boundary method with improved mass conservation and reduced spurious pressure oscillations”. In: *Journal of Computational Physics* 230.19 (2011), pp. 7347–7363.

[75] Jung Hee Seo and Rajat Mittal. “A sharp-interface immersed boundary method with improved mass conservation and reduced spurious pressure oscillations.” In: *Journal of Computational Physics* 230.19 (2011), pp. 7347–7363.

[76] Michael J Shelley and Jun Zhang. “Flapping and bending bodies interacting with fluid flows”. In: *Annual Review of Fluid Mechanics* 43 (2011), pp. 449–465.

[77] Kourosh Shoele and Rajat Mittal. “Energy harvesting by flow-induced flutter in a simple model of an inverted piezoelectric flag”. In: *Journal of Fluid Mechanics* 790 (2016), pp. 582–606.

[78] Lawrence Sirovich and Michael Kirby. “Low-dimensional procedure for the characterization of human faces”. In: *JOSA A* 4.3 (1987), pp. 519–524.

[79] Kunihiko Taira and Tim Colonius. “The immersed boundary method: a projection approach”. In: *Journal of Computational Physics* 225.2 (2007), pp. 2118–2137.

[80] Sadatoshi Taneda. “Waving motions of flags”. In: *Journal of the Physical Society of Japan* 24.2 (1968), pp. 392–401.

[81] James L Tangorra et al. “The effect of fin ray flexural rigidity on the propulsive forces generated by a biorobotic fish pectoral fin”. In: *Journal of Experimental Biology* 213.23 (2010), pp. 4043–4054.

[82] Fang-Bao Tian et al. “Fluid–structure interaction involving large deformations: 3D simulations and applications to biological systems”. In: *Journal of Computational Physics* 258 (2014), pp. 451–469.

[83] Anna-Karin Tornberg and Bjorn Engquist. “Numerical approximations of singular source terms in differential equations”. In: *Journal of Computational Physics* 200.2 (2004), pp. 462–488.

[84] Aaron Towne, Oliver T Schmidt, and Tim Colonius. “Spectral proper orthogonal decomposition and its relationship to dynamic mode decomposition and resolvent analysis”. In: *arXiv preprint arXiv:1708.04393* (2017).

[85] Jonathan H Tu et al. “On dynamic mode decomposition: theory and applications”. In: *Journal of Computational Dynamics* 1 (2014), pp. 391–421.

[86] HS Udaykumar et al. “A sharp interface Cartesian grid method for simulating flows with complex moving boundaries”. In: *Journal of Computational Physics* 174.1 (2001), pp. 345–380.

[87] Markus Uhlmann. “An immersed boundary method with direct forcing for the simulation of particulate flows”. In: *Journal of Computational Physics* 209.2 (2005), pp. 448–476.

[88] Chengjie Wang and Jeff D Eldredge. “Strongly coupled dynamics of fluids and rigid-body systems with the immersed boundary projection method”. In: *Journal of Computational Physics* 295 (2015), pp. 87–113.

[89] Charles HK Williamson and Anatol Roshko. “Vortex formation in the wake of an oscillating cylinder”. In: *Journal of Fluids and Structures* 2.4 (1988), pp. 355–381.

[90] Alan Wolf et al. “Determining Lyapunov exponents from a time series”. In: *Physica D: Nonlinear Phenomena* 16.3 (1985), pp. 285–317.

[91] Jianming Yang and Frederick Stern. “Sharp interface immersed-boundary/level-set method for wave–body interactions”. In: *Journal of Computational Physics* 228.17 (2009), pp. 6590–6616.

[92] Xiaolei Yang et al. “A smoothing technique for discrete delta functions with application to immersed boundary method in moving boundary simulations”. In: *Journal of Computational Physics* 228.20 (2009), pp. 7821–7836.

[93] Sara Zahedi and Anna-Karin Tornberg. “Delta function approximations in level set methods by distance function extension”. In: *Journal of Computational Physics* 229 (2010), pp. 2199–2219.

[94] N Zhang and Zhongquan Charlie Zheng. “An improved direct-forcing immersed-boundary method for finite difference applications”. In: *Journal of Computational Physics* 221.1 (2007), pp. 250–268.